

ANATOMICAL IMAGE SERIES ANALYSIS IN THE
COMPUTATIONAL ANATOMY RANDOM ORBIT
MODEL

by

Brian Curtis Lee

A dissertation submitted to Johns Hopkins University in conformity with the requirements
for the degree of Doctor of Philosophy

Baltimore, Maryland

July, 2020

Abstract

Serially acquired medical imagery plays an important role in the computational study of human anatomy. In this work, we describe the development of novel algorithms set in the large deformation diffeomorphic metric mapping framework for analyzing serially acquired imagery of two general types: spatial image series and temporal image series. In the former case, a critical step in the analysis of neural connectivity from serially-sectioned brain histology data is the reconstruction of spatially distorted image volumes and registration into a common coordinate space. In the latter case, computational methods are required for building low dimensional representations of the infinite dimensional shape space standard to computational anatomy. Here, we review the vast body of work related to volume reconstruction and atlas-mapping of serially-sectioned data as well as diffeomorphic methods for longitudinal data and we position our work relative to these in the context of the computational anatomy random orbit model. We show how these two problems are embedded as extensions to the classic random orbit model and use it to both enforce diffeomorphic conditions and analyze the distance metric associated to diffeomorphisms. We apply our

new algorithms to histology and MRI datasets to study the structure, connectivity, and pathological degeneration of the brain.

Readers: Michael I. Miller (advisor), J. Tilak Ratnanather

Acknowledgements

I would like to thank my advisor, Dr. Michael I. Miller, for his invaluable guidance, teachings, and support throughout the PhD program. I deeply appreciate the opportunity that he has given me to participate in exciting research in the field of computational anatomy and to be a member of this distinguished center, as well as the freedom he has afforded me to explore my own research interests in this area.

I would like to thank the members of my thesis committee, Dr. Tilak Ratnanather and Dr. Joshua Vogelstein, for their insightful counsel and for guiding my work in the right direction.

I would like to thank my numerous collaborators at Johns Hopkins University and the Center for Imaging Science, as well as institutions across the globe, for their enthusiasm and involvement.

Finally, I would like to thank my family, loved ones, and friends for their positivity and

unwavering support of my efforts over the past years.

Contents

Abstract	ii
Acknowledgements	iv
List of Figures	x
List of Tables	xiii
1 Introduction	1
1.1 Diffeomorphic Mapping	2
1.2 Random Orbit Model	4
1.3 Spatial Image Series	6
1.3.1 Connectomics	6
1.3.2 Brain Histology	7
1.3.3 Histological Reconstruction	7
1.3.4 Analysis of Histology-Associated Deformations	9

1.3.5	Cardiac Shape Analysis	10
1.3.6	Shape Interpolation	11
1.3.7	Our Contributions	11
1.4	Longitudinal Image Series	12
1.4.1	Alzheimer’s Disease	13
1.4.2	Diffeomorphometry in Longitudinal Imaging	13
1.4.3	Our Contributions	14
1.5	Outline of Thesis	15
2	Volume Reconstruction of Spatial Image Series	17
2.1	Methods	20
2.1.1	The Log-Likelihood Model of the Histology Sectioning Problem . . .	21
2.1.2	The Priors: Diffeomorphisms and Sobolev Smoothness of Images . . .	24
2.1.3	MAP, Penalized-Likelihood Reconstruction	27
2.1.4	Iterative Algorithm for Joint Penalized Likelihood and MAP Estimator	30
2.1.5	Gradients for Atlas Free Model	31
2.1.6	Gradients for Atlas Informed Model	33
2.1.7	Distances for Variational Methods	37
2.1.8	Diffeomorphometry of Histological Procedures	39
2.1.9	Serial Section Shape Interpolation	40
2.1.10	Software Implementation	42

2.2	Results	44
2.2.1	Evaluation of Reconstruction Accuracy	44
2.2.2	Evaluation of Registration Accuracy	54
2.2.3	Atlas-Informed Volume Reconstruction of Mouse Brain Architecture Project Data	57
2.2.4	MRI-Guided Volume Reconstruction of Brain/MINDS Marmoset His- tology Data	60
2.2.5	Effect of Model Priors on Curvature Preservation	64
2.2.6	Quantification of Metric Distortions in Brain/MINDs Data	68
2.2.7	Volume Reconstruction in Mouse Cardiac MRI	75
2.3	Discussion	84
3	Diffeomorphometry for Longitudinal Shape Analysis	88
3.1	Methods	89
3.1.1	Brownian Motion and Hamiltonian Flows	89
3.1.2	Drift Model for Longitudinal Shape Analysis	92
3.1.3	Estimating Personalized Control under Drift	94
3.1.4	Derivation of Dynamics Equations	95
3.1.5	Surface Matching Algorithm	98
3.1.6	Estimating Mean Drift of a Population	100
3.2	Results	103

3.2.1	Simulations based on Geodesic Shooting	103
3.2.2	Alzheimer’s Disease Neuroimaging Initiative	107
3.2.3	Surface Representation of Subcortical Structures in ADNI	107
3.2.4	Computing the Drift of ADNI Populations	108
3.2.5	Computing the Personalized Controls of ADNI Subjects	111
3.3	Discussion	113
4	Conclusion	116
A	Reproducing Kernel Hilbert Space and Green’s Kernel.	121
B	Geodesics solving Euler-Lagrange Equations.	123
C	Coadjoint Transport	126
	Curriculum Vitae	155

List of Figures

1.1	The random orbit model.	5
1.2	Sample histology slides.	8
2.1	The random orbit model extended to serial-section imagery	20
2.2	The histological sectioning model	22
2.3	Histology registration pipeline workflow	43
2.4	Comparison of atlas-free and atlas-informed models in simulated binary phantom	46
2.5	Comparison of resulting diffeomorphic transformation of atlas phantoms . . .	47
2.6	Atlas phantom simulation to validate recovery of sectioning parameters and diffeomorphic shape difference	49
2.7	Simulated noise on a binary image phantom	51
2.8	Evaluation of estimator MSE, variance, and bias	52
2.9	Image overlap after volume to volume registration	55

2.10 Comparison of reconstruction and mapping using atlas-free and atlas-informed models on data from the MBAP database	58
2.11 Comparison of diffeomorphic transformation recovered from atlas-free and atlas-informed models	59
2.12 Selected regions of the brain segmented by the atlas-informed and atlas-free models carry the label map from the Allen atlas under the computed diffeomorphism	60
2.13 Sample Nissl-stained and fluorescent data displayed with segmented and reconstructed tracer detections	63
2.14 Reconstruction examples depicting the effect of the smoothness prior	65
2.15 Histology restacking examples from Brain/MINDS dataset	67
2.16 Local scale factor change in two ex-vivo to histology mappings and two in-vivo to ex-vivo mappings	69
2.17 Histograms of local percent scale factor change in two ex-vivo to histology mappings and two in-vivo to ex-vivo mappings	71
2.18 Metric scale change associated with subvolume sections between in-vivo and ex-vivo MRIs	72
2.19 Metric scale change of in-vivo to ex-vivo mapping in atlas coordinates	73
2.20 Sample images from the mouse cardiac MR dataset	76
2.21 Long axis resampling examples	77

2.22	Short axis sample sections	79
2.23	Short axis resampling examples	79
2.24	Intensity error comparison between methods	80
2.25	Segmentation overlap between methods	82
2.26	Segmentation upsampling	83
2.27	Upsampling of human brain histology	84
3.1	Diagram of infinitesimal mean drift model	93
3.2	Longitudinal model for two subpopulations	101
3.3	Drift Estimation in Simulated Data	105
3.4	Personalized Control Estimation in Simulated Data	106
3.5	Surface generation process	108
3.6	Drift estimation in ADNI data	110
3.7	Personalized control estimation in ADNI data	112
3.8	Mean personalized control in ADNI data	113

List of Tables

2.1	Summary of landmarks selected for registration accuracy	56
-----	---	----

Chapter 1

Introduction

The acquisition of series of images is ubiquitous throughout the anatomical medical imaging setting. Imaging has become a critical tool for exploring and understanding the structural-to-functional relationship of complex organs like the brain, as well as the disruption of that relationship by disease. This is particularly true in the cases of neuro and cardiac imaging, where imaging in both spatial and temporal dimensions can provide valuable clinical insight. However, the traditional random orbit model of computational anatomy has focused primarily on the generation of single variants of an exemplar under diffeomorphic transformations governed by the large deformation diffeomorphic metric mapping (LDDMM) framework [1]. As modern imaging tasks become more complex, high-dimensional, and high-resolution, the need rises for new computational methods to handle these datatypes. In this work, we describe the development of methods to analyze spatial and temporal series of brain and

heart imagery, and we present our work in the context of the random orbit model of human anatomy and as extensions to the general LDDMM framework.

1.1 Diffeomorphic Mapping

The large deformation diffeomorphic metric mapping framework is well suited to the study of variation in human anatomy. In this model, shapes and images are acted on by the group of diffeomorphisms $\varphi \in \text{Diff}$, or smooth, 1-to-1, invertible transformations. Diffeomorphic flows are controlled by the evolution $\dot{\varphi}_t = v_t \circ \varphi_t, t \in [0, 1]$ with $\varphi \doteq \varphi_t$ for smooth vector fields $v \in V$ in a smooth reproducing kernel Hilbert space. This ensures that the flows are diffeomorphisms, making the LDDMM framework ideal for the study of the smooth and continuous structure of human anatomy.

Solving for the flows and correspondences between two structures is generally posed as an image registration problem, or as registration between parameterized representations of objects in images. In the case of images, diffeomorphisms can be parameterized as time-varying velocity fields $v_t, t \in [0, 1] \rightarrow \mathbb{R}^N$. Computing the optimal v_t that solves this flow generally involves minimizing a functional that takes the form:

$$E_t = \int_0^1 \|v_t\|_V^2 dt + \frac{1}{\sigma^2} M(\varphi_1 \cdot I, J) \quad (1.1)$$

where I and J are two images or parametric representations and M is some function defining

the distance between deformed template $\varphi_1 \cdot I$ and target image J . In the case of dense images, M is classically the sum of squared error such that:

$$M(\varphi_1 \cdot I, J) = \|\varphi_1 \cdot I - J\|_{L_2}^2 \quad (1.2)$$

The Euler-Lagrange equations have been solved by Beg [1], giving solutions to the minimization problem:

$$\nabla_v E_t = 2v_t - K \left(\frac{2}{\sigma^2} |D\varphi_{t,1}| \nabla(I \circ \varphi_{1,0}) (\delta_t M(I \circ \varphi_{1,0}, J) \circ \varphi_{t,1}) \right) \quad (1.3)$$

Diffeomorphic mapping of brain volumes has been a central focus in the field of Computational Anatomy [2–18]. Mapping methods initially followed the small deformation and elasticity methods of Bajcsy and others [19–24]. Subsequently Christensen et al [25] introduced large deformation flows for topology preservation in dense volume matching [26]. Since these early inceptions many methods have been developed based on both landmark and triangulated surface based spline deformations [27–29] as well as large deformation methods [30–34]. For dense images (i.e. 3D voxelized image volumes) with multiple modalities and tensor fields such as Diffusion track imaging (DTI), these methods were further developed and form the basis of the multiple contrast, multi-scale algorithmic framework that is well-described in the literature, but note that much of this work has focused on MRI volumes [1, 35–51].

1.2 Random Orbit Model

We model the observed medical imagery or anatomical structures as arising from the computational anatomy [52] random orbit model [53]. The random orbit model is a generative representation of anatomical imagery in which individual observations are probabilistically modeled as arising from deformations of some exemplar. Here, we specify these deformation as diffeomorphisms due to their suitability for studying human anatomy.

This model frames the optimization of Eqn (1.1) as a log likelihood maximization problem where the observed images are modeled as a conditional Gaussian random field with mean field $I \circ \varphi^{-1}$ for dense images. This is a powerful representation which has enabled algorithms such as the Bayesian template estimation algorithm and other methods based on Bayesian statistics.

Much of the existing body of work regarding the random orbit model in computational anatomy has dealt with independent observations and their relation to an exemplar. Here, we develop several algorithms intended to handle series of images and we present them as extensions to the classic random orbit model. We also take advantage of the random orbit model setting to quantitatively analyze the distance metric between diffeomorphisms cross-sectionally.

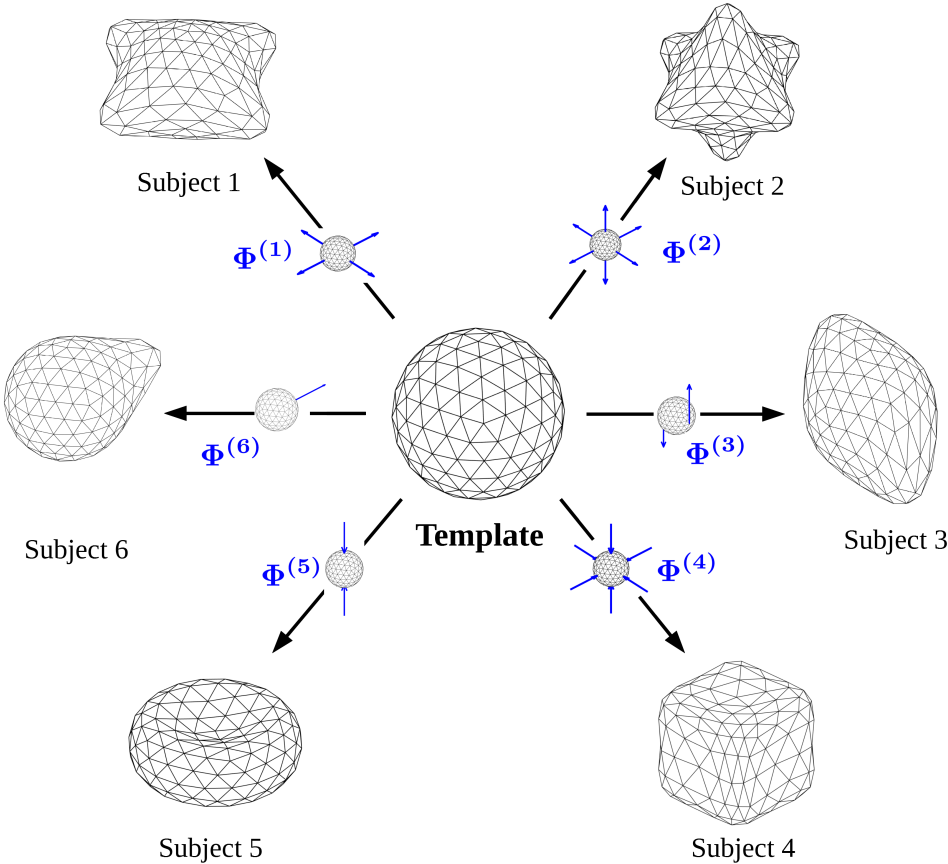


Figure 1.1: The computational anatomy random orbit model is depicted where the structure in the template coordinate space is a sphere. Six observations generated from deformations $\Phi^{(i)}$ on the template are shown.

1.3 Spatial Image Series

The first type of image series dealt with in our work are spatial image series. In anatomic and medical imaging, this can include histology, serial section MRI, and many other settings.

1.3.1 Connectomics

Understanding the basic structure and function of the brain remains one of the most important and challenging tasks in neuroscience despite its fundamental nature. It is generally understood that the brain is composed of a complex network of structures and connections which defines neural function [54]. These connections are not only fundamental to the basic function of the brain [55], but also deeply related to the pathology of neurodegenerative diseases [56] and to better understanding of artificial neural networks used in machine learning. The study of these networks in tandem with the physical structure of the brain has given rise to the field of connectomics. Studying the brain connectome remains challenging in part due to the size of the data – the human brain has an estimated 100 billion neurons [57] and several orders of magnitude more connections. Although modern developments in high-resolution brain imaging [58, 59], methods to label neurons [60], computational methods have been able to visualize the brain at the neuron level, investigation of the whole brain at this microscale remains difficult within current computational limits. As a result, much of the related work in human and primate brains has focused on the mesoscale resolution, a level between the macroscale of fiber bundles and the microscale of individual synapses [61].

1.3.2 Brain Histology

Neurohistology is a classical method for visualizing the brain and has greatly benefited from advancements in imaging technologies and neural tracing technologies to become one of the foremost methods to study the mesoscale neural architecture. Viral tract tracing (in which fluorescently tagged viruses designed to transport between neurons are injected into the brain and replicate) remains one of the most common methods for studying neural circuits at high resolution [62]. Figure 1.2 shows examples of serial section histology as observed in the clinic or laboratory. Individual sections of the image can be distorted by the sectioning process, the placement of the tissue under the imager, tissue damage, tissue warping due to chemical staining processes, and more. These settings involve additional degrees of freedom whereas the traditional random orbit model generally deals with coherent image volumes or structures. In the case of brain histology, the additional degrees of freedom are the transformations required to reconstruct a coherent volume from independently observed sections. This is a well studied problem with over 30 years of prior work in the literature, and at present there exists no general solution.

1.3.3 Histological Reconstruction

Circuit mapping is technique limited, and falls into three broad scales corresponding to distinct imaging modalities - indirect mapping at a macroscopic scale corresponding to MRI-based methods [63], and direct mapping at light (LM) and electron microscopic (EM) scales.

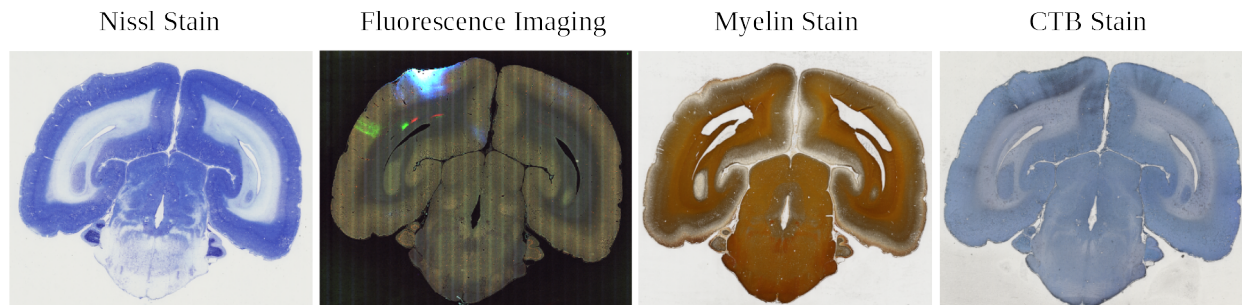


Figure 1.2: **Sample histology slides.** Common histology stains and modalities are shown. From left to right: Nissl stain, fluorescence imaging, myelin stain, Cholera toxin B stain.

For MRI and LM data, atlas mapping is an important step in the analysis. Several approaches exist for gathering LM data at the whole brain level [64–66]. For some of these approaches (two-photon serial block-face imaging, knife edge scanning microscopy and light sheet microscopy for cleared brains) two-dimensional (2D) optical sections are acquired in three-dimensional (3D) registry with each other, so that the only computational step required is 3D volumetric registration of the individual brain data set to a canonical atlas. However, for classical neurohistological approaches using tissue sectioning followed by histochemical processing, the 2D sections are gathered independently and each section can undergo an arbitrary rotation and translation compared to the block face. This may be considered a disadvantage of the classical neuroanatomical workflow, however the physical sectioning method followed by conventional histochemical analysis has certain important advantages. This allows for the full spectrum of histochemical stains, acquisition of physical sections for downstream molecular analyses, and processing for larger brains (upto and including whole human brains). Therefore it is necessary to perform an intermediate 2D to 3D registra-

tion step, where the individually acquired 2D sections are mutually co-registered into a 3D volume.

The histological reconstruction problem has been explored by several groups previously. Malandain first described the ill-posedness of reconstructing 3D sections and object curvature without prior knowledge of the shape of the object [67]. Rigid transformations for stack reconstruction have been estimated via block-matching of histological sections in [68], with point information based on landmarks introduced to guide volume reconstruction [69]. Dense external reference information such as MRI has been applied to guide reconstruction via registration of corresponding block-face photographs and for histology to MRI mapping [70, 71].

1.3.4 Analysis of Histology-Associated Deformations

Deformation of brain tissue caused by histological procedures is well known and has been reported in the previous literature and is a factor that must be considered in downstream image analysis. The chemical composition of the fixation solution and duration of exposure have been previously shown to cause significant tissue shrinkage [72–74]. More recently, histological distortions have been quantified with imaging techniques like MRI or computed tomography using variables such as total brain volume and the distance between hand-selected landmarks, in comparisons before and after mouse brain histology [75]. Others have assessed dense local deformative effects of extraction and fixation by examining the

strain resulting from a non-rigid displacement field [76]. Comparison of the total tissue area of imaged histological sections with block-face images can quantify the global in-plane shrinkage caused by sectioning, and neuronal density in the cutting axis has been used to quantify the non-uniformity of shrinkage in that direction [77].

1.3.5 Cardiac Shape Analysis

A second setting in which spatial image series analysis is innately involved is cardiac shape analysis. Complex shape changes in the chambers of the heart have long been associated with cardiomyopathy, particularly in the case of the left ventricle [78]. These shape changes have clinical implications for diagnosis and treatment as well as for the study of the pathological mechanisms of cardiomyopathy, for instance in treatment planning for hypertrophy of patients without the identifying genetic mutation [79].

Cardiac magnetic resonance imaging is commonly used in diagnostic and investigative imaging for studying ventricular shape and function due to the lack of ionizing radiation. However, due to the constant motion of the heart and the relatively long acquisition times of MRI, there is a resolution-to-acquisition-time tradeoff [80]. Images are generally acquired in 2D sections along the apex-base axis with each section acquired during subsequent phases of the cardiac cycle. Due to this acquisition scheme, sections are usually acquired sparsely in order to reduce total patient scanning times. This results image volumes that are highly anisotropic, reminiscent of histology stacks.

1.3.6 Shape Interpolation

General interpolation of shapes is a well-explored field of study. Traditional shape interpolation involves computing smooth trajectories between defined correspondences [81]. Other groups have proposed interpolation of longitudinal datasets and registration of time series [82], interpolation by geodesic flows [83, 84], population models [85], or joint modeling of shape and image intensity [86]. These methods generally involve extraction of image features and segmentation [87] or pairwise optical flow from neighbor to neighbor [88, 89].

Several studies have focused on developing methods to perform 3D reconstruction of the cardiac left ventricle (LV) from sparse MR imagery. These methods either employ interpolation [90] or surface-fitting to endocardial and epicardial contours using some predefined geometry [91]. Other approaches rely on diffeomorphic mapping of a high-resolution LV surface mesh to a set of sparse 2D short axis LV contours [92]. More recently, constrained neural network approaches have been used to incorporate prior anatomical knowledge to enhance sparsely collected 2D cardiac MR imagery [93]. These methods mostly rely on population-based atlases, predefined geometry (prolate-spheroidal) or training on ground truth data sets to reconstruct the 3D LV shape.

1.3.7 Our Contributions

In this work, we will explore the problem of curvature-preserving volume reconstruction without prior knowledge of the shape of the object. The lack of a shape prior places this work

into the random orbit model setting and is a common condition in brain histology settings. We will show that the classic volume-based random orbit model can be extended to serially-sectioned imagery and the solutions to image reassembly and registration problems can be solved variationally as with LDDMM. We will also use the techniques of diffeomorphometry as enabled by our embedding of serially-sectioned imagery into the random orbit model to quantify the deformative effects of histology processing on the brain. We will further extend our volume reconstruction algorithms by proposing a new method for interpolating shapes in order to upsample a sparsely acquired serial-section image stack using diffeomorphic transformations. We apply this methodology to upsample stacks of sparse 2D magnetic resonance cross-sections through live mouse hearts.

1.4 Longitudinal Image Series

In addition to adding spatial dimensions to our models of shape, we also turn to the study of longitudinal image series, in which multiple observations are made of the same set of individuals over time. We will investigate this problem in the context of a longitudinal imaging study of Alzheimer’s Disease patients, specifically the Alzheimer’s Disease Neuroimaging Initiative.

1.4.1 Alzheimer's Disease

Alzheimer's Disease is an incurable neurodegenerative disease which causes memory loss and personality/behavioral changes in elderly patients. It eventually leads to complications causing an estimated 122,000 deaths per year in the United States, making it the 6th leading cause of death in the US [94]. Alzheimer's is characterized by cortical and subcortical atrophy in the medial temporal lobe of the brain, particularly in the hippocampus and other nearby structures. However, atrophy is also associated with normal aging and Alzheimer's Disease patients are generally over 60 years of age. The challenge of studying the mechanism of neurodegeneration in Alzheimer's Disease is disentangling the shape change caused by normal aging versus the disease process.

1.4.2 Diffeomorphometry in Longitudinal Imaging

The study of shape in longitudinal neuroimaging data is a complex task that is generally approach by statistical methods in a field known as brain morphometry. We employ methods from a subfield known as diffeomorphometry, in which diffeomorphic mappings are used to quantify differences between shapes and trajectories of shapes and to define the relationship between elements of the random orbit model. Diffeomorphic trajectories that longitudinally map individuals can also be placed into the context of the random orbit model.

As well, atrophy and growth have been studied for understanding cohorts of shapes under transformation [8], in which time plays a role in simulation time for generating diffeomor-

phisms as well as in understanding the space-time phenomena of developmental and degenerative disease [95–105]. This field has progressed quickly and numerous groups have mapped populations of anatomical structures to common coordinate spaces in multiple contexts. Several formalized models of longitudinal shape analysis have been put forth to disentangle individual processes from population processes [82, 103, 106]. These mappings have been studied largely using mixed-effects modeling with statistical permutation testing [107–110] or linear operations on parameterized deformation fields [11, 111–115]. The motivation is to understand the typical representative shape change of populations as well as to make decisions concerning large deviations away from typical shape.

At the same time, the representation of population statistics in terms of high dimensional shape models has lagged behind. The mentioned examples have described methods for encoding means and variances of mapped populations in low dimensional statistical representations. However, little work has been done on directly encoding diffeomorphic modeling with typical population shape. The work proposed here is motivated by this goal.

1.4.3 Our Contributions

In this work, we will propose new models for determining the deviation of the shape change of brains with Alzheimer’s Disease from normally aging brains, under the random orbit model framework. We base our model off the classical models of Brownian motion with drift, in which the motion of particles is affected by a background ”drift”. Once again, we embed

our work into the random orbit model, this time extending the longitudinal dimension such that our template is no longer a single image but rather a trajectory over time. We take advantage of the inherent properties of the random orbit model in order to manipulate these trajectories, including operations such as averaging populations and computing deviations of individuals from populations.

1.5 Outline of Thesis

The following thesis will discuss the two main topics of image reconstruction of spatial image series and diffeomorphometry of a population of longitudinal image series. In the Chapter 2, we will discuss the motivation of our approach to the serial section image reconstruction problem. We will propose an extension to the classic random orbit model which allows for this computation under the same framework. We further expand our model to allow interpolation between sections under the Bayesian template estimation probabilistic model. Then, we show experimental results and implementation details on a dataset of mouse brain histology and cardiac MRI.

In Chapter 3, we will discuss the background of the longitudinal diffeomorphometry problem. We will propose our novel drift-based model for computing differences between two longitudinal diffeomorphic trajectories. In doing so, we will describe the computation of "biased geodesics", an augmentation of the classic geodesic shooting algorithm. Finally, we will show experimental results on simulated data and data from the Alzheimer's Disease

Neuroimaging Initiative study.

Chapter 2

Volume Reconstruction of Spatial Image Series

We first turn to the problem of volume reconstruction in serially sectioned or serially acquired imagery. This is a well studied problem in both the brain histology and cardiac MRI contexts and is a critical task for understanding the structure and function of the brain and the heart. In this chapter, we will first discuss a novel histology reconstruction and atlas mapping algorithm. We will show the results of implementing our algorithm for the Mouse Brain Architecture Project and the Marmoset Brain Architecture Project, as well as a quantitative analysis of the deformative properties of the histology process. Finally, we will show a further extension of the model to interpolation of anisotropic imagery. Some of the following text is taken from our publications ([116], [117] ©IEEE, selections reprinted with permission from

Lee BC et al., Diffeomorphic Upsampling of Serially Acquired Sparse 2D Cross-Sections in Cardiac MRI, Proceedings of the 2019 IEEE EMBC, 2019), [118] ©Wiley Periodicals 2020).

First, we develop a joint stack reconstruction and atlas mapping procedure that simultaneously restacks the 2D histology sections, applying a sequence of rigid motions to the sections, and estimates the diffeomorphic correspondence between the registered histology stack and a 3D atlas. We rigorously solve the problem when an external resource of identical geometry (such as an MRI of the same mouse) is not available, while accommodating for the innate anatomical variation from atlas to subject. The lack of a same-subject reference volume is often the standard in mouse brain histology and other large scale histology studies. This places us into the computational anatomy (CA) orbit problem for which constraints are inherited from an atlas that is diffeomorphic but not geometrically identical. With the availability of dense brain atlases at many resolution scales [119–122], methods to map atlas labels onto target coordinate systems are being ubiquitously deployed across neuroscience applications. Since Christensen’s early work [25], diffeomorphic transformation has become the de-facto standard as diffeomorphisms generate one-to-one and onto correspondences between coordinate systems. Herein we focus on the diffeomorphometry orbit model [53] of computational anatomy [2], where the space of dense volume imagery is modelled as a Riemannian orbit of an atlas under the diffeomorphism group. We use the large deformation diffeomorphic metric mapping algorithm first derived for dense imagery to retrieve the unknown high-dimensional reparameterization of the template coordinates.

We build on this work by extending our model to settings where the reconstruction process is informed by the ex-vivo MRI or other same-subject reference image of the brain prior to histology as well as an image intensity smoothness prior. We also incorporate multi-modal similarity metrics to order to accomodate cross-registration of multiple stains and imaging modalities. For instance, in our setting, we are generally interested in synchronizing the fluorescence microscopy imaging which reveals the viral tract tracing data with the Nissl stained imagery which clearly shows the anatomical structure. Importantly, we are able to quantify the 3D tissue distortion caused by two major parts of the histology procedure – the “sectioning” process (cryoprotection, freezing, sectioning) captured by the ex-vivo MRI to histology mapping and “preparatory” process (injection, incubation, perfusion, fixation) captured by the in-vivo MRI to ex-vivo MRI mapping.

As a final extension, we propose a method to upsample serially-acquired sparse serially-sectioned imagery based on a definition of a weighted mean derived from the well-known statistical template estimation [123] framework in computational anatomy. This method relies solely on the intrinsic constraint provided by the geometry of acquired sparse 2D images and does not require training or model fitting. The definition of a sliding windowed average of image slices with arbitrary center along an axis of a 3D image volume provides a flexible but robust framework for computing trajectories between shapes in neighboring image sections.

2.1 Methods

The novel aspect of the volume reconstruction method we propose is the augmentation of the random orbit model with transformations that describe serially-sectioned imagery. The extension to the model that allows the generation of this data is shown in Figure 2.1, where a slicing/sampling procedure along with some transformation $R^{(i)}$ produces the observed data.

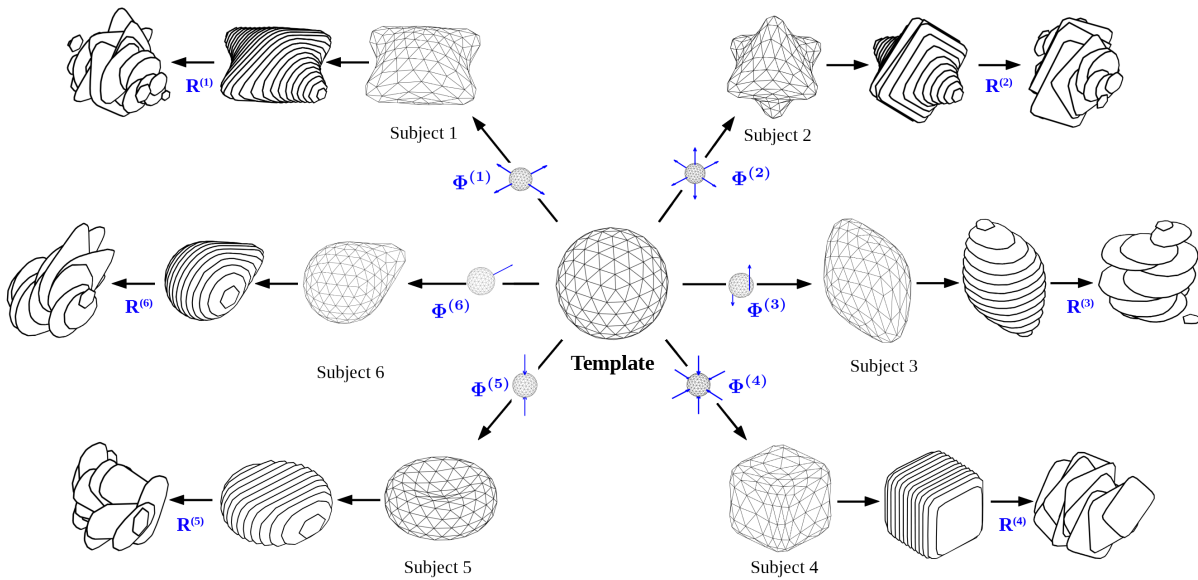


Figure 2.1: **The random orbit model and serial section imagery.** The computational anatomy random orbit model of Figure 1.1 is extended here for generation of serially-sectioned imagery distorted by some transformation $R^{(i)}$, $i = 1, 2, \dots, n$ for n serial sections.

At $20 \mu\text{m}$, this implies as many as 500 sections through the brain, augmenting the high-dimensionality of the diffeomorphism space to include as many as 1500 extra dimensions for planar rigid motions for restacking. Here lies the crux of the challenge. To accommodate the high-dimensionality of the unknown rigid motions, the space of stacked targets is modelled

to have finite-squared energy Sobolev norm, which enters the problem as a prior distribution restricting the roughness of the allowed restacked volumes. The variational method jointly optimizes over the high-dimensional diffeomorphism associated to the atlas reparameterization and the high-dimensional concatenation of rigid motions associated to the target.

2.1.1 The Log-Likelihood Model of the Histology Sectioning Problem

Fig 2.2 shows the components of the model for the histology stacking problem. Here, we discuss our work in the context of reconstructing brain histology stacks, particularly in mouse models which are the foremost high-throughput animal model for studying the brain. However, this work generalizes to any serially-sectioned imagery. We define the mouse brain to be sectioned as a dense three-dimensional (3D) object $I(x, y, z), (x, y, z) \in \mathbb{R}^3$, modelled to be a smooth deformation of a known, given template I_0 so that $I = I_0 \circ \varphi^{-1}$ for some invertible diffeomorphic transformation φ . The Allen Institute's mouse brain atlas [124] (CCF 2017) is taken as the template.

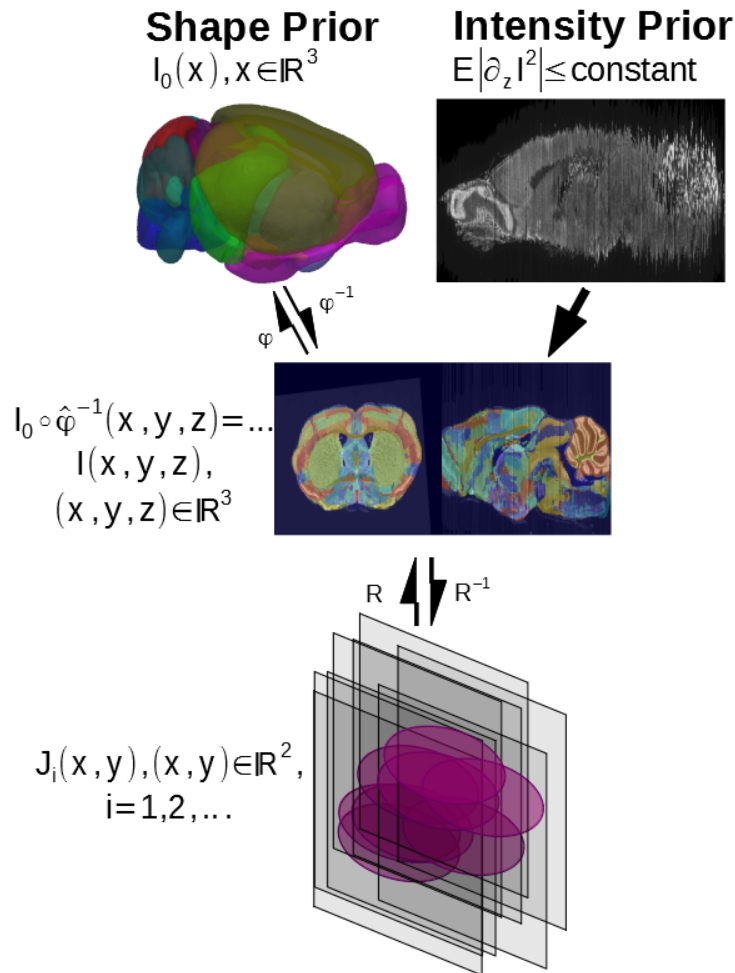


Figure 2.2: **The histological sectioning model.** The template I_0 , the mouse brain in the orbit $I \in \mathcal{I}$ and observed histological sections $J_i, i = 1, \dots, n$ are illustrated. The Sobolev image intensity prior and the shape prior are depicted in the top row. The model shows the template and mouse brain as elements of the same orbit $I_0, I \in \mathcal{I}$, such that there exists diffeomorphism $I = I_0 \circ \varphi^{-1}, \varphi \in \text{Diff}$.

Distinct from volumetric imaging such as MRI which delivers a dense 3D metric of the brain, the histology procedure (bottom row, Fig 2.2) consisting of sectioning, staining, and imaging generates a jitter process which randomly translates and rotates the stack sections.

Denote the rigid motions acting on the 2D sectioning planes $R_i : \mathbb{R}^2 \rightarrow \mathbb{R}^2$,

$$R_i(x, y) = (\cos \theta_i x + \sin \theta_i y + t_i^x, -\sin \theta_i x + \cos \theta_i y + t_i^y), \quad (x, y) \in \mathbb{R}^2, \quad (2.1)$$

with θ_i the rotation angle and $(t_i^x, t_i^y) \in \mathbb{R}^2$ the translation vector in section i . The histology stack $J_i(x, y), (x, y) \in \mathbb{R}^2, i = 1, \dots, n$, is a sequence of 2D image sections with jitter under smooth deformation of the atlas in noise:

$$J_i \circ R_i(x, y) = I_0 \circ \varphi^{-1}(x, y, z_i) + noise(x, y), \quad (x, y) \in \mathbb{R}^2. \quad (2.2)$$

Modeling the photographic noise as Gaussian and conditioning on the sequences of jitters $R_i, i = 1, \dots, n$ and atlas deformation $I = I_0 \circ \varphi^{-1}, \varphi \in Diff$, the photographic sections J_i are a sequence of conditionally Gaussian random fields with log-likelihood (with constants removed that are not a function of the parameters):

$$\ell(v, R; J) = \sum_i \left(-\alpha_i \int_{\mathbb{R}^2} |J_i \circ R_i(x, y) - I_0 \circ \varphi^{v, -1}(x, y, z_i)|^2 dx dy \right). \quad (2.3)$$

Here α_i is a weighting factor dependent on the noise of each section such that damaged sections can be weighted; v denotes the vector field which indexes the deformation as a diffeomorphic flow (see below).

2.1.2 The Priors: Diffeomorphisms and Sobolev Smoothness of Images

The parameterization of the histology pipeline augments the standard random orbit model of computational anatomy with the rigid-motion dimensions of the random jitter sectioning process. The unknowns to be estimated become $(R_1, \dots, R_n, \varphi) \in \mathbb{R}^{3n} \times Diff$ for n -sections. At $20 \mu\text{ m}$ then $n = 500$ implying the nuisance rigid motions are of high dimension $O(1500)$. The solution space must be constrained. We use priors on the deformations and on the rigid motion stacking of the images.

The Diffeomorphism Prior: The histological stacking constrains the brains as smooth transformations of the template, where the diffeomorphisms are generated as diffeomorphic flows $\varphi_t \in Diff$ [2], solving the ordinary differential equation

$$\dot{\varphi}_t = v_t \circ \varphi_t, t \in [0, 1], \varphi_0 = \textit{identity} , \quad (2.4)$$

with v_t the Eulerian velocity taking values in \mathbb{R}^3 , *identity* the identity mapping. The top row of Fig 2.2a shows that each φ has an inverse and that the random orbit model assumes any individual brain $I \in \mathcal{I}$ can be generated from the exemplar under the action of the diffeomorphism, so that for some $\varphi \in Diff$, $I = I \circ \varphi^{-1}$.

To score the distances between mouse brain coordinate systems and reject outlier solu-

tions we use geodesic flows minimizing metric length [125]. Large deviations as measured by the diffeomorphometry metric [53] from template atlas to target mouse brain are thus removed from the solution space. The vector fields are modeled to be in a reproducing kernel Hilbert space (RKHS) $(V, \|\cdot\|_V)$, supporting one continuous spatial derivative, and having geodesic length between coordinate systems determined by the norm-square $\|v\|_V^2$ of the RKHS:

$$\|v\|_V^2 = \sum_{i=1}^3 \int_{\mathbb{R}^3} ((-\nabla^2 + 1)^2 v_i(x, y, z))^2 dx dy dz < \infty . \quad (2.5)$$

This square-metric is used as a quadratic potential for the smoothness prior between images $I, I' \in \mathcal{I}$ [4, 126] minimizes the action

$$\rho^2(I, I') = \min_{\varphi: \varphi_0 = \text{id}, \varphi_1 \cdot I = I'} \int_0^1 \|v_t\|_V^2 dt . \quad (2.6)$$

and is used to determine the reproducing kernel Hilbert space norm for calculating the metric distance between images in the orbit. See Appendix A (Reproducing Kernel Hilbert Space and Green's Kernel) for the matrix Green's kernel and Appendix B (Geodesics solving Euler-Lagrange Equations) for the explicit equations for geodesics satisfying the Euler-Lagrange equations [6, 125].

We use the notation φ^v to emphasize the dependence of the diffeomorphism and the geodesic metric on the vector field v . Strictly speaking, the group generated by integrating (2.4) with finite norm $\|\cdot\|_V$ is both dependent on the norm of V as well as a subgroup of all

diffeomorphisms; we shall suppress that technical detail in the notation.

The Prior Distribution on Image Smoothness: To score the maximum a-posteriori (MAP) reconstruction of the rigid motions acting on the stack, we exploit a smoothness prior on the reconstructed histology stack which enforces the fact that anatomical structures are smooth and continuous. We model the images as arising from a smooth ‘‘Sobolev’’ or RKHS $I \in H^k$ supporting derivatives $\partial_h f = \frac{\partial^{h_1+h_2+h_3}}{\partial x^{h_1} \partial y^{h_2} \partial z^{h_3}} f$ that are square integrable, with norm:

$$\|I\|_{H^k}^2 = \sum_{h_1, h_2, h_3: |\sum_{i=1}^3 h_i| \leq k} \int_{\mathbb{R}^3} |\partial_h I(x, y, z)|^2 dx dy dz . \quad (2.7)$$

This is a quadratic form for a Gaussian random field prior on the dense histology stack with zero mean and covariance dependent on the squared norm $\|I\|_{H^k}^2$. For the purpose of stacking, the z-axis sections are sparse 20-40 μ m; the differential operators ∂_h are implemented via the difference operator along the sectioning z-axis (see Eqn. (2.8)). The Gaussian field has covariance determined by the difference operators; see [127] for example. We define the mixed differential-difference operator D_h as the centered difference for the z-partial derivatives,

$$D_h f(x, y, z) = \partial_{h_1, h_2} \left(\frac{f(x, y, z + \Delta/2) - f(x, y, z - \Delta/2)}{\Delta} \right) . \quad (2.8)$$

The gradient is forced to 0 at the boundaries of the image.

2.1.3 MAP, Penalized-Likelihood Reconstruction

Model the random sectioning with section-independent jitter as a product density $\pi(R) = \prod_i \pi(\theta_i, t_i^x, t_i^y)$, the priors centered at identity, with the priors on θ circular Gaussian with standard-deviation σ_θ and translation with means μ_c^x, μ_c^y at the center of the sections with $\sigma_c^x = \sigma_c^y$:

$$\pi(\theta, t^x, t^y) = \frac{1}{\sqrt{2\pi}\sigma_\theta} e^{-\frac{\theta^2}{2\sigma_\theta^2}} \frac{1}{\sqrt{2\pi}\sigma_c^x} e^{-\frac{(t_x - \mu_c^x)^2}{2\sigma_c^2}} \frac{1}{\sqrt{2\pi}\sigma_c^y} e^{-\frac{(t_y - \mu_c^y)^2}{2\sigma_c^2}}. \quad (2.9)$$

We choose our standard-deviations so that they are small relative to the center of the image, and a small rotation, roughly 5 percent of the total range of each. Generating MAP estimates of the rigid motions generates the MAP estimator of the histology restacking problem denoted as

$$I^R(x, y, z_i) = J_i \circ R_i(x, y), (x, y) \in \mathbb{R}^2, \quad i = 1, \dots, n.$$

Since the diffeomorphisms are infinite dimensional, the maximization of the log-likelihood function with respect to a function with the deformation penalty is termed the "penalized-likelihood estimator". Conditioned on the known atlas, the augmented random variables to be estimated are $(R_1, \dots, R_n, \varphi) \in (\mathbb{R}^{3n} \times \text{Diff})$.

Problem 1 (MAP, Penalized-Likelihood Estimator).

Given histology stack $J_i(x, y), (x, y) \in \mathbb{R}^2, i = 1, \dots$ and reconstructed stack $I^R(\cdot, z_i) = J_i \circ R_i(\cdot), i = 1, \dots, n$ modelled as conditionally Gaussian random fields conditioned on jitter and smooth dormation of the template. The joint MAP, Penalized-Likelihood estimators

$\arg \max_{R,v} \log \pi(R, v | J)$ given by

$$\begin{aligned} \operatorname{argmax}_{R,v} \quad & -\frac{1}{2} \int_0^1 \|v_t\|_V^2 dt - \frac{1}{2} \sum_i \|D_h I^R(\cdot, z_i)\|_2^2 \\ & + \sum_i (\log \pi(R_i) - \alpha_i \|I^R(\cdot, z_i) - I_0 \circ \varphi^{v,-1}(\cdot, z_i)\|_2^2) . \end{aligned} \quad (2.10)$$

The MAP, Penalized-Likelihood estimators satisfy

$$\left\{ \begin{array}{l} R^* = \operatorname{argmax}_{R_i, i=1, \dots} \sum_i (\log \pi(R_i) - \frac{1}{2} \|D_h I^R(\cdot, z_i)\|_2^2 \\ \qquad \qquad \qquad - \alpha_i \|I^R(\cdot, z_i) - I_0 \circ \varphi^{v^*, -1}(\cdot, z_i)\|_2^2) , \\ v^* = \operatorname{argmax}_v - \frac{1}{2} \int_0^1 \|v_t\|_V^2 dt - \sum_i \alpha_i \|I^{R^*}(\cdot, z_i) - I_0 \circ \varphi^{v,-1}(\cdot, z_i)\|_2^2 \end{array} \right.$$

with $\|\cdot\|_2^2$ denoting the norm per z -axis section:

$$\|f(\cdot, z_i)\|_2^2 = \int_{\mathbb{R}^2} f(x, y, z_i)^2 dx dy . \quad (2.11)$$

We call this the **atlas-informed** model. The first two prior terms of (2.10) control the smoothness of template deformation and the realigned target image stack, with the third keeping the rigid motions close to the identity. The last term is the “log-likelihood” conditioned on the other variables.

The optimization for the R^* rigid-motions is not decoupled across sections because of the smooth diffeomorphism of the LDDMM update and the Sobolev metric represented through

the difference operator across the z - sections. Clearly, the smooth diffeomorphism is able to interpolate through the measured target sectioning data when the restacking solution gives a relatively smooth target, as diffeomorphisms are spatially smooth with at least one derivative. The optimization of the vector field v^* corresponds to the LDDMM solution of Beg [1].

The principal algorithm used for solving this joint MAP-penalized likelihood problem alternates between fixing the rigid motions and solving LDDMM and fixing the diffeomorphism and solving for the rigid motions. This is described below in the following section.

When there is no atlas available this is equivalent to setting α_i small and becomes a MAP rigid motion restacking of the sections:

$$\operatorname{argmax}_{R_i, i=1, \dots} \sum_i \left(\log \pi(R_i) - \frac{1}{2} \|D_h I^R(\cdot, z_i)\|_2^2 \right) .$$

We term this the **atlas-free** model. The gradient of the rigid motions with respect to the components of translations t^x, t^y and rotation θ is defined in Gradients for Atlas Free Model. The registration is not independent across sections due to coupling through the Sobolev metric.

2.1.4 Iterative Algorithm for Joint Penalized Likelihood and MAP Estimator

Here we describe the details of the algorithm used for solving for the MAP/penalized-likelihood problem described above. The algorithm alternately fixes the set of rigid motions while updating LDDMM and fixes the diffeomorphism while updating the rigid motions.

Algorithm 1.

0. Initialize $\varphi^{new}, R^{new} \leftarrow \varphi^{init}, R^{init}, I^{old} \leftarrow J \circ R^{init}$.
1. Update $\varphi^{old} \leftarrow \varphi^{new}, R_i^{old} \leftarrow R_i^{new}, I^{old}(\cdot, z_i) \leftarrow I^{new}(\cdot, z_i), i = 1, \dots$.
2. Update LDDMM for diffeomorphic transformation of atlas coordinates:

$$v^{new} = \operatorname{argmax}_v - \frac{1}{2} \int_0^1 \|v_t\|_V^2 dt - \sum_i \alpha_i \|I^{R-old}(\cdot, z_i) - I_0 \circ \varphi_1^{v-1}(\cdot, z_i)\|^2, \quad (2.12)$$

$$\varphi^{new} = \int_0^1 v_t^{new} \circ \varphi_t^{new} dt + \operatorname{id}.$$

3. Deform atlas $I_0 \circ \varphi^{new-1}$ and generate new histology image stack:

$$\begin{aligned}
R^{new} &= \arg \max_{R_i, i=1, \dots} \sum_i (\log \pi(R_i) \\
&\quad - \frac{1}{2} \|D_h I^R(\cdot, z_i)\|_2^2 - \alpha_i \|I^R(\cdot, z_i) - I_0 \circ \varphi^{new-1}(\cdot, z_i)\|_2^2) ; \\
I^{R-new}(\cdot, z_i) &= J_i \circ R_i^{new}(\cdot), i = 1 \dots
\end{aligned} \tag{2.13}$$

4. Return to Step 1 until convergence criterion met.

The form of the gradients for the rigid motions is given in the following two sections for the atlas-free and atlas-informed models. The LDDMM update solutions are given by Beg [1].

2.1.5 Gradients for Atlas Free Model

We can write the gradient of E , the function to be maximized in Eqn. (2.10), with respect to the components of R (translation vector t and rotation matrix r parametrized by rotation angle θ and section number z), where ∇_X is the 2D in-plane gradient, σ_{JJ} is the weighting factor on the image smoothness prior. Rotations and translations are penalized by a regularization prior centered at identity ($\frac{\theta}{\sigma_\theta^2}$ and $\frac{t(z_i)}{\sigma_t^2}$, respectively), where σ_θ and σ_t are weighting factors on the rotation and translation priors arising as standard-deviations of the Gaussian

priors written out in Eqn. (2.9).

$$\nabla_r E = -\alpha(z_i) \frac{d^2}{dz^2} (J(r(\theta, z_i)x + t(z_i))) \nabla_X J(r(\theta, z_i)x + t(z_i)) \delta r(\theta, z_i)x + \frac{\theta}{\sigma_\theta^2} \quad (2.14)$$

$$\nabla_t E = -\alpha(z_i) \frac{d^2}{dz^2} (J(r(\theta, z_i)x + t(z_i))) r(\theta, z_i), \nabla_X J(r(\theta, z_i)x + t(z_i)) + \frac{t(z_i)}{\sigma_t^2} \quad (2.15)$$

Here the weight α_i plays the role of controlling the step size in the gradient algorithm rather than controlling the weight relative to the prior of the likelihood function as it does in the atlas-informed case. For image planes that are noisy, the step-size is small, approximately zero. These are derived more generally in the following section on the atlas-informed model's gradients.

2.1.6 Gradients for Atlas Informed Model

The minimization of the energy E_v of (2.12) in terms of the vector field is the LDDMM gradient of Beg [1]:

$$\begin{aligned} \nabla_v E_v(x, y) = \sum_i \int_{\mathbb{R}^2} K(x - x', y - y', z - z_i) |D\varphi_{t,1}| (I \circ \varphi_{t1} - I_0 \circ \varphi_t^{-1}) \\ \nabla(I_0 \circ \varphi_t^{-1})(x', y', z_i) dx' dy' . \end{aligned} \quad (2.16)$$

Variation of the Image Matching Term: The variation of $\int (I - I_0 \circ \varphi^{-1})^2 dx$ via perturbation $\varphi \rightarrow \varphi^\varepsilon = \varphi + \varepsilon \delta\varphi$ requires the inverse perturbation $\delta\varphi^{-1} = -(d\varphi)_{|\varphi^{-1}}^{-1} \delta\varphi|_{\varphi^{-1}}$, derived in (B.2) above. Then we have

$$\begin{aligned} \frac{d}{d\varepsilon} \int_{\mathbb{R}^3} (I - I_0 \circ \varphi^{\varepsilon^{-1}})^2 dx|_{\varepsilon=0} &= 2 \int_X (I - I_0 \circ \varphi^{-1}) \nabla(I_0)|_{\varphi^{-1}} \cdot (d\varphi)_{|\varphi^{-1}}^{-1} \delta\varphi|_{\varphi^{-1}} dx \\ &= 2 \int_X (I \circ \varphi - I_0) (d\varphi)^{-1T} \nabla I_0 |d\varphi| \cdot \delta\varphi dx . \end{aligned}$$

Rigid motion variations: Rigid motion minimization is standard for rigid registration in 2D and 3D images. Denoting $\|f_{\theta,t,z_i}\|^2 = \|J^R(\cdot, z_i) - I_0 \circ \varphi^{v^*^{-1}}(\cdot, z_i)\|_2^2$ to represent each rigid registration norm-square minimization within each histological plane, then

$$\begin{aligned} \nabla_\theta \|f_{\theta,t,z_i}\|^2 &= \int_{\mathbb{R}^2} 2f_{\theta,t,z_i}(\cdot) \frac{\partial_\theta f_{\theta,t,z_i}}{\partial \theta} dx dy ; \\ \nabla_t \|f_{\theta,t,z_i}\|^2 &= \int_{\mathbb{R}^2} 2f_{\theta,t,z_i}(\cdot) \nabla_t f dx dy . \end{aligned}$$

Here, we derive gradients for the energy functional with respect to rotation and translation parameters as these are generally relevant for tape-transfer histology. However, we note that this model is generalizable to any class of transforms in the restacking plane. The energy functional is written for target serially-section stack J , template I , r is a rotation matrix, t is the translation vector, σ_{JI} is a weighting factor on the matching term between template and target, σ_{JJ} is a weighting factor on the Sobolev term, and σ_r and σ_t are weighting factors on the rigid motion regularization that centers them at identity:

$$E_R = \int_{X(z)} \int_Z \frac{1}{2\sigma_{JI}^2} |I_{\varphi^{-1}}(x) - J(r(\theta, z)x + t(z))|^2 + \frac{1}{2\sigma_{JJ}^2} \left| \frac{d(J(r(\theta, z)x + t(z)))}{dz} \right|^2 dx dz + \frac{1}{2} \int_Z \frac{t(z)^2}{\sigma_t^2} dz + \frac{1}{2} \int_Z \frac{\theta(z)^2}{\sigma_r^2} dz \quad (2.17)$$

For simplicity, we write $I_{\varphi^{-1}} = I \circ \varphi^{-1}$. We again apply the method of coordinate descent and compute the gradient of this expression with respect to r and t . Take a perturbation on translation $t(z)$ such that $t_{\varepsilon\eta} \rightarrow t(z) + \varepsilon\eta(z)$:

$$E_R = \int_{Y(z)} \int_Z \frac{1}{2\sigma_{JI}^2} |I_{\varphi^{-1}}(x) - J(r(\theta, z)x + t(z) + \varepsilon\eta(z))|^2 + \frac{1}{2\sigma_{JJ}^2} \left| \frac{d(J(r(\theta, z)x + t(z) + \varepsilon\eta(z)))}{dz} \right|^2 dx dy dz + \frac{1}{2} \int_Z \frac{(t(z) + \varepsilon\eta(z))^2}{\sigma_t^2} dz + \frac{1}{2} \int_Z \frac{\theta(z)^2}{\sigma_r^2} dz \quad (2.18)$$

Take the Gateaux derivative with respect to ε :

$$\begin{aligned} \frac{d}{d\varepsilon} \Big|_{\varepsilon=0} E_R &= \int_{X(z)} \int_Z \frac{1}{\sigma_{JI}^2} (I_{\varphi^{-1}}(x) - J(r(\theta, z)x + t(z))) \nabla_X J(x + t(z)) \eta(z) \\ &\quad - \frac{1}{\sigma_{JJ}^2} \frac{d^2}{dz^2} (J(r(\theta, z)x + t(z))) (DJ)(r(\theta, z)x + t(z)) \eta(z) dx dz + \int_Z \frac{t(z)}{\sigma_t^2} \eta(z) dz \end{aligned} \quad (2.19)$$

$$\begin{aligned} &= \int_{X(z)} \frac{1}{\sigma_{JI}^2} (I_{\varphi^{-1}}(x) - J(r(\theta, z)x + t(z))) \nabla_X J(r(\theta, z)x + t(z)) \\ &\quad - \frac{1}{\sigma_{JJ}^2} \frac{d^2}{dz^2} (J(r(\theta, z)x + t(z))) r(\theta, z) \nabla_X J(r(\theta, z)x + t(z)) dx + \frac{t(z)}{\sigma_t^2} dz \end{aligned} \quad (2.20)$$

Above, we observe that $(DJ)(r(\theta, z)x + t(z)) = D(J(r(\theta, z)x + t(z)))r(\theta, z)^T = r(\theta, z) \nabla_X J(r(\theta, z)x + t(z))$ by the derivative chain rule. Therefore, the gradient with respect to the translation parameters is:

$$\begin{aligned} \nabla_{R,t} E(v, R; J) &= \left\langle \frac{1}{\sigma_{JI}^2} (I_{\varphi^{-1}}(x) - J(r(\theta, z)x + t(z))) - \frac{1}{\sigma_{JJ}^2} \frac{d^2}{dz^2} (J(r(\theta, z)x + t(z))) r(\theta, z), \right. \\ &\quad \left. \nabla_X J(r(\theta, z)x + t(z)) \right\rangle + \frac{t(z)}{\sigma_{reg_t}^2} \end{aligned} \quad (2.21)$$

Now we solve for the gradient with respect to rotation parameters. Take a perturbation on

rotation $r(\theta, z)$ such that $r_{\varepsilon\eta}(\theta, z) \rightarrow r(\theta + \varepsilon\eta(z), z)$. Note that for 2D rotation matrices, $r(\theta + \varepsilon\eta(z), z) = r(\theta, z)r(\varepsilon\eta(z), z)$:

$$\begin{aligned}
E_R &= \int_{X(z)} \int_Z \frac{1}{2\sigma_{JI}^2} |I_{\varphi^{-1}}(x) - J(r(\theta, z)r(\varepsilon\eta(z), z)x + t(z))|^2 + \\
&\quad \frac{1}{2\sigma_{JJ}^2} \left| \frac{d(J(r(\theta, z)r(\varepsilon\eta(z), z)x + t(z)))}{dz} \right|^2 dx dy dz + \frac{1}{2} \int_Z \frac{t(z)^2}{\sigma_t^2} dz + \frac{1}{2} \int_Z \frac{(\theta + \varepsilon\eta(z))^2}{\sigma_r^2} dz
\end{aligned} \tag{2.22}$$

Take the Gateaux derivative with respect to ε :

$$\begin{aligned}
\frac{d}{d\varepsilon} \Big|_{\varepsilon=0} E_R &= \int_{X(z)} \int_Z \frac{1}{\sigma_{JI}^2} (I_{\varphi^{-1}}(x) - J(r(\theta, z)x + t(z)))(DJ)(r(\theta, z)x + t(z)) \\
&\quad \frac{d}{d\varepsilon} r(\theta, z)r(\varepsilon\eta(z))x - \frac{1}{\sigma_{JJ}^2} \frac{d^2}{dz^2} (J(r(\theta, z)x + t(z)))(DJ)(r(\theta, z)x + t(z)) \frac{d}{d\varepsilon} r(\theta, z)r(\varepsilon\eta(z))x dx \\
&\quad + \int_Z \frac{\theta}{\sigma_r^2} \eta(z) dz \tag{2.23}
\end{aligned}$$

Observing that $\frac{d}{d\varepsilon} r(\theta, z)r(\varepsilon\eta(z))x = r(\theta, z)x\eta(z)$ where the perturbation direction $\eta(z) \rightarrow \delta r(\theta, z)$ and that the XY gradient term is derived from the chain rule $(DJ)(r(\theta, z)x + t(z))r(\theta, z) = D(I(r(\theta, z)x + t(z)))$:

$$\begin{aligned}
&= \int_{X(z)} \int_Z \frac{1}{\sigma_{JI}^2} (I_{\varphi^{-1}}(x) - J(r(\theta, z)x + t(z))) \nabla_X J(r(\theta, z)x + t(z)) \delta r(\theta, z)x - \\
&\quad \frac{1}{\sigma_{JJ}^2} \frac{d^2}{dz^2} (J(r(\theta, z)x + t(z))) \nabla_X J(r(\theta, z)x + t(z)) \delta r(\theta, z)x dx + \frac{\theta}{\sigma_r^2} \tag{2.24}
\end{aligned}$$

Therefore, the gradient with respect to the rotation parameters is:

$$\begin{aligned} \nabla_{R,r} E(v, R; J) = & \left\langle \frac{1}{\sigma_{JI}^2} (I_{\varphi^{-1}}(x) - J(r(\theta, z)x + t(z))) - \frac{1}{\sigma_{JJ}^2} \frac{d^2}{dz^2} (J(r(\theta, z)x + t(z))), \right. \\ & \left. \nabla_X J(r(\theta, z)x + t(z)) R \begin{bmatrix} 0 & 1 \\ -1 & 0 \end{bmatrix} x \right\rangle + \frac{\theta}{\sigma_{reg_r}^2} \end{aligned} \quad (2.25)$$

Where the X gradient term is expanded in matrix form for 2D sections as:

$$\nabla_X J(r(\theta, z)x + t(z)) \delta r(\theta, z) x = \left(-\frac{d}{dy} J, \frac{d}{dx} J \right) \begin{pmatrix} x \\ y \end{pmatrix} \quad (2.26)$$

2.1.7 Distances for Variational Methods

The variational methods described above require building distances between the mean fields and the histology stacks. In general, we perform guided histology reconstruction as described in the estimation problem above using the nissl-stained histology sections due to their anatomical clarity. The guiding image, I_0 , is generally an atlas image of the same modality but in some cases may be a different modality like ex-vivo MRI, in which case φ can be restricted to simpler transforms like rigid or affine deformations. Cross-modality matching is also required in 2D when co-registering structural Nissl-stained stacks with connective fluorescent imaging, or other stains. In the former case, as matching is performed

within modalities, we define a similarity metric based on squared error of intensities. In the latter case, cross-modal matching is driven by a mutual information similarity metric. The transformations for the additional stains/modalities are driven by the cross-modal metric.

To build correspondences between the histological stack of 2D sections $I^R(\cdot, z_i)$ and sections of the Nissl atlas or cross-modality MRI image $I_0(\cdot, z_i)$ we use a similarity metric based on either squared-error (same modality) as described in the above algorithm or mutual information (cross modality) as described by Kutten et al [128].

Squared-error within modality Define the error function between images $d : (I, J) \rightarrow R^+$ a positive squared-error function between images can be defined as the square of the Euclidean distance;

$$d(I, J) = \frac{1}{2} \|J(\cdot) - I(\cdot)\|_2^2 = \frac{1}{2} \sum_{x,y,z} |I(x, y, z) - J(x, y, z)|^2 .$$

Mutual information Across modalities, $p_{I,J}$ is the empirical estimate of the joint histogram density and p_I, p_J are the corresponding marginals. The mutual information $d(I, J)$ is given by

$$d(I, J) = - \sum_{\eta} \sum_{\psi} p_{I,J}(\eta, \psi) \log \left(\frac{p_{I,J}(\eta, \psi)}{p_I(\eta)p_J(\psi)} \right) . \quad (2.27)$$

2.1.8 Diffeomorphometry of Histological Procedures

The embedding of our algorithms into the diffeomorphic random orbit model described here allows the quantification of metric distances between trajectories and shapes within the same orbit. We demonstrate the advantage of this property by performing the first localized quantitative analysis of deformative effects at each stage of the histology process (the preparatory and the sectioning processes). Using Beg's volume-to-volume LDDMM model with the cross-modal metric defined in the previous section, we compute transformations between the different coordinate spaces associated to in-vivo, ex-vivo, and histology stack produced by guided reconstruction, thus separating the deformative effects of the preparatory process from the sectioning process. In order to quantify the non-linear distortion between these coordinate spaces, we examine the first fundamental form of the mapping computed by the above method determines how vectors are transformed under mapping between coordinate systems and is specified by the Jacobian matrix ($\partial_X \varphi$).

$$\partial_X \varphi(x, y, z) = \begin{pmatrix} \frac{\partial \varphi_1(x, y, z)}{\partial x} & \frac{\partial \varphi_2(x, y, z)}{\partial x} & \frac{\partial \varphi_3(x, y, z)}{\partial x} \\ \frac{\partial \varphi_1(x, y, z)}{\partial y} & \frac{\partial \varphi_2(x, y, z)}{\partial y} & \frac{\partial \varphi_3(x, y, z)}{\partial y} \\ \frac{\partial \varphi_1(x, y, z)}{\partial z} & \frac{\partial \varphi_2(x, y, z)}{\partial z} & \frac{\partial \varphi_3(x, y, z)}{\partial z} \end{pmatrix}. \quad (2.28)$$

The determinant $|\det \partial_X \varphi|$ and its logarithm are fundamental measures of coordinate change and in the comparative study of the in-vivo, ex-vivo, and histology coordinate spaces, directly measures the amount of metric distortion within the same subject, and the change

in measure across coordinate systems of different subjects. Naturally, the mapping between each coordinate space may contain a rigid 3D component which we exclude from our morphometric measurement. The non-rigid component of the 3D distortion caused by the histology processing is isolated by performing affine registrations between each coordinate space as a pre-processing step to diffeomorphic registration. The scale change associated with the determinant of the affine transform matrix is included in the reported percent scale change.

2.1.9 Serial Section Shape Interpolation

We make one final extension of our model to enable estimation of diffeomorphic trajectories along the sectioning axis of our reconstructed volumes. This can be a useful tool for upsampling highly anisotropic image volumes like histology or serial-section MRI. We can view this problem as equivalent to estimation of a statistical average of shapes in images. This becomes a natural extension as it is a direct application of the computational anatomy random orbit model framework of Bayesian template estimation, first described in [123]. Template estimation is traditionally employed to compute atlas images which are minimally distant (in terms of some similarity metric) from a sample of some population of images. We take the same maximum a posteriori approach here, where our population subjects or observations I_i are the neighboring sections to a desired position to be upsampled.

We define our estimate of the data at an unobserved position as a Jacobian-weighted mean of the population along their diffeomorphic trajectories. The diffeomorphic trajectories are

solved by the minimization in Eqn. (2.12). In the classic template estimation case, these minimizations are performed iteratively such that population subjects are mapped to an iterative estimate of the population's centroid or mean. The per-iteration estimate of the mean image is given by a weighted sum at the endpoints of these trajectories:

$$\bar{I}^{(k+1)} = \frac{\sum_{i=1}^N I_i \circ \varphi_{v_i^{(k)}} |D\varphi_{v_i^{(k)}}|}{\sum_{i=1}^N |D\varphi_{v_i^{(k)}}|} \quad (2.29)$$

where $\varphi_{v_i^{(k)}}$ is the diffeomorphism of the velocity field v for observation i at iteration k , N is the number of population subjects, and D indicates the Jacobian determinant of φ in space. The notion of weighting by the Jacobian determinant $|D\varphi_{v_i^{(k)}}|$ is a natural one as the Jacobian encapsulates the change of coordinates from each observation to the mean. It is, in a sense, weighting the importance of the observations - for instance, if a pixel in the mean/centroid space maps to many pixels in an observation, that pixel should be more heavily weighted in the computation of the average image by a degree commensurate to its importance. In the original expectation-maximization formulation, this process is repeated until the mean image converges to the desired minimally distant population mean.

In the case of image slice upsampling, the two observed slices neighboring the z -position where we want to upsample the volume are the only two population “subjects” or “observations”. The mean along the diffeomorphic trajectory between a pair of images is a simpler problem which does not require the notion of a large population's centroid and can be com-

puted in a single shot without an iterative procedure. As such, we define a weighted mean

$$\bar{I}_r = \frac{I_0(\varphi_0^{0, \frac{r}{R}}) |D\varphi_0^{0, \frac{r}{R}}| (1 - \frac{r}{R}) + I_1(\varphi_1^{1, \frac{r}{R}}) |D\varphi_1^{1, \frac{r}{R}}| \frac{r}{R}}{|D\varphi_0^{0, \frac{r}{R}}| (1 - \frac{r}{R}) + |D\varphi_1^{1, \frac{r}{R}}| \frac{r}{R}} \quad (2.30)$$

where R is the z -axis distance between two observed slices I_0 and I_1 and r is the z -axis distance from I_0 at which to estimate the interpolation between the observations. We use Eqn. (2.30) to directly compute the the midpoint (or any arbitrary point) along the trajectory between I_0 and I_1 in a single iteration. We expect the flow to be symmetric in time, so we constrain φ as in [38]. This formulation is a modification of the Jacobian-weighted mean of Eqn (2.29) where the population observations are averaged at an intermediate point determined by the diffeomorphic trajectory rather than the estimation of a population's centroid. Here, $\varphi_0^{a,b}$ is the diffeomorphism computed from the time-varying velocity field v_t parameterizing (2.12) from time $t = a$ to time $t = b$ for the mapping of I_0 to I_1 ($\varphi_1^{a,b}$ being the same for I_1 to I_0).

2.1.10 Software Implementation

A software pipeline that performs start-to-finish volume reconstruction operations was originally implemented in C++ and MATLAB for processing on a high performance computing cluster. This pipeline was later upgraded to a full implementation in PyTorch, optimized on run on GPU or CPU (open-source version available at <https://github.com/brianlee324/torch-1ddmm>). To date, the pipeline has been used to reconstruct thousands of mouse brains

and tens of marmoset brains as well as perform registration into common coordinate spaces.

The general pipeline workflow is illustrated in Fig 2.3. The general order of operations in-

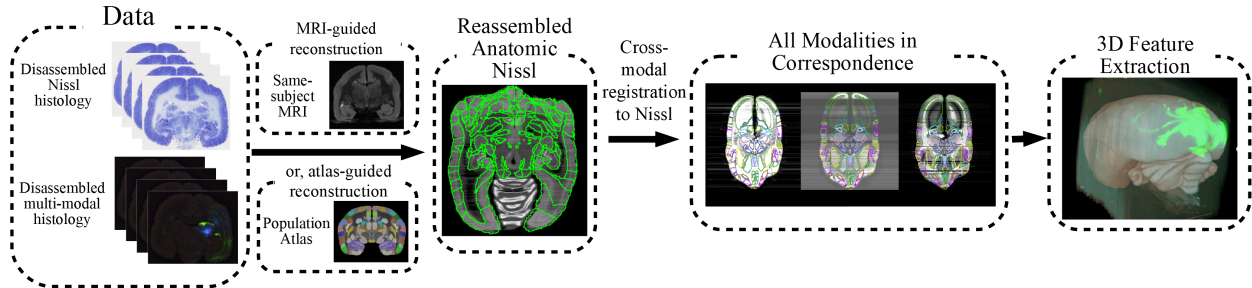


Figure 2.3: **Histology registration pipeline workflow.** Reconstruction pipeline workflow from multi-modality histological image sections to segmented data and connectivity analysis. The proposed workflow starts with disassembled multimodal histology and reconstructs 3D Nissl-stained volumes using either MRI or atlas guidance. Cross-modal reconstructions are then achieved by registration to the corresponding Nissl reconstruction. Segmentations are obtained as a side product of atlas registration. In the final step, connectivity-related features are extracted from the 3D volumes in a common coordinate space.

volves first performing the volume reconstruction operations on the anatomic Nissl stack, using either atlas guidance or same-subject reference guidance. The reconstruction process simultaneously produces the curvature-preserved Nissl volume as well as the segmentations inherited from the joint atlas-mapping component. Then, the reconstructed Nissl volume is used as a reference to cross-modally reconstruct all other modalities, such as fluorescence microscopy, bringing all modalities into a common coordinate space with segmentations where further downstream analysis can occur.

The run-time/complexity for the volume LDDMM algorithm has complexity order $n_T N_{vox} \log(N_{vox})$, where n_T is the number of steps for integrating the time varying velocity field, and N_{vox} is the

total number of voxels. The slice based portion of the code is order N_{vox} . While the FFTs are order $N \log N$, in practice most computation time is spent during linear interpolation (order N). A start-to-finish example Jupyter notebook of GPU-accelerated MRI-guided reconstruction has been posted at https://github.com/brianlee324/torch-lddmm/blob/master/examples/8_Section_Alignment_to_Reference.ipynb in which processing time was a total of 47 minutes for image volumes of dimension 323x473x340 (51,944,860 voxels). In contrast, the same operations performed on a 16-core CPU would consume over 30 hours.

2.2 Results

We apply the algorithms described here for volume reconstruction in a number of datasets, including simulated data, the Mouse Brain Architecture Project mouse histology dataset, the Brain/MINDS marmoset brain histology dataset, a mouse cardiac MRI dataset, and human brain histology. In each section below we will describe the data and show results of volume reconstruction.

2.2.1 Evaluation of Reconstruction Accuracy

Binary Phantom with Curvature Distortion

The model was applied to binary image phantoms in order to examine the “curvature” problem in which a 3D curved object cannot be accurately reconstructed after being sectioned.

This is illustrated in Fig 2.4. We produced sections through the 3D phantom, applying the atlas-free and the atlas-informed models. The results from the atlas-free algorithm in which the sections are aligned based on the Sobolev smoothness followed by mapping of the atlas via LDDMM are summarized in Fig 2.4c. The atlas-free section alignment reconstructs the target stack, demonstrating a cylindrical reconstruction rather than the curved template shape, followed by LDDMM alignment $I_0 \circ \varphi^{-1}$. This illustrates the curvature issue. The atlas coordinate grid is transformed significantly (bottom right of Fig 2.4c) in order to match the target. Despite this significant deformation, there is some residual error in the atlas-to-target mapping with the remaining tendrils where the ends of the phantom did not shrink inwards. Here, the energy required to push the ends of the atlas inwards was greater than the potential image matching improvement.

Shown in Fig 2.4d is the atlas-informed solution. The bottom row shows that simultaneously solving for reconstruction and registration parameters allows for more consistent stack reconstruction of the target resulting from the influence of the smooth deformation of the template onto the target in the joint solution.

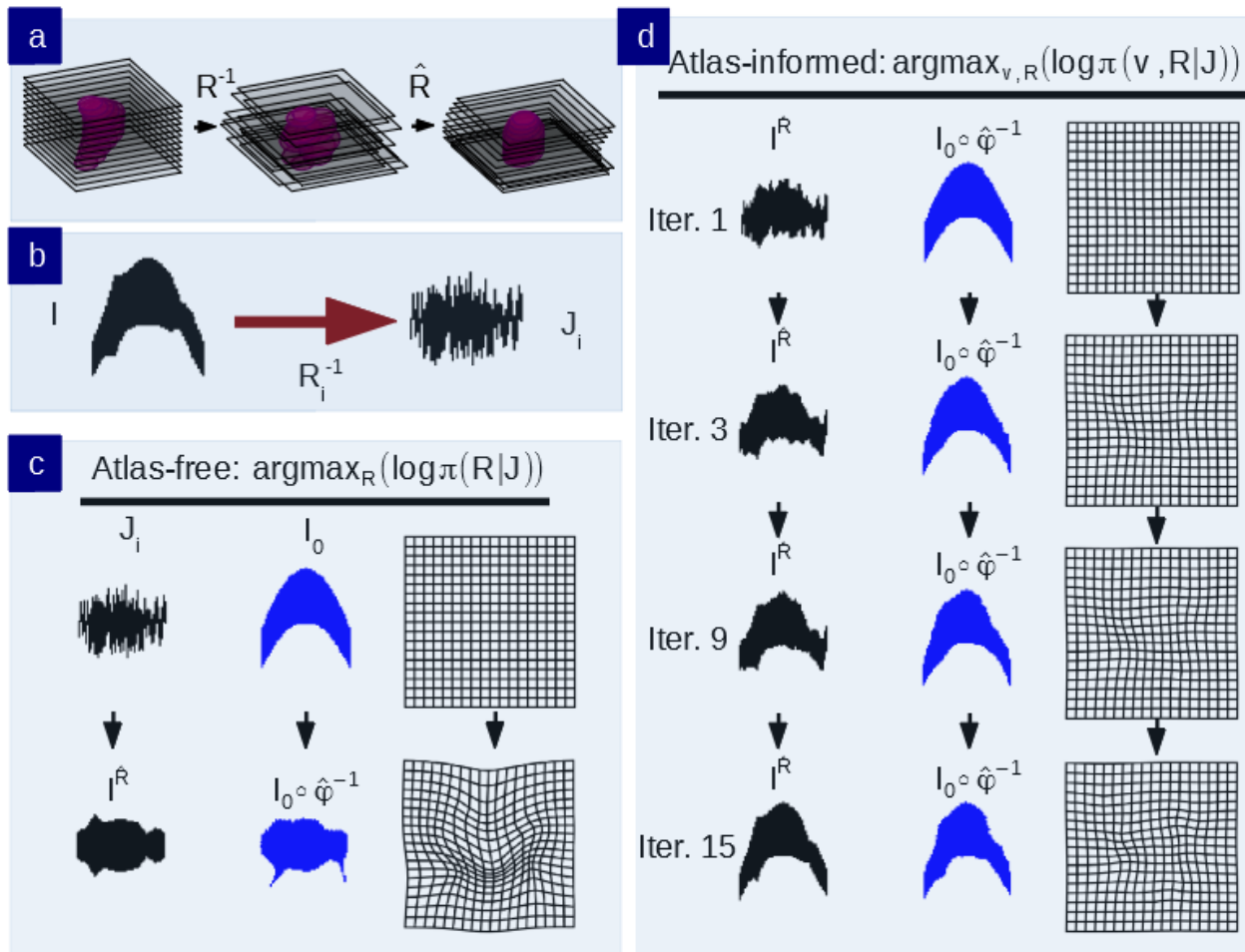


Figure 2.4: **Comparison of atlas-free and atlas-informed models in simulated binary phantom.** a) An illustration of the classic curvature reconstruction problem. b) The unobserved 3D-phantom is randomly sectioned and observed as $J_i, i = 1, \dots, n$. c) Reconstruction of the histological stack using the atlas-free method. The top row shows the histological stack and atlas. The bottom row shows the reconstructed histological stack $I^{\hat{R}}$ alongside the deformed phantom atlas $I = I_0 \circ \varphi^{-1}$ which has been mapped to histological sections, and the diffeomorphic change of coordinates $\hat{\varphi}^{-1}$. d) Reconstruction of phantom using the atlas-informed model. Each row depicts iterations of the reconstructed histological stack $I^{\hat{R}}$ alongside the deformed atlas $I = I_0 \circ \hat{\varphi}^{-1}$ and deformed coordinates. The bottom row is the convergence point of the algorithm.

These results are depicted by the motions of the atlas coordinate grids when deforming

onto the targets in Fig 2.5. Tandem optimization of section alignment parameters and diffeomorphisms produces a nonlinear mapping with lower metric cost (Fig 2.5c is less warped than Fig 2.5b).

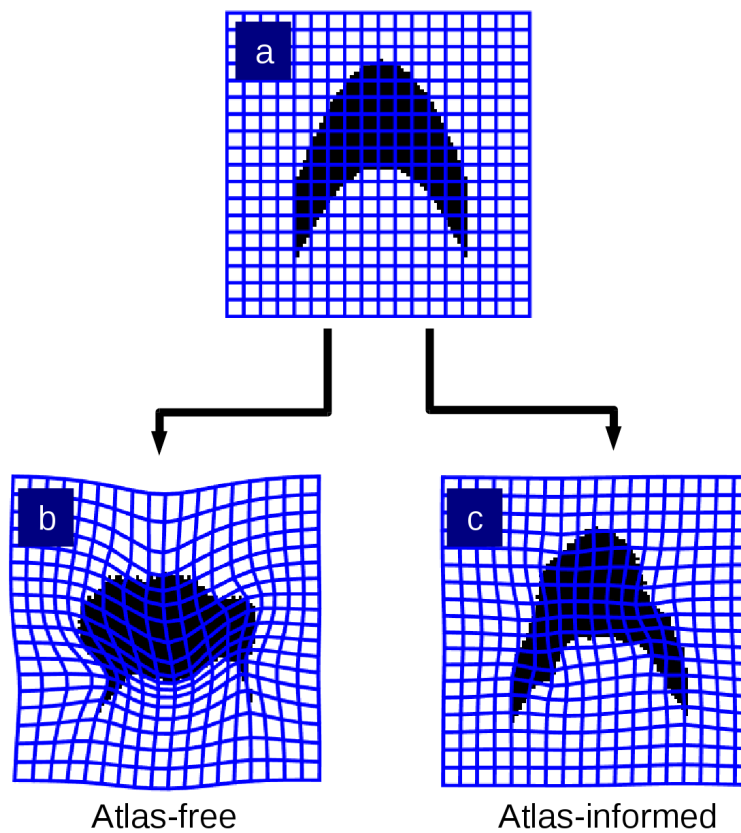


Figure 2.5: **Comparison of resulting diffeomorphic transformation of atlas phantoms.** The warped coordinate grids illustrate the difference in the mapping deformation from the atlas-free methods from (A) to histology stack target (B) versus the atlas-informed algorithm which produces (C).

Simulated jitter on the Allen Atlas

A similar experiment was performed using the Allen mouse brain atlas as the 3D phantom. A target histology stack was generated by sectioning the Allen atlas in simulation and applying random rigid transforms to its coronal sections. The atlas images were sampled at 40 μ m isotropic voxels. This is depicted in Fig 2.6a. A simulated atlas was generated by applying a given random diffeomorphism to the Allen atlas. This random diffeomorphism is depicted in Fig 2.6c. The histology stacks were then reconstructed and diffeomorphic transformations generated between the atlas and target stacks using both models, intending to recover both the unknown rigid transforms from Fig 2.6a and the unknown diffeomorphism from Fig 2.6c. Fig 2.6b shows the atlas-free method (bottom left) compared to the atlas-informed method (bottom right). The atlas-informed method nearly reproduces the original coordinates whereas the atlas-free method drifts away from the original coordinates. Note that although the diffeomorphisms are not identical, this does not necessarily indicate segmentation error as small differences in stack alignment can be compensated for by nonlinear registration during atlas-mapping.

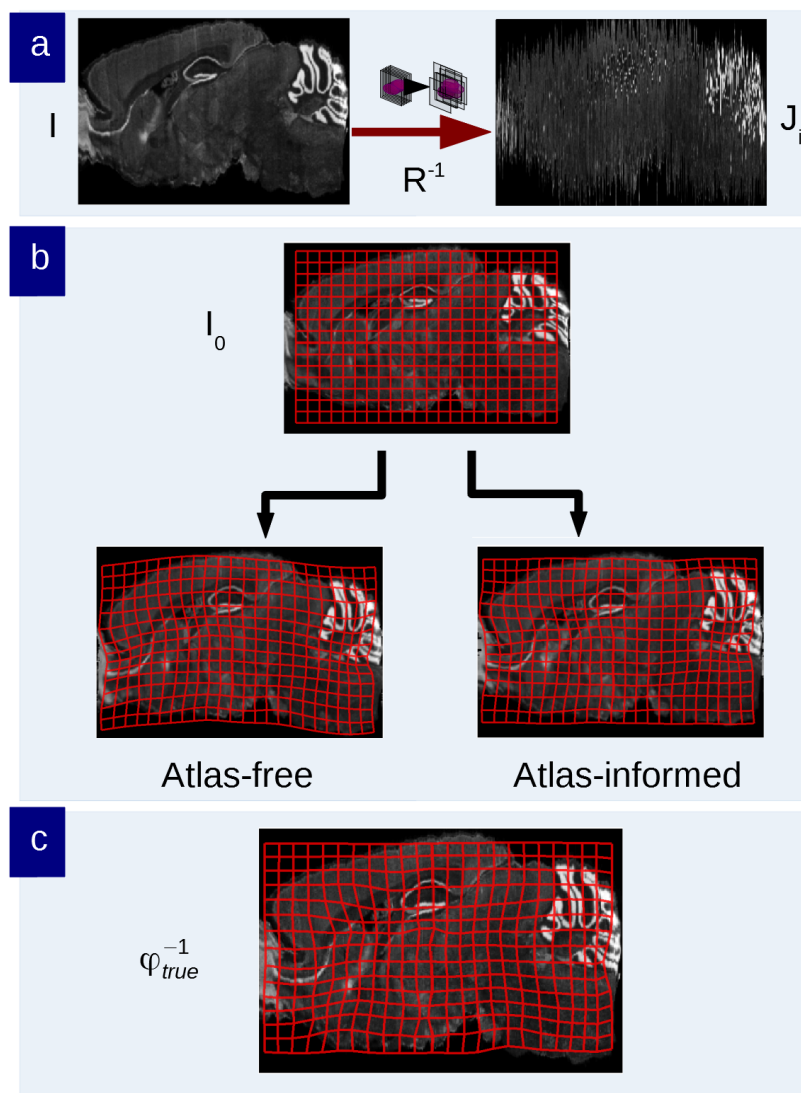


Figure 2.6: **Atlas phantom simulation to validate recovery of sectioning parameters and diffeomorphic shape difference.** a) The ground truth target I is sectioned to generate the observed target J_i . b) Transformed grids illustrating the brain phantom atlas (top) shown mapped onto the histological stack using the atlas-free algorithm (bottom left) and the atlas-informed algorithm (bottom right). c) The ground truth diffeomorphism to be recovered.

Simulated Bias and Variance Statistics

Figs 2.7 and 2.8 show results quantifying the bias and variance of the joint estimation of the diffeomorphism transformation and the rigid motion jitter in simulation. Eqn. (2.2) was simulated over a range of Gaussian white noise selections while simultaneously varying the jitter rigid motions of the sections along with multiple deformations of shearing applied to the template I_0 . Shearing produced images where each section was successively offset by 0.25 pixels in both x and y directions, cumulatively producing the “shear” effect illustrated in Fig 2.7. Fig 2.8a keeps the stack jitter fixed and varies the noise levels; Fig 2.8b varies the stack jitter. The random rigid motion jitter was normally distributed $(t_x, t_y) \sim \mathcal{N}(\mu = 0, \sigma^2 = 36)$, $\theta \sim \mathcal{N}(\mu = 0, \sigma^2 = 100)$ in pixel units. The RMSE, bias, and standard deviation of the estimated parameters were computed in each experiment and plotted as a function of error units versus noise level. 500 simulations per experiment were performed.

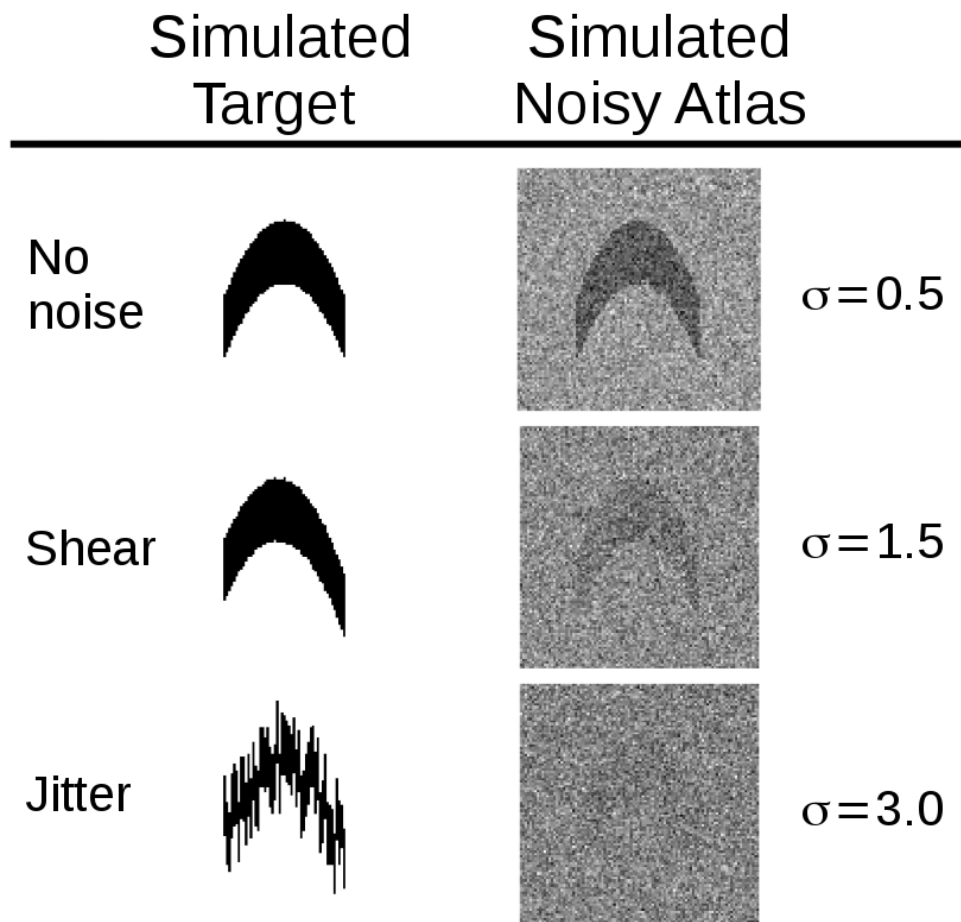


Figure 2.7: **Simulated noise on a binary image phantom.** Left column shows phantom for identity, shearing, and jitter of sections (successive rows); right column shows Gaussian white noise added to the atlas at various standard deviations.

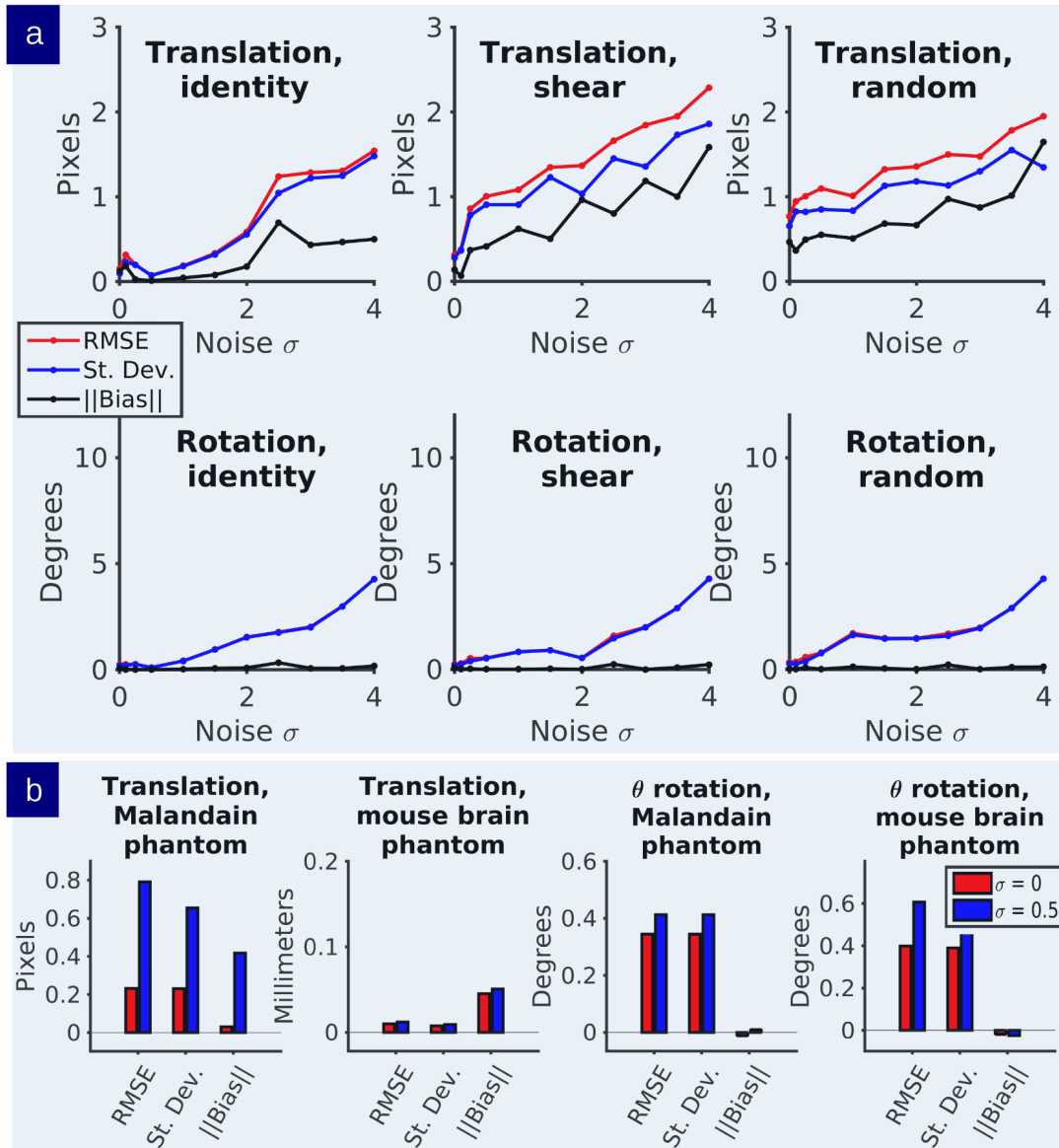


Figure 2.8: **Evaluation of estimator MSE, variance, and bias.** a) Statistics on the translation-rotation estimators for noise levels varying initial conditions. b) Statistics on the rigid motion estimators where the section jitter was added in a random fashion.

In each experiment, estimator accuracy is preserved up to high noise levels. At typical noise levels ($\sigma \leq 0.5$), we observe subpixel RMSE and small bias. Fig 2.8b shows that the rotation estimator is virtually unbiased whereas the translation estimator does have small subvoxel bias. It is likely that more rotational error is accounted for by section realignment than deformable mapping, whereas both play a relatively balanced role in translation correction. Small motions are ill-posed in that small rigid-motions can accommodate small atlas deformation. Fig 2.8c (top row) shows the case where there is jitter in the target stack. Estimator statistics are computed in each of these cases showing similar subpixel errors.

A similar analysis was performed for the Allen atlas brain phantom simulations. The reconstruction RMSE observed in the brain phantom simulation (bottom row of Fig 2.8c) is lower than that observed in the simple curved phantom in pixels. It is likely that this is due to the presence of more contour lines in grayscale images versus binary images. These additional features allow for more accurate distinction of matching error than simpler images with small numbers of distinct level lines. This is consistent with the demonstration in [125] showing that the stabilizer of the group corresponding to vector fields tangent to the level lines of the image cannot be uniquely identified or retrieved via any mapping methods that look at color or contrast of the image as the identifying feature.

2.2.2 Evaluation of Registration Accuracy

Although the performance of LDDMM is well described in the literature, we additionally evaluate the accuracy of our multi-modal 3D-to-3D registration model by identifying eight landmarks in our marmoset brain dataset drawn from the Brain/MINDS study described below (see Table 2.1 for summary of landmarks and description of their identification, see Section 2.2.4 for description of dataset), six of which are drawn from the Brain/MINDS study [129]: center of the anterior commissure, mid-sagittal anterior corpus callosum, mid-sagittal posterior corpus callosum, left and right anterior dorsal lateral geniculate nucleus. We identify two additional landmarks of our own, the meeting of the left and right lateral sulcus with the cortical surface at the anterior-most point. These eight landmarks are manually identified across all in-vivo MRI, ex-vivo MRI, and nissl reconstructions in our distortion quantification dataset.

The Brain/MINDS dataset is ideal for this analysis as it includes four coordinate spaces: in-vivo, ex-vivo, histology reconstruction, and atlas. We evaluate the accuracy of all three mappings that connect these coordinate spaces. An analysis of mean landmark transfer accuracy across all 15 subjects is performed on the three mappings. We report an average transfer accuracy across all eight landmarks of 0.2602 mm for the atlas to nissl reconstruction mapping, 0.2319 mm for the ex-vivo MRI to nissl reconstruction mapping, and 0.3487 mm for the in-vivo MRI to ex-vivo MRI mapping. Both mappings used to quantify tissue distortions have landmark transfer error of 1-2 voxels for all landmarks, which we consider to be within

the error range expected for human landmark identification and transform interpolation.

Sample image overlaps resulting from registration warps are displayed in Figure 2.9.

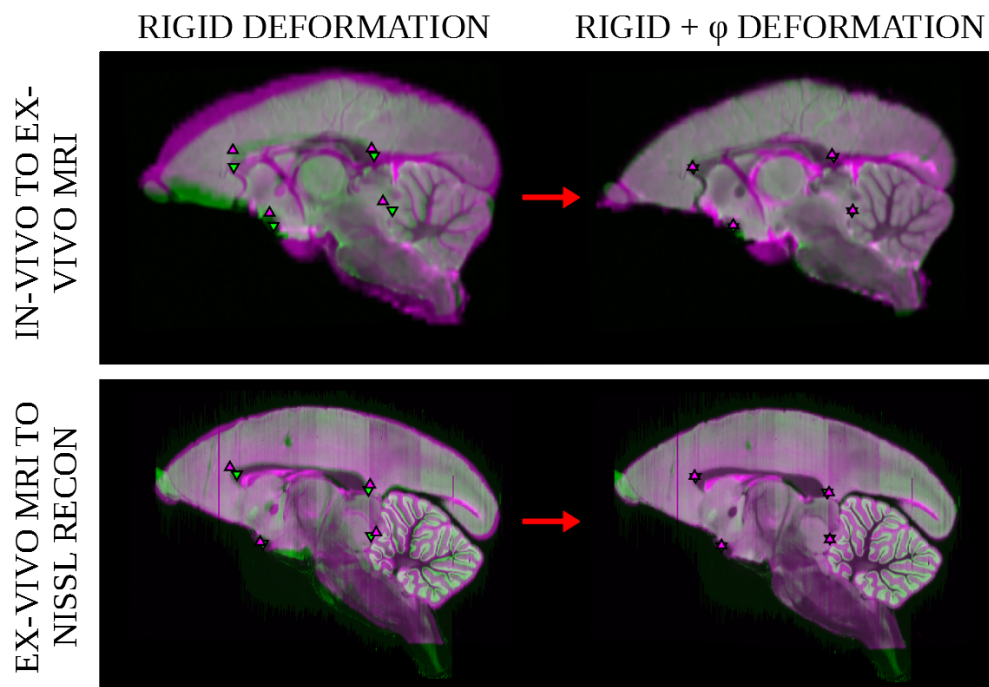


Figure 2.9: **Image overlap after volume to volume registration.** Registration accuracy was measured to validate quantitative distortion measurements. The top row shows overlap of a subject’s in-vivo MRI (magenta) mapped to the ex-vivo MRI (green) and the bottom row shows overlap of a subject’s ex-vivo MRI (magenta) mapped to the nissl reconstruction (green). Landmarks located near the mid-sagittal plane from the landmark transfer analysis are overlaid on each image: posterior and anterior corpus callosum, anterior commissure, and the fastidium of the fourth ventricle.

Landmark	Location Description	Transfer Accuracy: In-vivo to Ex-vivo (mm)	Transfer Accuracy: Ex-vivo to Nissl (mm)	Transfer Accuracy: Atlas to Nissl (mm)
Dorsal lateral geniculate nucleus (left)	Posterior-most point of left dorsal lateral geniculate nucleus in coronal view	0.2432	0.1615	0.1789
Dorsal lateral geniculate nucleus (right)	Posterior-most point of right dorsal lateral geniculate nucleus in coronal view	0.2411	0.1372	0.2106
Anterior commissure	Mid-sagittal anterior-most point of the anterior commissure	0.3632	0.1302	0.1866
Corpus callosum, anterior	Anterior-most point of the corpus callosum in mid-sagittal plane	0.4326	0.2859	0.1625
Corpus callosum, posterior	Posterior-most point of the corpus callosum in mid-sagittal plane	0.2875	0.3486	0.2648
Lateral sulcus (left)	Posterior-most intersection of left lateral sulcus with cortical surface	0.4939	0.3290	0.4156
Lateral sulcus (right)	Posterior-most intersection of right lateral sulcus with cortical surface	0.5201	0.3578	0.4887
Fastidium of fourth ventricle	Mid-sagittal point of the fastigium of the fourth ventricle	0.2083	0.1053	0.1742

Table 2.1: Summary of landmarks selected for registration accuracy evaluation alongside mean landmark transfer accuracy across 15 subjects.

2.2.3 Atlas-Informed Volume Reconstruction of Mouse Brain Architecture Project Data

Our method was implemented to support the Mouse Brain Architecture Project based at Cold Spring Harbor Laboratory, which contains thousands of mouse brain histology volumes. Here, we use the Allen Institute’s mouse brain atlas [124] (CCF 2017) as the template coordinate space. The experimental workflow generating the data utilizes a tape transfer technique [130], allowing for the sections to maintain geometrical rigidity within section and also allowing for physically disjoint components to maintain their spatial relations. The tape method ensures that the number of missing sections is minimal, with serial sections cut at a thickness of 20 μm and alternate sections subjected to Nissl staining alongside staining with histochemical or fluorescent label. These Nissl stained sections form the basis of alignment to a Nissl whole-brain reference atlas.

We selected specific targets which were prone to poor registration due to image intensity local minima. In particular, structures like the cerebellum tend to be difficult to register accurately due to their folded nature; one fold can easily be mistaken for the adjacent fold, and if the target and atlas are not well initialized, the deformation required to flow one fold onto another can have a high metric cost. We are also interested in inspecting lower-contrast structures like the corpus callosum, which may be poorly registered due to local minima in other nearby bright structures. We also evaluate our mapping quality in the hippocampal region, which is one of the most relevant regions for the study of neurodegenerative diseases.

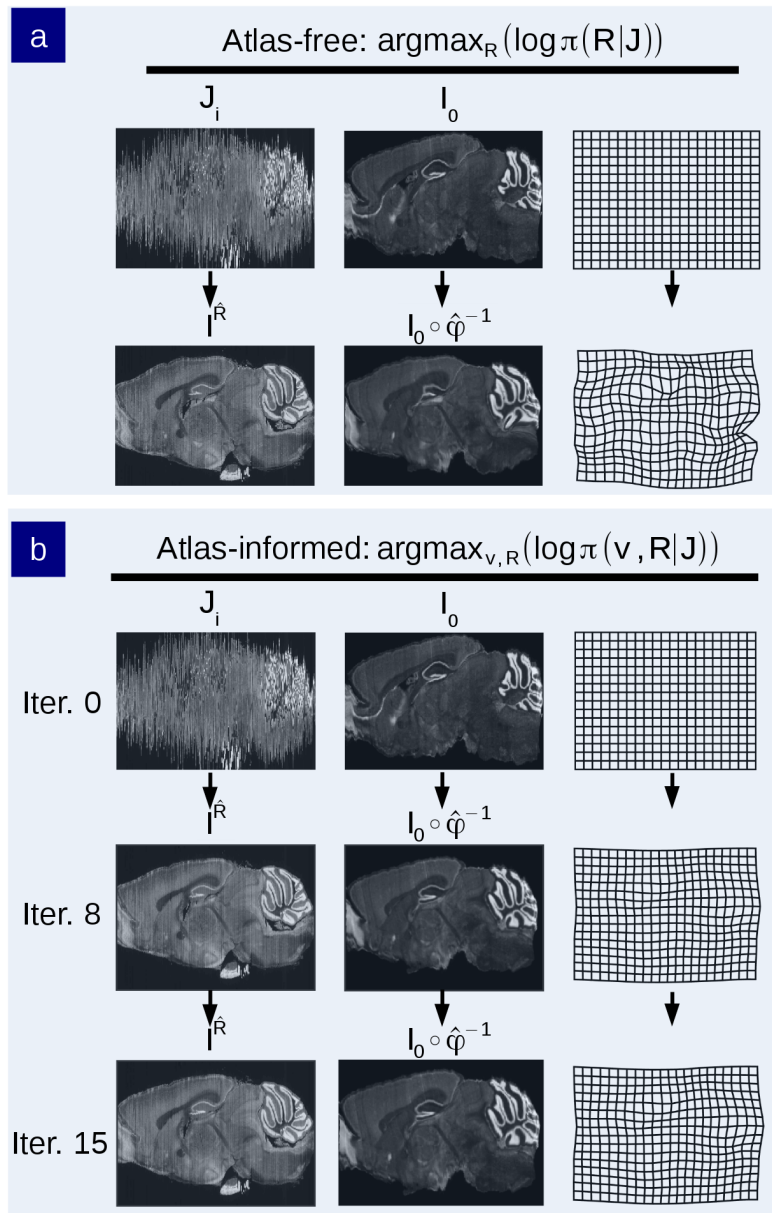


Figure 2.10: **Comparison of reconstruction and mapping using atlas-free and atlas-informed models on data from the MBAP database.** a) Reconstruction of an MBA Nissl-stained brain histological stack using the atlas-free method. Top row shows the histological stack and Allen mouse brain atlas. Bottom row shows the reconstructed histological stack $I^{\hat{R}}$ alongside the deformed phantom atlas I , and the diffeomorphic change of coordinates $\hat{\varphi}^{-1}$. b) Reconstruction using the atlas-free method. Top row shows the histological stack and Allen mouse brain atlas. Middle row depicts intermediate iterations of the reconstructed stack $I^{\hat{R}}$ alongside the deformed atlas $I_0 \circ \hat{\varphi}^{-1}$ and coordinate grid. Bottom row shows the convergence point of algorithm.

The reconstructed histological target stack in the atlas-informed model shown in Fig 2.10a takes on the shape of the atlas but is prone to reconstruction artifacts. The deformation grids produced by the atlas-informed mapping is much smoother and has many fewer wrinkles than the atlas-free mapping. This is seen clearly in Fig 2.11.

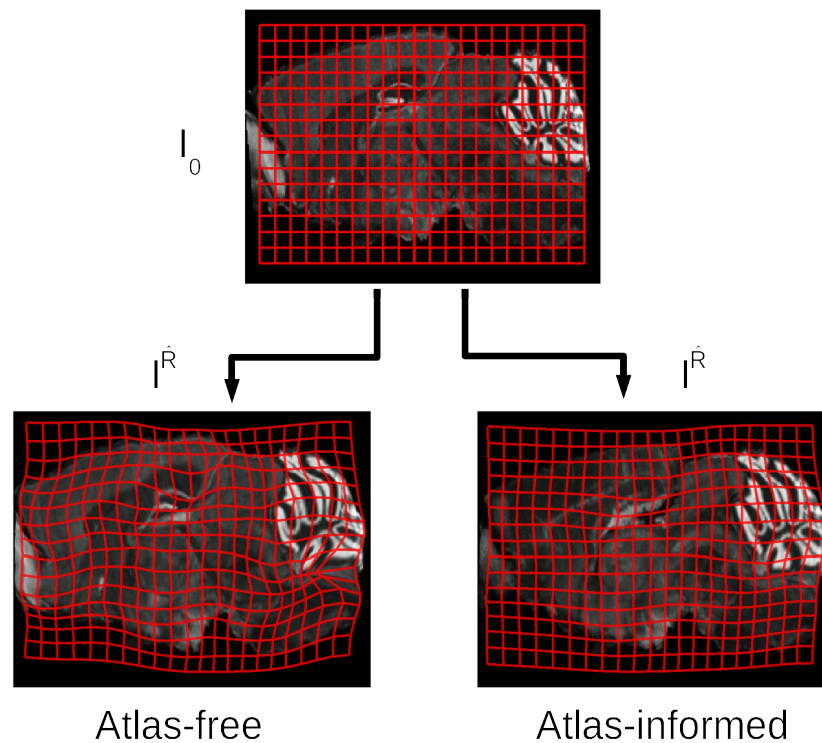


Figure 2.11: **Comparison of diffeomorphic transformation recovered from atlas-free and atlas-informed models.** The warped grids illustrate the difference in the mapping deformation from atlas (top) to target using the atlas-free method (bottom left) versus the atlas-informed method (bottom right), performed on real brain data from the MBA Project.

Fig 2.12 shows examples of improved segmentations in selected regions of the brain. The atlas-informed model generates more accurate segmentation results and produces smoother mappings as exhibited by the less wrinkled and distorted grids (bottom row b), showing

more consistent results throughout the MBAP dataset.

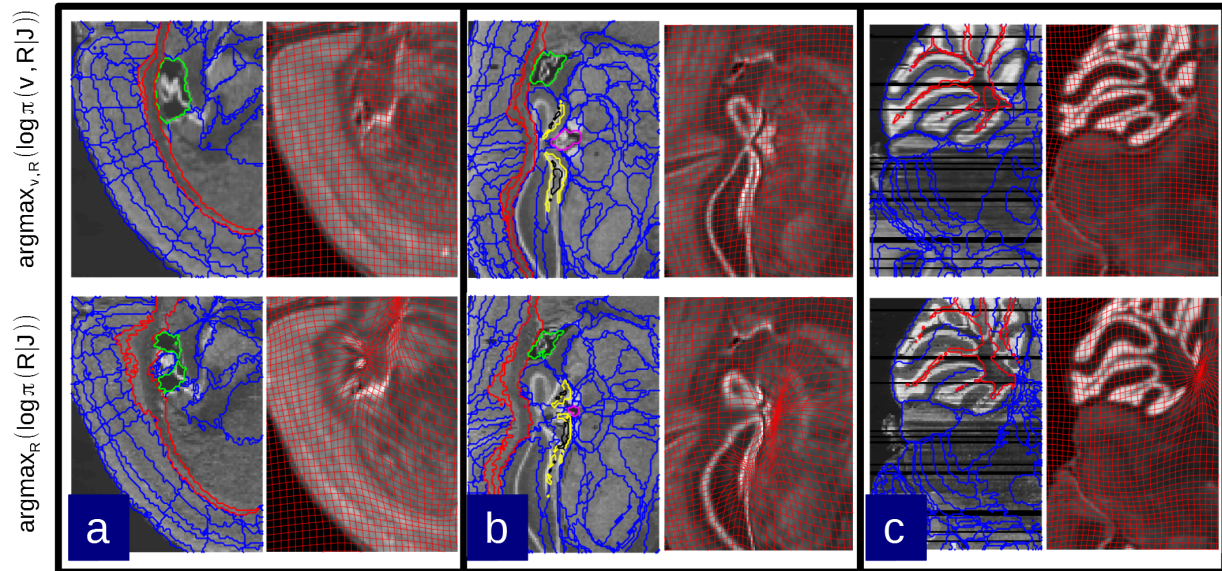


Figure 2.12: Selected regions of the brain segmented by the atlas-informed and atlas-free models carry the label map from the Allen atlas under the computed diffeomorphism. The bottom row shows several examples where optimization of the atlas-free solution is trapped in false minima due to folded or low-contrast structures. The top row shows correction by the atlas-informed algorithm. A) The corpus callosum and lateral ventricle. B) The dentate gyrus, corpus callosum, and lateral ventricle. C) The cerebellar white matter.

2.2.4 MRI-Guided Volume Reconstruction of Brain/MINDS Marmoset Histology Data

We additionally construct a pipeline to support analysis of the Brain/MINDS Marmoset Brain Architecture Project. We apply our methodology to a dataset of marmoset brains obtained as part of the RIKEN Brain/MINDS project and demonstrate solutions to the multi-modal stack reconstruction problem as well as robust atlas mapping results across

four modalities. The Brain/MINDS dataset was prepared using a high throughput histological and image processing pipeline, described in [131]. Briefly, each individual marmoset brain dataset consists of high resolution (9.4T) MRI scans (both in-vivo and ex-vivo post perfusion/extraction/fixation preparations) and high resolution images of a series of brain sections that have undergone histological processing to stain for Nissl substance, Myelin, Fluorescent neuronal tracers and the expression of Cholera toxin B (CTB). The in-vivo MRI was acquired from the marmosets prior to any experiments at a resolution of $0.269 \text{ mm} * 0.269 \text{ mm} * 0.539 \text{ mm}$ per voxel. The ex-vivo MRI was acquired after the injection of tracers, the incubation period, perfusion, and fixation at a resolution of $0.1 \text{ mm} * 0.1 \text{ mm} * 0.2 \text{ mm}$ per voxel. The histological sections were imaged after sucrose cryoprotection, freezing, and cryo-sectioning. For simplicity, we refer to the procedures that occur between the in-vivo and ex-vivo MRI acquisitions as the “preparatory processes” and the procedures that occur between ex-vivo MRI acquisition and histology as the “sectioning process”. The histological image data was originally acquired at $0.46 \mu\text{m}$ in-plane resolution with $20 \mu\text{m}$ section thickness (alternating through four stains resulting in $80 \mu\text{m}$ gap between sections of a single modality, resulting in a $\sim 174\text{x}$ factor of anisotropy between XY and Z directions) and was downsampled to $80 \mu\text{m}$ in-plane resolution for computational purposes. We additionally use the Brain/MINDS marmoset brain atlas [129] which includes a nissl-stained 3D volume as the template coordinate space in our processing pipeline.

The histological restacking was guided by a same-subject ex-vivo MRI scan where avail-

able. These informed variational solutions were optimized for each of fifteen brains in the Brain/MINDS dataset and we observed accurate estimates of the reconstructed stacks consistent with simulations previously reported in the above sections and in previous work [132]. Segmentations were projected from the registered Brain/MINDS atlas as an auxiliary output of the reconstruction workflow and sample segmentation and process detection results are depicted in Fig 2.13 for an individual marmoset brain. Segmentation of the fluorescence, myelin, and CTB images was achieved using the same reconstruction framework that was applied to the original Nissl stack, by using the corrected Nissl stack as an exact shape prior with only rigid in-plane cross-registration connecting the two series and using the cross-modality similarity metrics of Section 2.3. Fig 2.13 shows examples of fluorescent image stacks being reconstructed by transferring the segmentation computed on the Nissl stack. The top two rows of Fig 2.13 show the computed transforms applied to the full resolution fluorescence image stack. Major connections and fiber tracts originating from the fluorescent tracer injections (Red: TRE3-tdTomato anterograde; Green: TRE3-Clover anterograde; Blue: Fast Blue retrograde) can be identified from the color-coded stains in 3D. The bottom row of Fig 2.13 shows 3D reconstructions of the tracings.

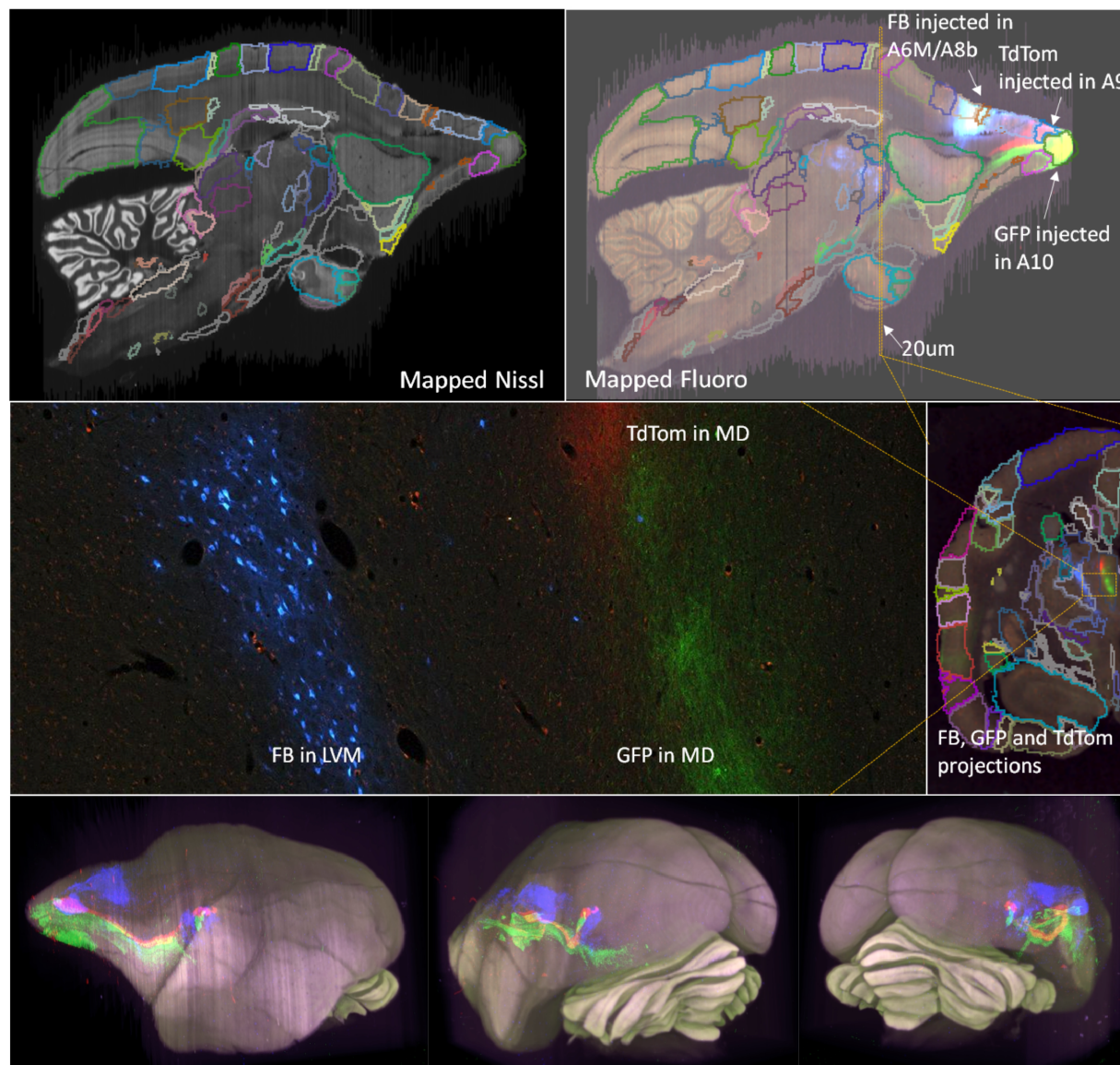


Figure 2.13: **Sample Nissl-stained and fluorescent data displayed with segmented and reconstructed tracer detections.** Top two rows: Nissl and fluorescent reconstructed segmented volumes. NB: the sections are originally cut in the coronal section; a sagittal virtual cut of the 3D reconstructed brain is shown. The upsampled reconstruction transforms are applied to the full resolution fluorescent tracer images where tract tracing can be performed. Here, the three injected tracers are labeled in the high resolution image (mid left). Bottom row: 3D visualization of the Nissl stack reconstruction overlaid with the red, green, and blue tagged tracer paths detected from the registered fluorescence volumes.

2.2.5 Effect of Model Priors on Curvature Preservation

The constraint of anatomical smoothness within a brain volume is critical to producing accurate reconstructions, particularly in cases with *missing data or tissue damage* (for instance, the cross-modality registration presented here in the case where the Nissl stack is damaged or has missing sections). As previously introduced in our reconstruction and registration model, we incorporate a smoothness prior in the form of a Sobolev derivative norm to provide robustness and control the dimension during the diffeomorphic mapping and restacking solution, as well as a shape prior in the form of an atlas/reference similarity function. The Sobolev prior couples adjacent sections and results in continuity of the reconstruction. It is particularly noticeable in the registration of multiple subject modalities to one another where sections are missing or damaged. The importance of this prior is visible in panels A-C of Fig 2.14.

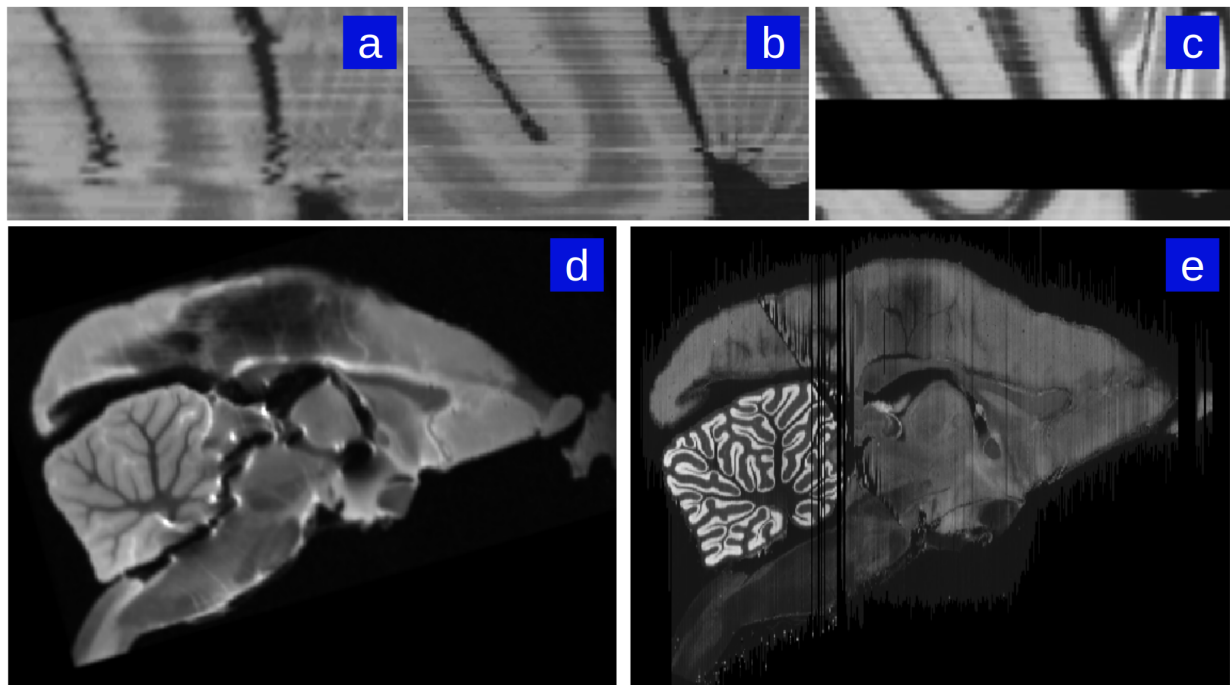


Figure 2.14: **Reconstruction examples depicting the effect of the smoothness prior.** When the Nissl stack (c) has missing or noisy sections, reconstruction to the next-best Nissl section contains small distortion accumulations (a). Inclusion of a smoothness constraint corrects this error (b). Additionally, highly damaged Nissl stacks can still be reconstructed despite major differences between damaged Nissl sections to corresponding MRI sections. For instance, ex-vivo MRI of a particular subject marmoset brain prior to sectioning (d) and successful Nissl reconstruction of the same marmoset brain despite major damage caused by sectioning process (e).

The effect of the image intensity smoothness prior also manifests during Nissl-to-MRI stack reconstruction when there is significant damage to the Nissl brain. An example of our framework’s ability to achieve accurate reconstruction when there is significant tissue damage (such as cutting and folding in particular sections) to the sections is shown in panels D and E of Fig 2.14.

Our pipeline also allows for the correction of curvature artifacts associated with the histo-

logical restacking unguided by same-subject MRIs. Fig 2.15 shows examples of the curvature artifacts associated with 2D-3D reconstructions unguided by a reference brain [133]. These figures demonstrate that the MRI guided registration pipeline solves the curvature issue. An example of this problem is shown in Fig 2.15. The left 2 columns show the unguided stacking alignment which results in a large curvature artifact (highlighted within the yellow bounding box). The third and fourth columns show the guided restacking using our current pipeline. The yellow bounding boxes depict the areas with highest curvature bias effects. The curvature of the coordinate grid depicted in Figure 2.15 is encoded by the 2D component of the 3×3 Jacobian matrix of the transformation. Notice the curvature of the grid is more extreme for the unguided reconstruction which has no MRI to guide it globally. The Malandain curvature artifact is present in the warping of the grids in the uncorrected restacking case due to the higher metric cost of φ required to map an atlas onto the accumulated distortions of an unguided reconstruction.

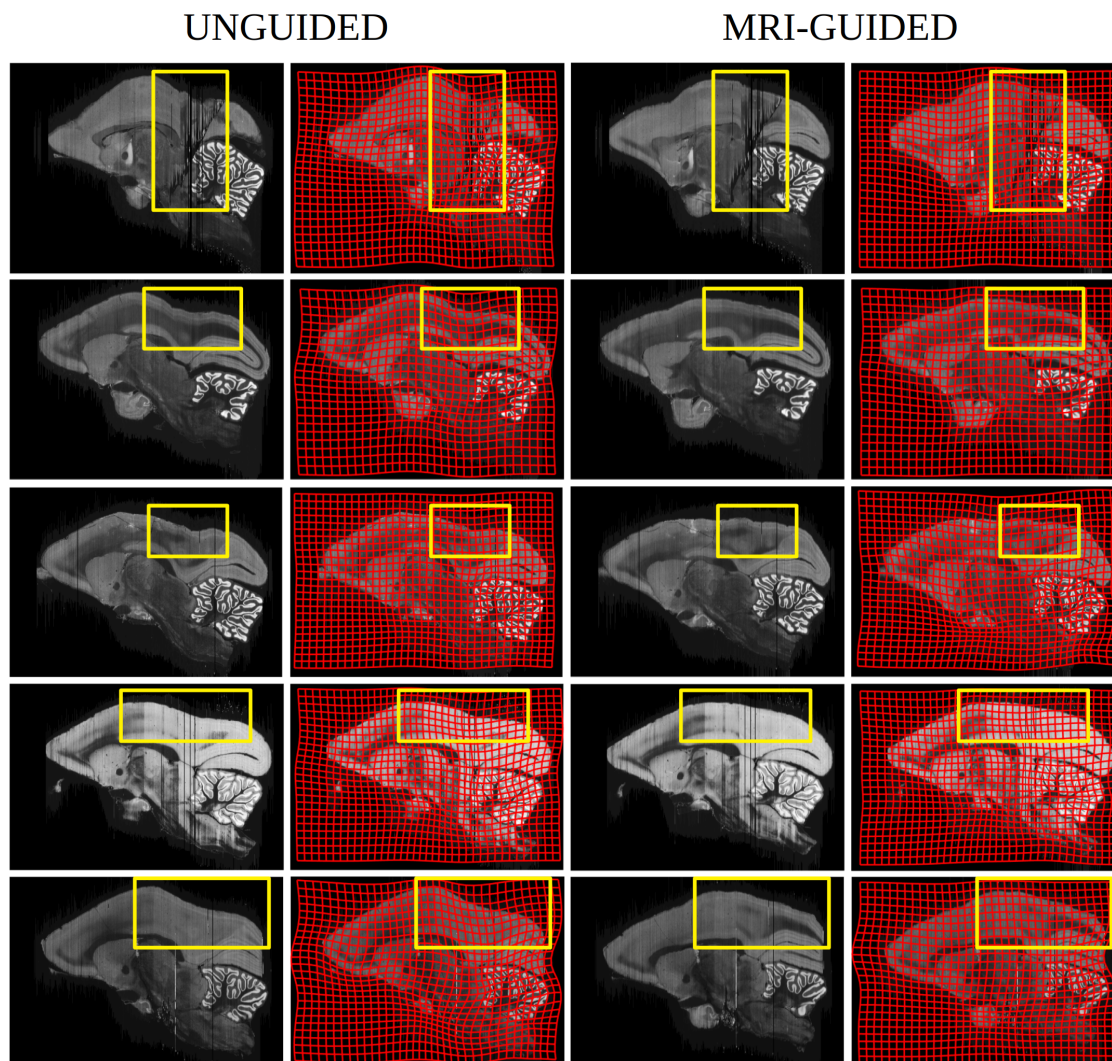


Figure 2.15: **Histology restacking examples from Brain/MINDS dataset.** Columns 1 and 2 depict sections exhibiting Malandain curvature artifact (notice cortical bend) associated to the unguided alignment with column 2 showing deformation of the underlying coordinate associated to the atlas-to-target warping; columns 3 and 4 show the Nissl histological stackings which are guided via the template based deformation. Regions of large artifact compared to none are highlighted via yellow boxes.

2.2.6 Quantification of Metric Distortions in Brain/MINDs Data

The diffeomorphic models described here uniquely place this work in a position to quantitatively study the metric distortions caused by the histology processing. We examine the first fundamental form, or determinant of the metric tensor, of the diffeomorphic mapping as described in Eqn (2.28). We do this to quantify the distortion caused by the histological process. Several preparatory processes occur in between the in-vivo MRI acquisition and the ex-vivo MRI acquisition – we interpret the Jacobian determinant of the mapping between these coordinate spaces as the combined deformative effect of tracer injection, extraction, perfusion, and tissue fixation. We report the “percent scale change factor” which is computed as $|\det \partial_X \varphi|^{\frac{1}{3}}$, the cube root of the Jacobian determinant, and which represents the per-axis local scale change. Similarly, the freezing and sectioning processes occur between the ex-vivo MRI acquisition and the histological imaging. Under our informed histological reconstruction model we can interpret the scale change between these two coordinate spaces as the combined deformative effect of freezing/sectioning.

We illustrate the quantitative properties of the Jacobian matrix as a first-order description of the map. Four sample measurements (two of the sectioning process, A and B, and two of the preparatory process, C and D) from the dataset are shown in Fig 2.16. These demonstrate that there is minimal metric scale change away from the identity map for the ex-vivo MRI to sectioned histology maps. However, the measured metric scale was much higher for the in-vivo pre-preparatory MRI to ex-vivo post-preparatory MRI maps. Panels A and B show the

percentage metric change away from the identity of the cube-root of the Jacobian between ex-vivo MRI and the Nissl reconstructed brains. Shown as a heat-map superimposed over the gray level images is the cubed root of the Jacobian determinant for the central sagittal

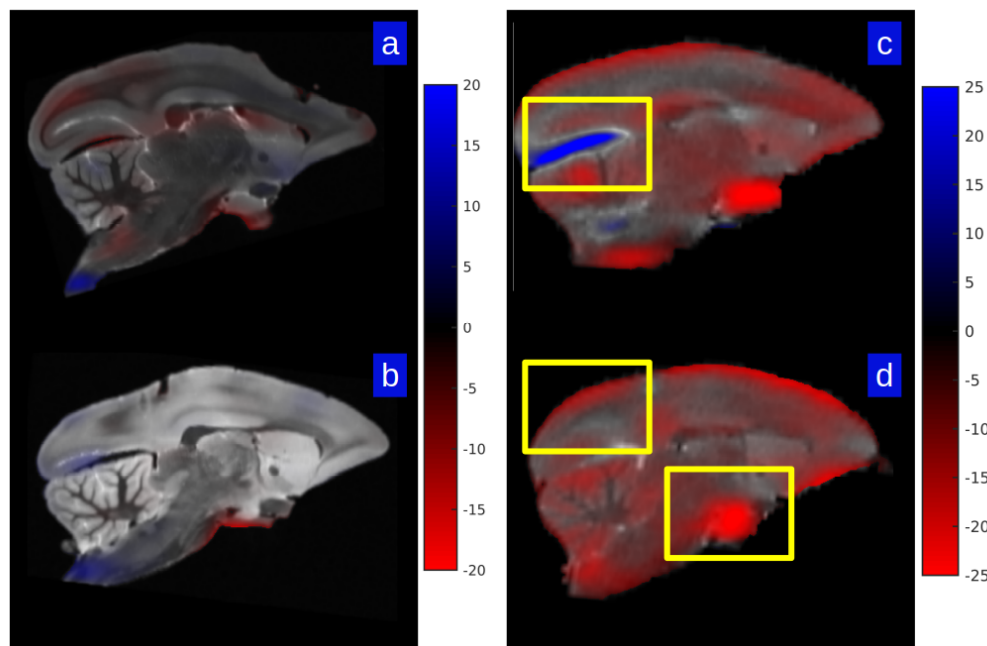


Figure 2.16: **Local scale factor change in two ex-vivo to histology mappings and two in-vivo to ex-vivo mappings.** Shown is the percent scale change away from the identity of the mapping as measured by the cube-root of Jacobian determinant; blue depicts shrinkage, red expansion. Panels A and B show two examples of ex-vivo MRI mapped to Nissl histological stack; panels C and D show the same for the ex-vivo to in-vivo MRI. Yellow boxes depict intense scale changes which are depicted via grid deformation shown in Fig 2.18.

As depicted by the color bar, the maximum value of blue represents 20 percent expansion

in a dimension, with the red implying contraction. Panels C and D show similar analyses for two brains corresponding to ex-vivo to in-vivo MRI maps, indicating several areas of significant contraction and expansion. Overall, we report the mean across 15 subjects of the median absolute percent scale change as 1.97 ± 0.38 % for the sectioning process (ex-vivo MRI to reconstructed histology mapping) and 6.90 ± 2.08 % for the fixation process (ex-vivo MRI to in-vivo MRI mapping).

Shown in Fig 2.17 are histograms of the percent scale change factor between the ex-vivo to Nissl histological stack (A & B) and the ex-vivo to in-vivo spaces (C & D) for the same brains shown in Fig 2.16.

As seen in Fig 2.16 and Fig 2.17, the change in measures between the ex-vivo post-preparatory and in-vivo MR-measured coordinate systems are large and mostly contractive in each dimension as measured by the cubed-root of Jacobian determinant. In comparison, the corresponding metric change due to the sectioning process are small, and are almost symmetric around zero (so that both shrinkage and expansion occurs in roughly equal proportions). The histograms of Fig 2.17 demonstrate that the range of the ex-vivo post-preparatory to in-vivo MR maps are nearly three times in terms of median absolute scale change. Fig 2.18 shows that scale change can be as much as 20-25 percent in a single axis dimension as measured by the cubed-root of Jacobian determinant. Shown are sample in-plane deformations for magnified brain regions from Fig 2.16. Notice that the intense blue indicates 25 percent expansion, and intense red indicates 25 percent contraction along a single axis dimension.

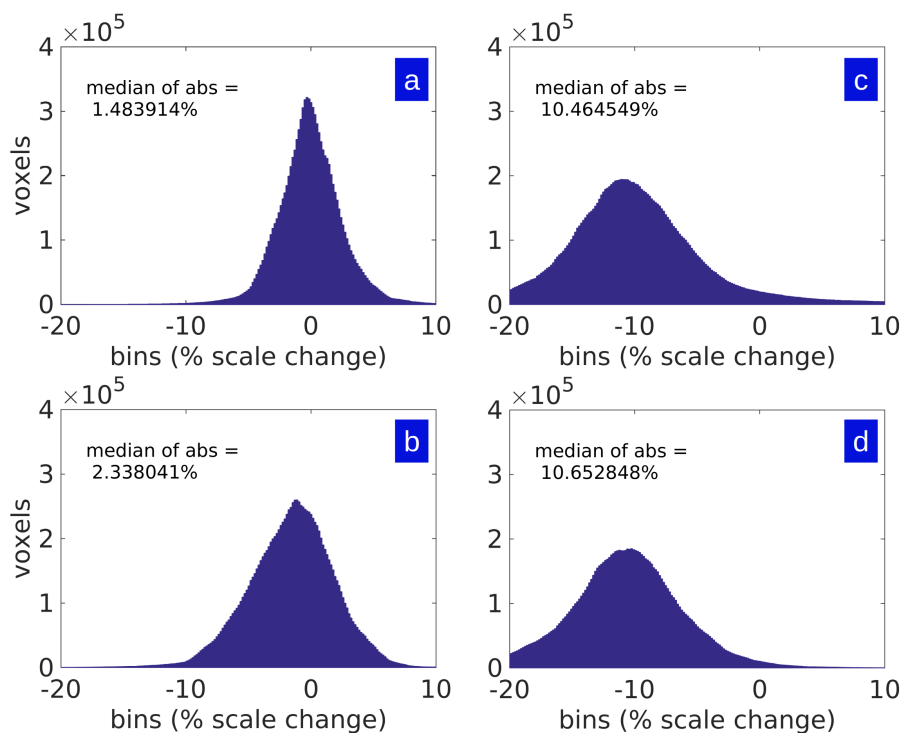


Figure 2.17: **Histograms of local percent scale factor change in two ex-vivo to histology mappings and two in-vivo to ex-vivo mappings.** Shown are histograms of the percent scale in single axis dimension as measured by cube-root of Jacobian determinant of maps shown in Fig 2.16. Panels A and B show the ex-vivo MRI mapped to Nissl histological stack; Panels C and D show the ex-vivo MRI to in-vivo MRI histograms.

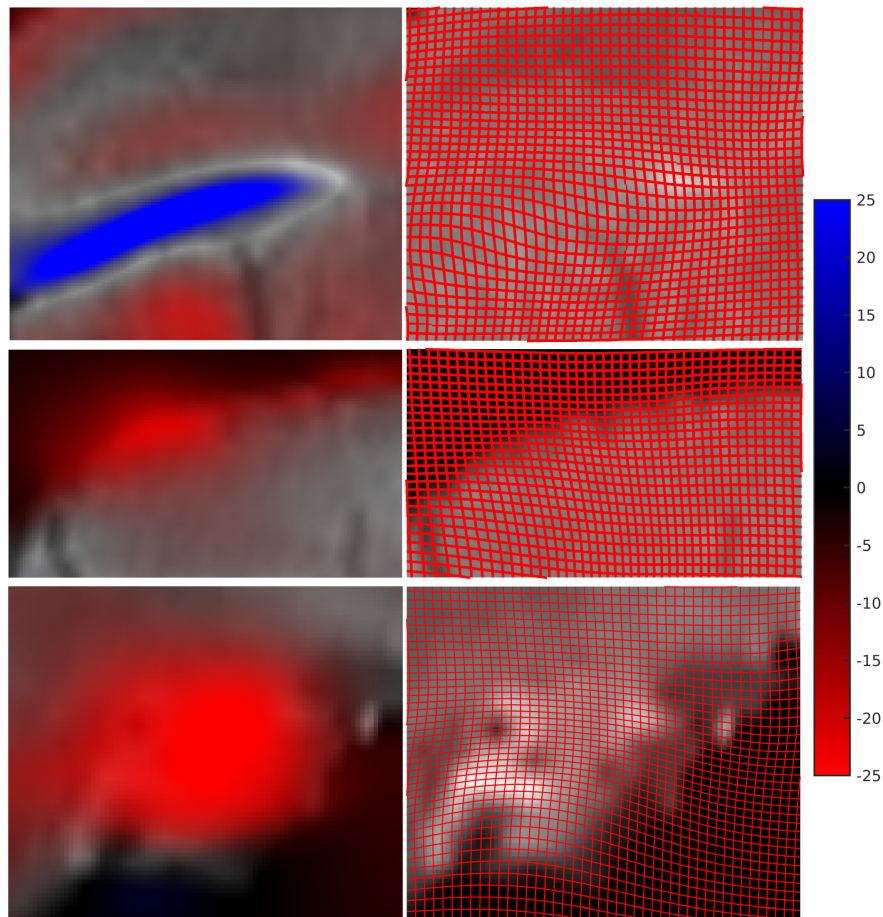


Figure 2.18: **Metric scale change associated with subvolume sections between in-vivo and ex-vivo MRIs.** Maximum blue indicates 25 percent expansion, maximum red indicates 25 percent contraction as measured by the cubed-root of Jacobian determinant. Right column shows the how a uniform square grid on the in-vivo brain deforms when mapping to the ex-vivo brain. This helps visualize the scale factor change from identity. Both grid expansion (top row blue) and grid contraction (bottom row red) is seen.

A closer examination of the brain-wide distribution of changes in tissue volume due to the preparatory process between the in-vivo and the ex-vivo MR images is shown in Fig 2.19. The heat map of the percent scale change factor of one mapping from in-vivo to ex-vivo MRI

is shown in sagittal and transverse sections of the same brain, with maximal red depicting 8 percent shrinkage along a single scale dimension. Delineation of cortical and subcortical structures (lines in Fig 2.19) from the atlas mapping shows that the distortions are not uniformly distributed across the cortex.

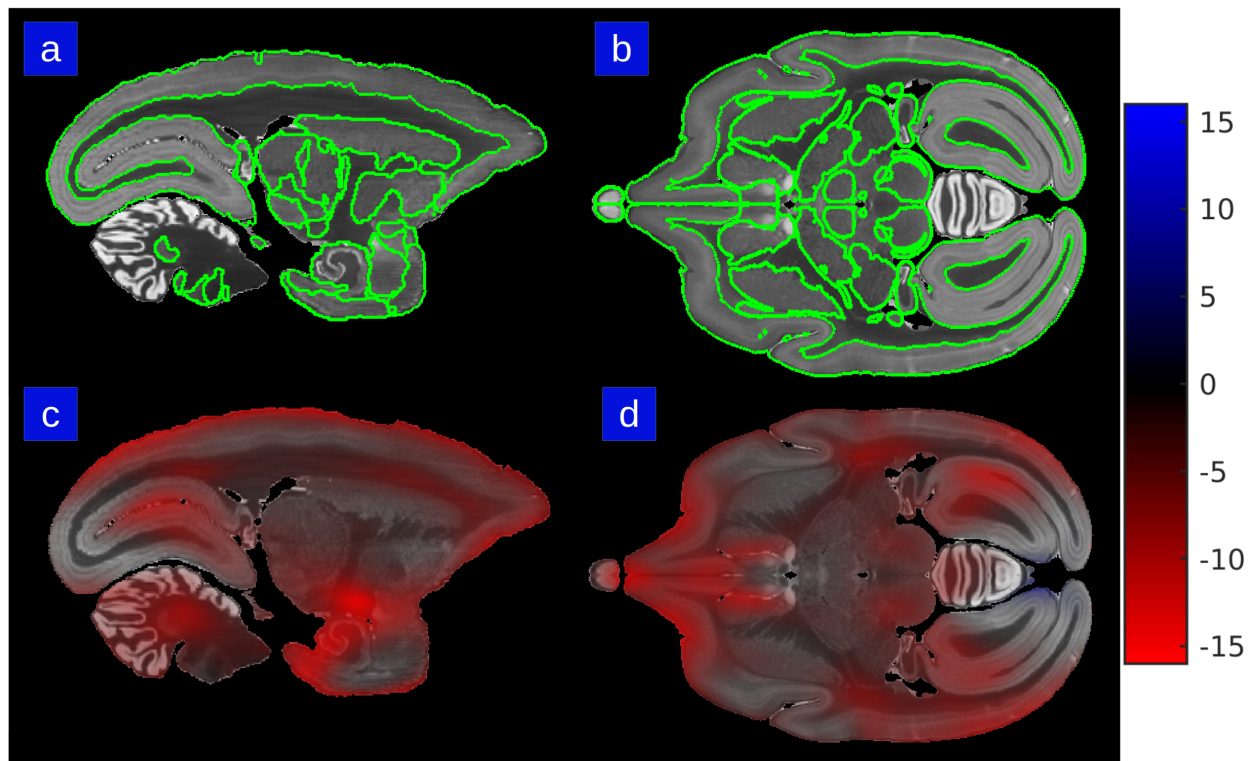


Figure 2.19: **Metric scale change of in-vivo to ex-vivo mapping in atlas coordinates.** Percent scale factor heat map is superimposed on olfactory bulb, cortical areas, septum, thalamus, epithalamus, pretectum, brainstem, hypothalamus, cerebellum, cranial nerve, entorhinal cortex. Panels A & B show section outlines of structures in the Paxinos/Hasikawa atlas in sagittal and transverse views. Panels C & D show the metric scale change for the same sections. The color bar depicts maximum red of percent scale contraction in a single axis dimension.

Thus, in future work quantifying cell or process densities, it would be important to

take into account these local scale changes, rather than relying on an overall scale factor which may or may not reflect what is going on at a specific location in the brain. Note the importance of acquiring an in-vivo and an ex-vivo MRI scan, without which this analysis is not possible.

The ex-vivo to histology coordinate mapping captures the deformative effects of the “sectioning” process. This mapping enables not only the histological reconstruction but also the segmentation of brain regions which allows the quantitative measurements of scale factor change. In an analysis of the dataset of 15 brains, the cerebral cortical areas, thalamus, brainstem and the cranial nerves showed a local scale change of $< 1\%$ per axis as measured by the percent scale change factor. The hippocampus, basal ganglia, pretectum and cerebellum showed a local change of 2-3% and the hypothalamus showed a local change of 4% per axis. The in-vivo to ex-vivo coordinate mapping encompassing the extraction, perfusion, and fixation procedures shows much higher levels of distortions when averaged across the dataset. The cerebral cortical areas, thalamus, brain stem and the cranial nerves show a significantly larger absolute scale change of 5-6% per axis. For the hippocampus, basal ganglia, pretectum, cerebellum, the difference was 6-8% for the in-vivo to ex-vivo maps. The hypothalamus showed a large change of 10% per axis.

2.2.7 Volume Reconstruction in Mouse Cardiac MRI

As a final example, we apply our proposed shape interpolation algorithm (Section 2.1.9) to upsample a sparsely acquired cardiac MRI dataset. As a part of ongoing project and work we have previously published [117] (©2019 IEEE, selections reprinted with permission from Lee BC et al., Diffeomorphic Upsampling of Serially Acquired Sparse 2D Cross-Sections in Cardiac MRI, Proceedings of the 2019 IEEE EMBC, 2019), in-vivo heart images of 5 adult male wild type ($n = 2$) and Galectin-3 knockout ($n = 3$) mice were acquired using Bruker NMR/MRI spectrometer equipped with a 11.7T magnet and a gradient set capable of developing gradient strengths of 740mT/m (Bruker Biospin, Germany). The mice were positioned on the MRI 4-channel surface coil and an MRI gating trigger was established via ECG leads and a respirator pillow was used. Cine MRI was collected (15 frames, echo time (TE) = 1.9708 ms, repetition time (TR) = varied according to the heart rate, slice thickness of 0.8 mm, in plane resolution of $0.1307 \times 0.1307 \text{ mm}^2$, flip angle = 12, NEX = 6) at 6-8 short axis slices through the LV. Figure 2.20 shows some examples of the dataset.

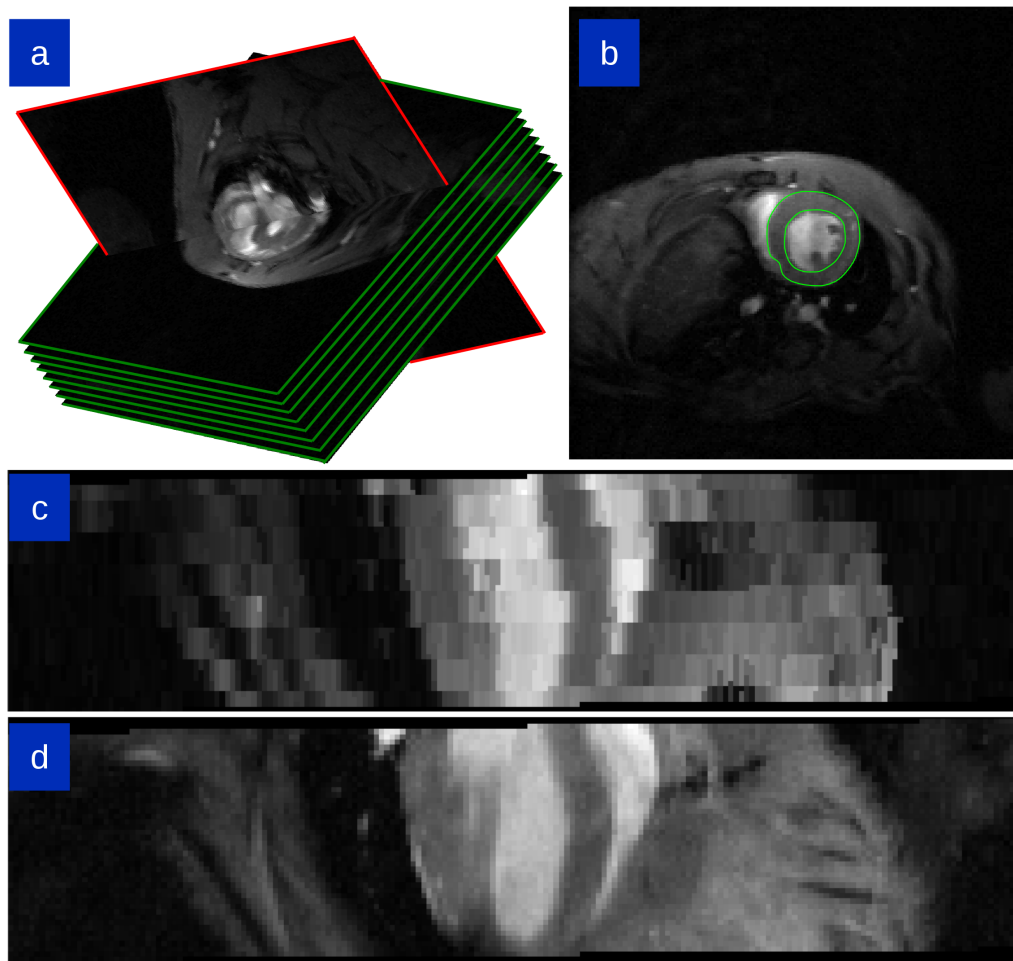


Figure 2.20: Sample images from the mouse cardiac MR dataset. a) A long axis section interposed with short axis sections. b) Short-axis cine with manual segmentation. c) Short-axis image stack resliced along the long axis at native resolution. d) True long-axis cine image.

As a first step, we apply the proposed algorithm of Section 2.1.9 to the $0.1307 \text{ mm} \times 0.1307 \text{ mm} \times 0.8 \text{ mm}$ short-axis image stack of Figure 2.20 in order to upsample the volume by a factor of six along the imaging axis to $0.1307 \text{ mm} \times 0.1307 \text{ mm} \times 0.1333 \text{ mm}$. The resulting upsampled volume is resliced along the given acquisition's long-axis image plane

and compared against the ground truth acquisition alongside other interpolation methods in Figure 2.21. Because corresponding long-axis acquisitions were not available for all subjects, we present comparison of long-axis reslicing for visual comparison only. Nearest-neighbor interpolation produces the expected step artifacts, and while linear interpolation somewhat smooths these artifacts, they are still evident in panel b of Figure 2.21. Unlike linear interpolation, the proposed model is capable of modeling physical fluid-like deformations, producing the profile most similar to the ground truth.

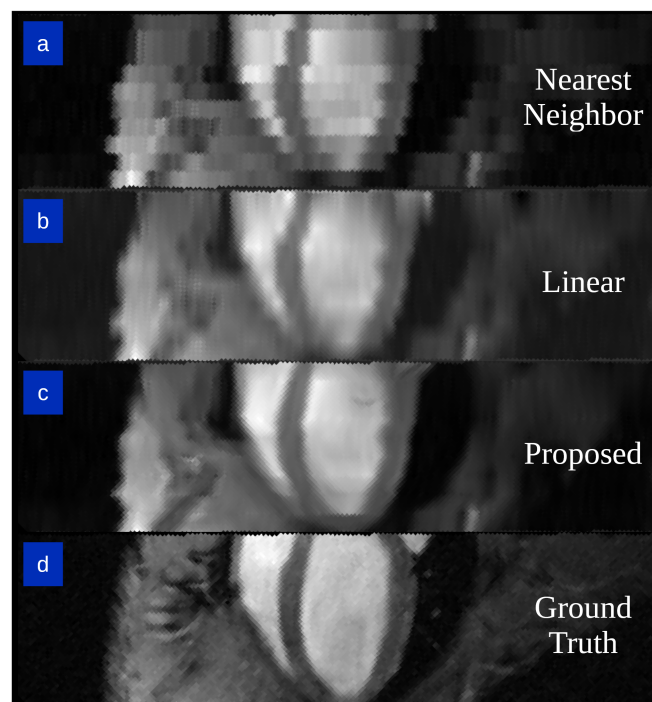


Figure 2.21: Long axis view through left ventricle, resampled from several interpolation methods applied to short-axis image stack alongside ground truth long axis image. a) Nearest neighbor interpolation applied to short-axis stack. b) Linear interpolation applied to short-axis stack. c) Our proposed shape-based interpolation applied to short-axis stack. d) Ground truth long axis scan.

To quantitatively evaluate the proposed shape interpolation method, we perform a short-axis estimation experiment and evaluation. We apply the proposed algorithm to our mouse cardiac MR dataset and evaluate the accuracy of our estimations by excluding an interior short-axis slice and comparing our estimate with the excluded ground truth. For example, in a heart with 10 slice acquisitions along the left ventricle, we estimated slice 2 using only slice 1 and 3, then we estimated slice 3 using only slice 2 and 4, and so on. In total, the dataset contains 68 such unique triplets of neighboring slices. We evaluate the mean squared error of the grayscale image produced by our estimated with the ground truth image and we compare against traditional linear interpolation. An independent expert has also hand-segmented all estimated slices from end-systole and end-diastole time points for both the proposed method and linear interpolation, and we report the resulting segmentation Dice [134, 135] score against the ground truth.

We perform this evaluation for the end-systole and end-diastole time points for all subjects. A sample series of three acquired short-axis end-systole sections from a single subject are shown in Figure 2.22. For every triplet of sections, the central section is hidden from the proposed model and reconstructed using its neighbors. Figure 2.23 shows an example of this process in which section 7 from Figure 2.22 is estimated by both linear interpolation and the proposed diffeomorphic interpolation method.

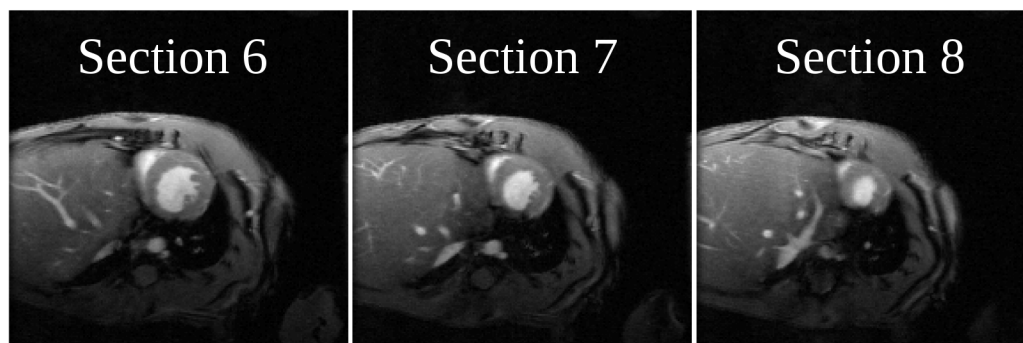


Figure 2.22: Sample of three consecutive 0.8 mm thickness short-axis sections acquired at end-systole from a single subject. Sections move closer to the apex as section # increases.

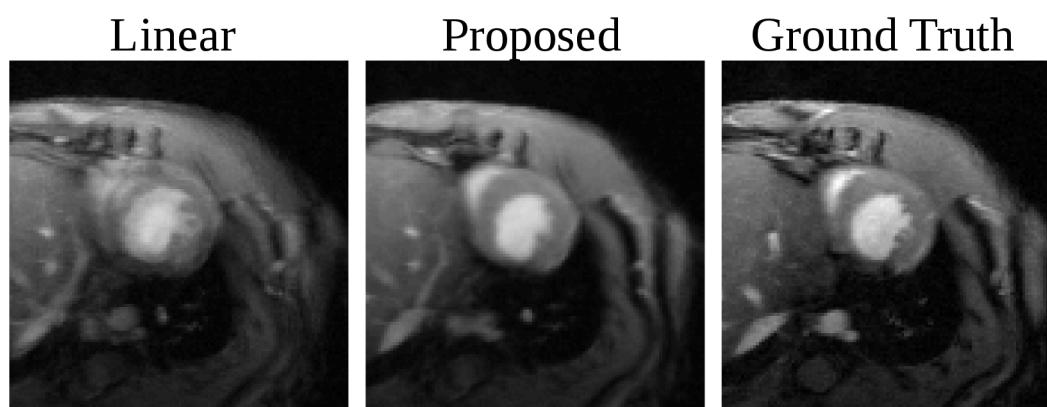


Figure 2.23: Estimation of an intermediate section (section 7 from Figure 2.22) by linear interpolation (left) and the proposed model (center). The ground truth is shown on the right. The images are zoomed to the left ventricle for clarity.

Here, the power of the proposed interpolation model becomes evident: obvious ghosting artifacts are present in the linearly interpolated image while the proposed model produces a coherent image with left ventricular boundaries that closely match the ground truth image. Beyond the heart itself, the proposed model clearly produces more accurate estimations in

regions with thin features, such as the ventral chest surface on the right side of the panels of Figure 2.23.

We first quantify the accuracy of our estimation by comparing the absolute intensity difference between our estimated images and the ground truth. Figure 2.24 shows the difference image for the estimation of section 7 from Figure 2.23 for both linear interpolation and the proposed model. The difference image shows a close estimate of the ground truth image intensity by the proposed method. Averaged over the entire dataset, we report a mean percent reduction in absolute intensity error of $12.7\% \pm 3.26\%$. We also report that 100% of slices estimated by the proposed model showed lower absolute intensity error compared to linear interpolation. We performed a one-sided Wilcoxon rank-sum test between the sets of individual error values for slice between the two methods and report a p-value of 1.31×10^{-8} , indicating that our method produces significantly more accurate intensity estimates.

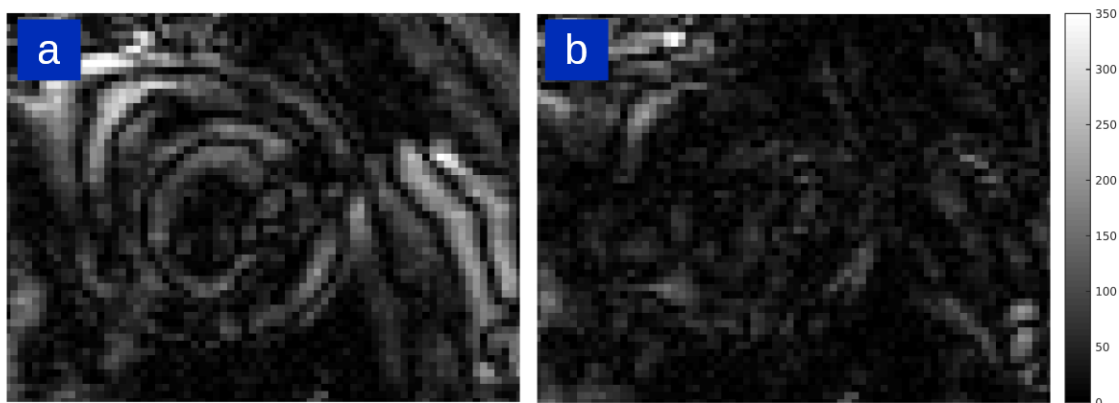


Figure 2.24: Sample absolute intensity difference image zoomed to the left ventricle between a) ground truth slice and linearly interpolated estimation, and b) ground truth slice and diffeomorphically interpolated estimation. Colorbar has units of % mean intensity of the ground truth image.

In addition to comparing raw intensity, we evaluate our model by comparing manual segmentations of estimated slices by an independent expert against segmentations of the ground truth by the same expert. We evaluate the Dice coefficient of each dense 2D segmentation and observe marked improvement in estimation of the LV boundary when comparing our model (mean Dice score across slices of 0.87 ± 0.085) to linear interpolation (mean Dice score across slices of 0.79 ± 0.11). We again performed a Wilcoxon rank-sum test between the two groups of Dice scores and report a p-value of 1.53×10^{-4} , indicating significantly improved accuracy in the left ventricular region using the proposed method. Sample segmentations for each model overlaid with the ground truth segmentations are shown in Figure 2.25. The right column of this figure shows close alignment between the ground truth (green) and proposed model (red), whereas linear interpolation (blue) is generally less accurate.

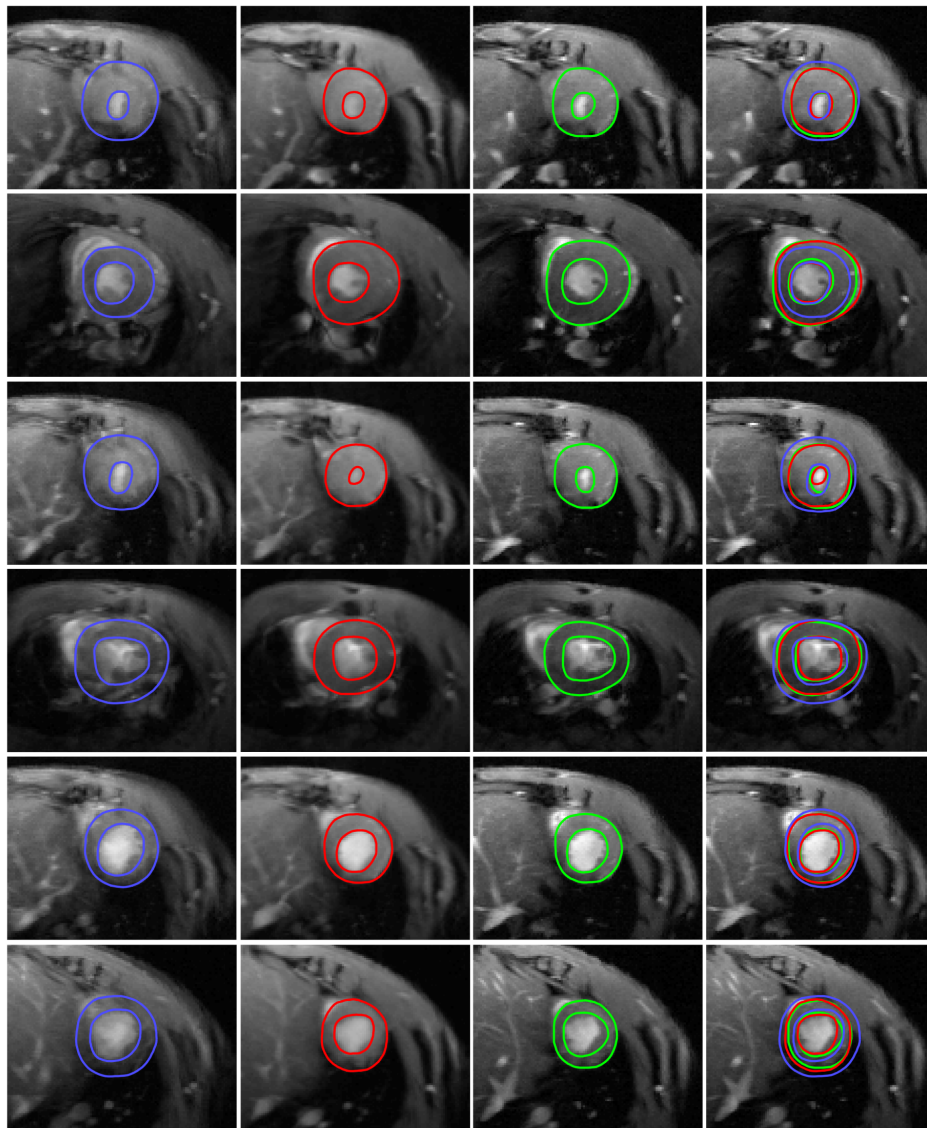


Figure 2.25: Sample manual segmentations of linearly interpolated estimations (left, blue), diffeomorphically interpolated estimations (left center, red), ground truth (right center, green), and all three overlaid on the ground truth (right).

Alongside improved upsampling accuracy, an additional benefit of the proposed deformation-based model is its ability to carry information associated to the sparse observations into the

upsampled region. For instance, we can apply each section's computed Jacobian-weighted averaging to the associated sparse segmentations to produce a densely segmented and upsampled volume; this is not possible by linear or nearest-neighbor interpolation. Figure 2.26 shows an example of this effect on a long-axis reslicing of an upsampled short-axis stack.

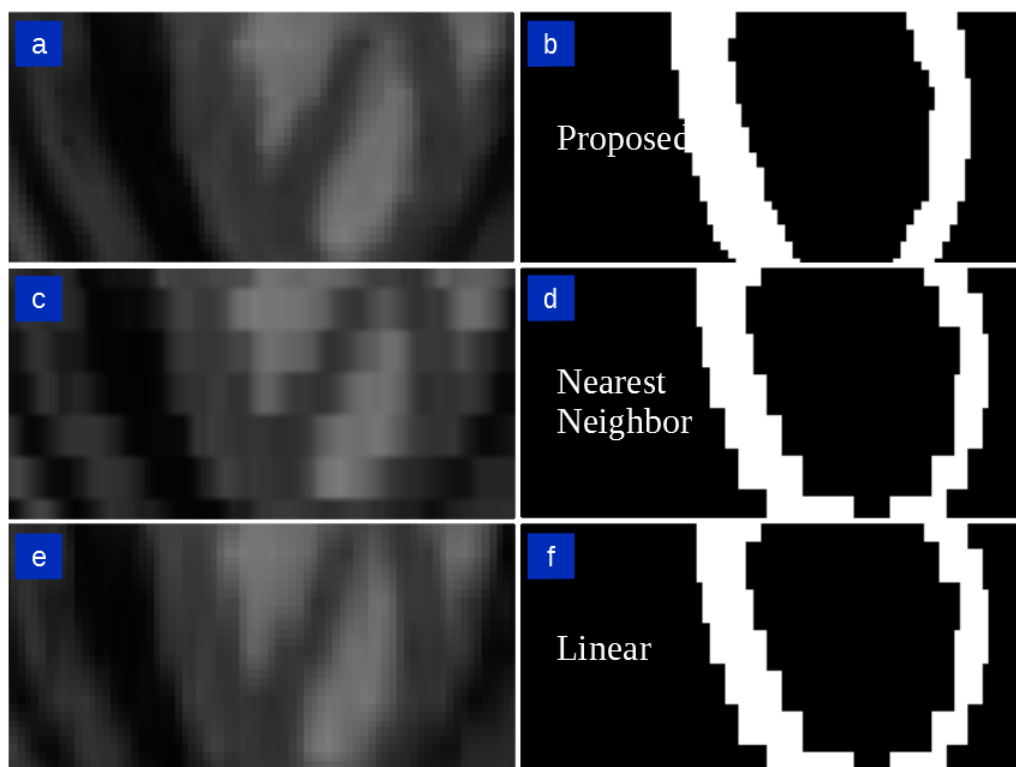


Figure 2.26: Comparison of sparse segmentations upsampled by a&b) the proposed model, c&d) nearest neighbor interpolation, e&f) linear interpolation, alongside upsampled grayscale intensity images. Segmentation by linear and nearest neighbor methods are identical in the case of 50% thresholding.

In addition to upsampling of cardiac MRI, we show that this method is also relevant for brain histology data which has a similarly high degree of anisotropy in image resolution. In Figure 2.27, an example of an upsampled brain histology volume from a sectioned human

brain chunk is shown. A comparison is made between linear interpolation and the proposed method.

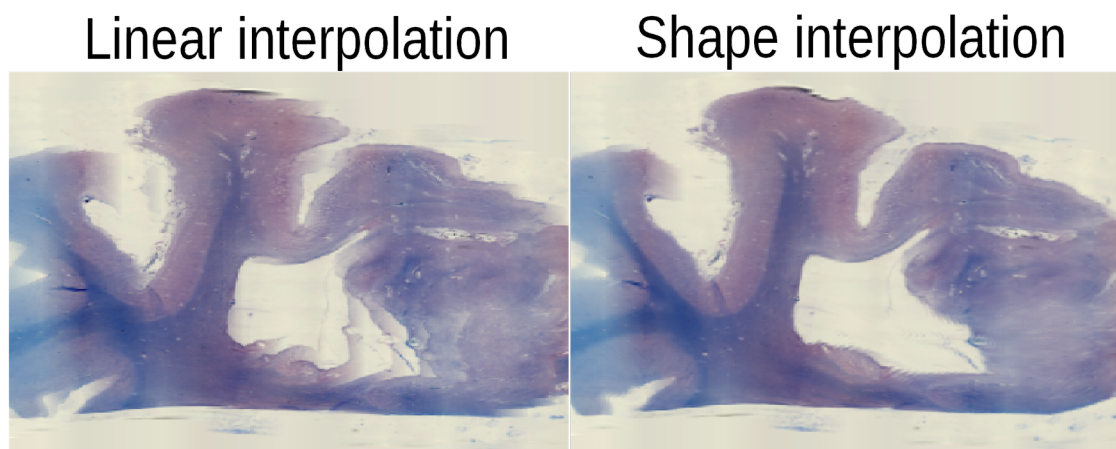


Figure 2.27: Interpolation of sections from human brain histology chunk. A stack of sections from human brain histology is reconstructed and upsampled using linear interpolation and the proposed method, before being sliced at an angle oblique to the sectioning plane. The resampled oblique plane is shown for linear (left) and shape (right) interpolation.

2.3 Discussion

Here, we have examined the computational anatomy random orbit model at the mesoscale for the stacking of sectioned whole brains coupled with mapping to annotated atlases. The standard CA model has been expanded to include the $O(3 \times n)$ extra rigid motion dimensions representing the planar histology sections. The estimation procedure solved here simultaneously estimates the diffeomorphic change of coordinates between atlas and target histological stack, as well as the “nuisance” rigid motion parameters for each section in stack space. This requires the introduction of a smoothness constraint on the target jitter simultaneous with

LDDMM, which is enforced via a Sobolev metric, encouraging the reconstructed stack to be smooth by controlling the derivative along the cutting axis.

Dense large deformation diffeomorphic image matching is being used extensively for magnetic resonance imaging in the brain at 1 millimeter scale for both T1 and DTI [1, 39, 114, 136] as well as for human anatomy [53] including for transferring the geometries of Cardiac fibers in dense Cardiac imaging [9, 45] and for radiation treatment planning [43]. These technologies form the basis of many implementations such as Ashburner’s important SPM [14, 137]. The aforementioned applications have not included complex prior distributions to encode distortions such as the Sobolev derivative prior introduced here that may have been required due to the distortions introduced in the imaging and stacking process.

Our results generally demonstrate that the introduction of an atlas into the estimation scheme and simultaneous accommodation for the nonlinear atlas-to-target shape difference via diffeomorphism solves several of the classic problems associated with volume reconstruction, including the recovery of the curvature of extended structures. Since the atlas gives *a priori* indication of the global shape, the tendency to remove distortions along the section axis is balanced against the desire to minimize the amount of deformation of the atlas onto the reconstruction. The algorithm is shown to mediate this tension well.

When the shape prior is a same subject reference volume, the guided reconstruction acts as an improved initialization for nonlinear image registration, placing the voxels of the subject volume closer to their corresponding voxels in the atlas volume. As with any

gradient-based optimization framework, LDDMM benefits from improved initialization as this reduces the likelihood of falling into a local minimum in the objective function. As shown in Fig 2.15 the sample maps generated by registration of the Brain/MINDS atlas to an unguided reconstruction versus a guided reconstruction reveals an increased curvature of the underlying coordinate grid warp associated with the atlas mapping in the unguided case, indicating a displacement field with higher magnitudes and less homogeneity.

The addition of the smoothness prior via the Sobolev norm is valuable for providing robustness in the presence of noise or missing data or when the shape prior is not an exact reference volume. The driving intuition behind the smoothness prior is that in addition to the subject brain taking the shape of the reference volume, its image should be continuous and smooth. The effect of this prior is particularly noticeable in the registration of multiple subject modalities to one another where sections are missing or damaged. This is visible in the top row of Fig 2.14.

Our quantitative study of the histology-induced distortions (Fig 2.16) reveal that the general deformation effect caused by the histological process is shrinkage in certain areas of the brain, and also expansion in other regions. The shrinkage is not surprising as it is generally well-known that some tissue shrinkage is caused by the histology procedures [72]. Examination of the mean image (Fig 2.19) shows that shrinkage is not uniform throughout the brain but is generally located in the central and inferior regions of the brain, and near the ventricles. However, we note that some areas of the brain also showed expansions as depicted

in the almost symmetric histogram of scale changes. More importantly, the methodology provides a *quantitative* measure for every brain voxel of the associated scale factor.

Our 3D volume reassembled maps from the tape transfer assisted histological sections matched very closely with the ex-vivo MRI maps. When the reassembled volumes from sections using the tape transfer technique [130] were compared with the ex-vivo post perfusion MRI, the efficiency of the technique in preserving the tissue becomes evident.

In contrast, quantification of the impact of the preparatory processes which was achieved by mapping the in-vivo MRIs to the ex-vivo MRIs, confirms the large, uni-directional shrinkage of brain tissue that has been reported in the literature. We believe that this is the first time that there has been a detailed quantification of these changes brain-wide. We show that this shrinkage is not uniform across the brain and different brain areas show quite different levels of change.

Finally, the embedding of our proposed algorithms into the computational anatomy random orbit model enables the application of many existing algorithms based on the random orbit model to our serially-sectioned datasets. We demonstrate one example by performing shape interpolation, a derivative of template estimation, on serially-sectioned imagery in order to upsample them along the sectioning axis.

Chapter 3

Diffeomorphometry for Longitudinal Shape Analysis

Describing longitudinal morphometric differences between populations and individuals is a critical task in computational anatomy. Having described methods based on the random orbit model of computational anatomy for spatial image series in the previous chapter, we now turn to the study of models for longitudinal image data. In the context of the random orbit model, this often implies study of the variation of individual shape trajectories associated to some mean field, as well as longitudinal morphological differences as encoded by similar subjects from representative populations. In this chapter, we present a new method for computing the deviation of individual subjects from models of flow. We demonstrate estimation of the infinitesimal drift representing the mean flow of a population and its entrance

into the Eulerian vector field controlling that flow. Each individual is studied longitudinally by modeling another associated individual drift which acts as the personalized control of the flow. We provide an augmentation of the classic LDDMM equations to generate “biased geodesics” for trajectory shooting algorithms, allowing for direct computation of the individual’s deviation under the influence of a mean drift. Our new model is inspired by diffusion models from stochastic processes in which the personalized control is a non-stochastic term representing the additive Brownian component on top of the infinitesimal drift representing the population. We present results of our model on entorhinal cortical surfaces extracted from a patient population of the Alzheimer’s Disease Neuroimaging Initiative. Parts of the following text are selected from our publication on this subject [138] (©2020 IEEE, selections reprinted with permission from Lee BC, Tward DJ, Hu Z, Trouvé A, Miller MI. Infinitesimal Drift Diffeomorphometry Models for Population Shape Analysis. IEEE/CVF Conference on Computer Vision and Pattern Recognition, 5th International Workshop on Differential Geometry in Computer Vision and Machine Learning, July 2020.).

3.1 Methods

3.1.1 Brownian Motion and Hamiltonian Flows

The work proposed in this chapter is motivated by the goal of developing methods for encoding diffeomorphic modeling with typical population shape. We explicitly define the

population shape as represented by the mean vector field encoding the flow of the cohort, and we associate to each individual in the population a deviation encoding another personalized vector field. Viewing the diffeomorphism as the state in a dynamical system, then the typical flow encodes the overall average control; the individual is encoded by the deviation via an additional personalized control. These high dimensional trends directly encode typical growth, atrophy, and neurodevelopmental or neurodegenerative disease. We embed into our new algorithms the estimation of the vector field which is in common to the population as well as the per subject estimation of the individual deviation.

In describing the model, we use the language of the diffusion and stochastic differential equations studied in the classical stochastic process literature of Brownian motion with drift [139]. Of course, we appreciate that in our setting, the state is infinite dimensional. The infinitesimal drift in our model is the differential change in state given by the diffeomorphic flow; we associate the mean flow or "mean drift" representing the population to the infinitesimal mean of Brownian motion, and likewise associate the personalized infinitesimal motion or "personalized control" to the infinitesimal variance. For us the personalized deviation is not stochastic, but is another deterministic drift term replacing the explicit Brownian term. Holm [140] has examined diffeomorphic flows in the context of the stochastic term in this infinite dimensional setting.

Our focus on the infinitesimal mean to encode the population of typical shape as a method to study individual deviations is motivated by the success of representing population means

in the field of machine learning and data science. The conditional mean as an estimator is remarkably efficient and ubiquitous. Examples abound in the literature for representation of the expected value of moments via the use of maximum entropy models for speech and image representation [141–148]. The drift term in stochastic optimization and random sampling for inference in high dimensional spaces has seen a plethora of successful applications, where drift guides a process towards a particular set of explanations as represented by the posterior distribution [149–151]. As well, our representation is highly reminiscent of the principles embedded in mixed-effect modeling of what are usually lower dimensional statistics. Here, our goal is to build into the diffeomorphic flow model itself the typicality of shape as represented by the population mean as well as the variance of the individual by associating it to the individual deviation element.

We approach this problem from the Hamiltonian flow perspective. We generally describe diffeomorphisms by computing geodesics parameterized by initial momentum. This is a natural representation as geodesics are often described as the motion of a particle through a curved space when no force acts on it other than the initial impulse. However, in our case, we seek to model diffeomorphisms controlled by “biased geodesic” flows, in which the particle is influenced by some external force, here termed the “infinitesimal drift”. This interpretation makes clear the inspiration that we take from models of particle movement as controlled by Brownian motion with drift.

3.1.2 Drift Model for Longitudinal Shape Analysis

Our basic model for longitudinal shape is a mechano-dynamical system in which structures are viewed as being embedded in a condensed matter continuum where advection and transport hold [2, 14, 152]. In the following text, we will refer to the infinitesimal mean as the **mean drift** and the individual deviation as the **personalized control** for simplicity. The model of dynamics for a given subject i is a dense space-time flow of the state $t \rightarrow \varphi_t^{(i)}(x) \in \mathbb{R}^3, x \in \mathbb{R}^3$ with control $t \rightarrow v_t^{(i)}$ given as the superposition of drift $\mu_t^{(i)}(\cdot)$ representing typicality and personalized or individual mechano-dynamics $w_t^{(i)}(\cdot)$:

$$\frac{d\varphi_t^{(i)}}{dt}(x) = v_t^{(i)} \circ \varphi_t^{(i)}(x), \quad \varphi_0^{(i)}(x) = x \quad (3.1a)$$

$$\text{with } v_t^{(i)} = \mu_t^{(i)} + w_t^{(i)} \quad (3.1b)$$

where the mean drift μ_t in an exemplar coordinate system (see Figure 3.1) is transported into the coordinate system specific to subject i to produce $\mu_t^{(i)}$, and $w_t^{(i)}$ is the personalized control. The Eulerian vector fields $v_t^{(i)} \in \mathbb{R}^3$ are modeled as elements of a Hilbert space of smooth and 1-time differentiable functions of space. In the continuum, this smoothness corresponds to the motions seen for transport and advection as associated to growth and atrophy from millimeter to meso-scale. We model the dense vector fields $v \in V$ as being

generated via differentiable scale-space kernels $k(\cdot, \cdot)$ acting on L_2 functions:

$$V = \{v = \int k(x, y)h(y)dy, \|h\|_2^2 = \int |h|^2 dx < \infty\}. \quad (3.2)$$

A diagram of the proposed generative model is displayed in Figure 3.1. The model is similar to that proposed in [82] in which there is a normalization of each individual flow of the population relative to the template which essentially defines the initial condition of each individual flow, denoted as $\Phi^{(i)}, i = 1, \dots, N$. To define the mean flow of the normalized population within each individual's time series, we coadjointly transport [153] it and denote it as $\mu_t^{(i)}, i = 1, \dots, N$.

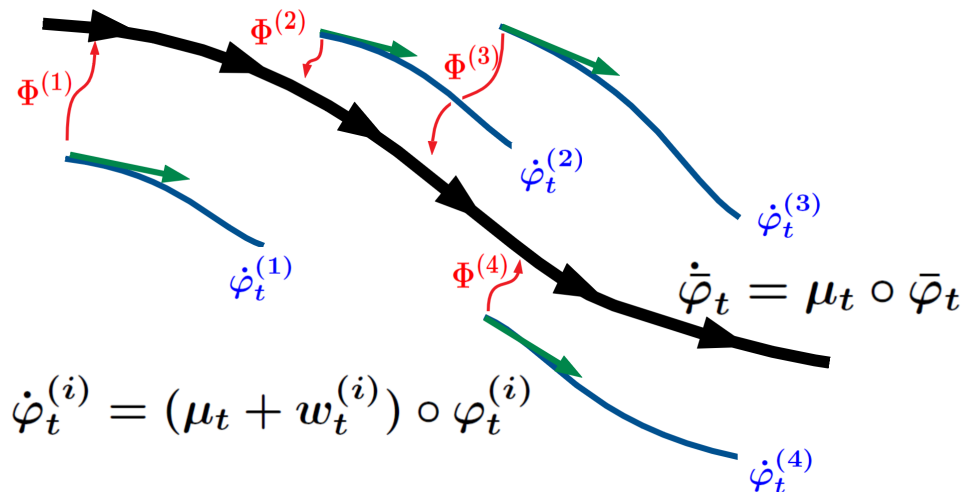


Figure 3.1: Diagram of infinitesimal mean drift model. The black curve represents the flow generated by the population mean drift μ_t , while individual subject observations' flows are governed by $\dot{\varphi}^{(i)}$. The red curve represents transport $\Phi^{(i)}$ of the personalized controls $w_t^{(i)}$ into the coordinate space of the mean drift.

3.1.3 Estimating Personalized Control under Drift

The dynamics space is huge. We select the parsimonious ones based on what we term "biased geodesic flow" via Hamilton's principle and the principle of least action. We term it biased because we add an infinitesimal mean drift to the standard geodesic equations of LDDMM, where the mean drift represents the population statistics. We adopt a Hamiltonian control systems model for flows of human anatomy [126]. Given the mean drift $\mu_t^{(i)}$ in an individual's coordinates, we define the Hamiltonian of our dynamical system according to

$$H(p, \varphi^{(i)}, w^{(i)}, t) = \int p \cdot ((\mu^{(i)} + w^{(i)}) \circ \varphi^{(i)}) dx - \frac{1}{2} \|w^{(i)}\|_V^2 \quad (3.3)$$

where $\dot{\varphi}^{(i)} = (\mu^{(i)} + w^{(i)}) \circ \varphi^{(i)}$ is a dynamical constraint, and p is termed the Hamiltonian momentum acting as a Lagrange multiplier on the constraint. Our dynamical systems model becomes the following:

$$\begin{aligned} \dot{\varphi}_t^{(i)} &= (\mu_t^{(i)} + w_t^{(i)}) \circ \varphi_t^{(i)} \\ \dot{p}_t^{(i)} &= -d(\mu_t^{(i)} + w_t^{(i)})^T \circ \varphi_t^{(i)} p_t^{(i)} \\ w_t^{(i)}(\cdot) &= \int K(\cdot, \varphi_t^{(i)}(x)) p_t^{(i)}(x) dx \end{aligned} \quad (3.4)$$

The initial momentum $p_0^{(i)}$ driving the time-varying velocity field $w_t^{(i)}$ can be computed under this constrained optimization scheme and represents the deviation or personalized control of

individual i from the background mean drift $\mu_t^{(i)}$. We model $p_0^{(i)}$ as being initially seeded on a set of k discrete control points $q^{(i)}$ such that $p_0^{(i)}(x) = \sum_k w_k^{(i)} \delta(x - q_k^{(i)})$. Notably, $\mu_t^{(i)}$ does not appear in the regularization term of (3.3) and thus this formulation does not produce the same $w_t^{(i)}$ as for the more classical LDDMM. Classic geodesic shooting initialized at μ_t does not produce this result for any non-zero regularization weight. The proposed model treats the drift as being in a space where it is identity, and deviations from the drift in any direction have the same metric distance.

3.1.4 Derivation of Dynamics Equations

The diffeomorphic flow is controlled by the governing differential equation (of typical LDDMM).

$$d\varphi_t = v_t \circ \varphi_t dt \quad (3.5)$$

We define our velocity field v_t as the sum of μ_t the drift and w_t the personalized control:

$$v_t = \mu_t + w_t \quad (3.6)$$

The diffeomorphic flow is governed by:

$$\dot{\varphi}_t = (\mu_t + w_t) \circ \varphi_t \quad (3.7)$$

We define the augmented Hamiltonian:

$$\tilde{H}(p_t, \varphi_t, w_t, t) = \int p_t \cdot ((\mu_t + w_t) \circ \varphi_t - \dot{\varphi}_t) dx - \frac{1}{2} \|w_t\|_V^2 \quad (3.8)$$

The first equation in the dynamical system which governs $\dot{\varphi}_t$ is given.

Solve for \dot{p}_t

We solve for \dot{p}_t by taking a perturbation of φ_t in the Hamiltonian by some amount ε :

$$\left. \frac{d}{d\varepsilon} \int p_t \cdot ((\mu_t + w_t) \circ (\varphi_t + \varepsilon \delta \varphi_t) - (\dot{\varphi}_t + \varepsilon \delta \dot{\varphi}_t)) dx \right|_{\varepsilon=0} = 0$$

$$\left. \frac{d}{d\varepsilon} \int p_t \cdot ((\mu_t + w_t) \circ (\varphi_t + \varepsilon \delta \varphi_t)) - p_t \cdot (\dot{\varphi}_t + \varepsilon \delta \dot{\varphi}_t) dx \right|_{\varepsilon=0} = 0$$

Apply the chain rule:

$$\int p_t \cdot d(\mu_t + w_t) \circ \varphi_t \cdot \delta \varphi_t - p_t \cdot \delta \dot{\varphi}_t dx = 0$$

Take the integral over simulation time and do integration by parts:

$$\int \int p_t \cdot d(\mu_t + w_t) \cdot \varphi_t \delta \varphi_t dx dt - \int p_t \delta \dot{\varphi}_t dz \Big|_{t=0}^{t=1} + \int \int \dot{p}_t \cdot \delta \varphi_t dx dt = 0$$

The boundary condition specified by the second term of the left hand side plays a role in the matching problem and it balances the forcing term coming from the longitudinal matching problem. We ignore this term for now.

$$\dot{p}_t = -d(\mu_t + w_t)^T \circ \varphi_t p_t$$

Solve for w_t

Take a perturbation of W_t in the Hamiltonian by some amount ε . Here we write the regularization term in matrix form where A is the inverse of some smoothing kernel K .

$$\begin{aligned} \frac{d}{d\varepsilon} \int \int (p_t \cdot (\mu_t + w_t + \varepsilon \delta w_t)(x) - \dot{\varphi}_t) \delta(x - \varphi_t) dx \\ - \frac{1}{2} \int (w_t + \varepsilon \delta w_t)^T(x) A (w_t + \varepsilon \delta w_t)(x) dx \Big|_{\varepsilon=0} = 0 \end{aligned} \quad (3.9)$$

Perform a change of variables such that $z = u + \varepsilon \delta u$.

$$\int \int p_t \cdot \delta w_t(x) \delta(x - \dot{\varphi}_t) dx - \frac{1}{2} \int z^T(x) A z(x) dx \Big|_{\varepsilon=0} = 0 \quad (3.10)$$

Apply the chain rule:

$$\int \int p_t \cdot \delta w_t(x) \delta(x - \dot{\varphi}_t) dx - \int z^T(x) A \frac{dz}{d\varepsilon} dx \Big|_{\varepsilon=0} = 0 \quad (3.11)$$

Change variables back:

$$\int \int p_t \cdot \delta w_t(x) \delta(x - \varphi_t) dx - \int w_t^T(x) A \delta w_t dx \Big|_{\varepsilon=0} = 0 \quad (3.12)$$

Recall that p_t and φ_t are functions of x . Apply integration by parts where $y = \varphi_t(x)$, $x = \varphi_t^{-1}(y)$, $dx = |D\varphi_t^{-1}(y)|dy$.

$$\int \left[\int p_t \cdot \delta(x - \varphi_t) - w_t^T A \right] \delta w_t(x) dx = 0 \quad (3.13)$$

Here, we recognized that the terms within the square brackets are set equal to zero.

$$\left(\int p_t \cdot \delta(x - \varphi_t) \right) - w_t(x)^T A = 0 \quad (3.14)$$

Solve for w_t :

$$w_t(\cdot) = \int K(\cdot, \varphi_t(x)) p_t(x) dx \quad (3.15)$$

3.1.5 Surface Matching Algorithm

For the experiments shown below, we assume that the infinitesimal mean drift μ_t of a given population is generated offline and is transported from the population space to the individual subjects' longitudinal trajectory $\mu_t^{(i)}, i = 1, \dots, N$. To estimate the mean drift, we model populations of time series of surfaces $S_{t_j}, t_j \in \{t_1, t_2, \dots, t_m\}$ viewed as longitudinal

observations from members of labeled cohorts undergoing disease modeling processes. In our setting, we have triangulated mesh cortical surfaces associated to studies such as ADNI [154] and BIOCARD [155]. We use current matching for surfaces [33] as adopted for LDDMM to generate the initial momentum fitting through the time-series [107, 114]. We solve for the variational solutions as an optimal control problem, defining the state $t \mapsto q_t = \varphi_t \cdot S$ and the control $t \mapsto v_t$ satisfying the dynamical equations of (3.4).

The time series of surfaces enters as input data with matching term given by the smooth energy $U : q_t \rightarrow R^+, t \in [0, 1]$ which drives the state through the target surfaces with pre-defined mean drift $\mu_t, t \in [0, 1]$. We pose the following control problem:

Control Problem :

$$\begin{aligned} \dot{\varphi}_t^{(i)} &= (\mu_t^{(i)} + w_t^{(i)}) \circ \varphi_t^{(i)}, \\ q_t^{(i)} &= \varphi_t^{(i)} \circ S_0, \quad q_0^{(i)} = S_0, \\ \min_{v_t, t \in [0, 1]} E(v) &:= \frac{1}{2} \int_0^1 \|w_t^{(i)}\|_V^2 dt + \int_0^1 U_t(q_t^{(i)}) dt . \end{aligned} \tag{3.16}$$

The Hamiltonian momentum satisfies Eqn. (3.4) with forces:

$$\dot{p}_t^{(i)} = -d(\mu_t^{(i)} + w_t^{(i)})^T \circ \varphi_t^{(i)} p_t^{(i)} + \frac{\partial U_t^{(i)}}{\partial q}(q_t^{(i)}) . \tag{3.17}$$

The energy $U_t, t \in [0, 1]$ is defined by the current matching norm on surfaces (see Sup-

plementary A) denoted as $\|\cdot\|_{\mathcal{S}}$:

$$U_t^{(i)}(q_t^{(i)}) = \sum_{t_j} \delta(t - t_j) \frac{1}{\sigma_m^2} \|q_{t_j}^{(i)} - S_{t_j}^{(i)}\|_{\mathcal{S}}^2. \quad (3.18)$$

We solve the minimization of this new control problem following the traditional method of matching onto surfaces which has been previously described for this class of problems [152].

3.1.6 Estimating Mean Drift of a Population

We now describe our method for computing the mean drift μ_t from a population of shapes. Figure 3.2 depicts the setting for our model assuming two populations, disease and control, each with their own mean drift representing their cohort. More generally, there can be any number of subpopulations.

The basic idea is to generate for each subject's time-series $i \in 1, 2, \dots, N$ the optimal momentum $p_{0,sub}^{(i)}$ by geodesic shooting of a single trajectory through a time-series, followed by transport of the trajectory's initial momentum into the common population coordinates where we average the momentum of each of the subjects to generate \bar{p}_0 . Each subject's LDDMM flow and initial momentum is transported into the population template coordinate space by computing the diffeomorphism $\Phi^{(i)}$ of the subject time-series onto the population template, and then coadjointly transporting [153] the initial momentum into the template population coordinates.

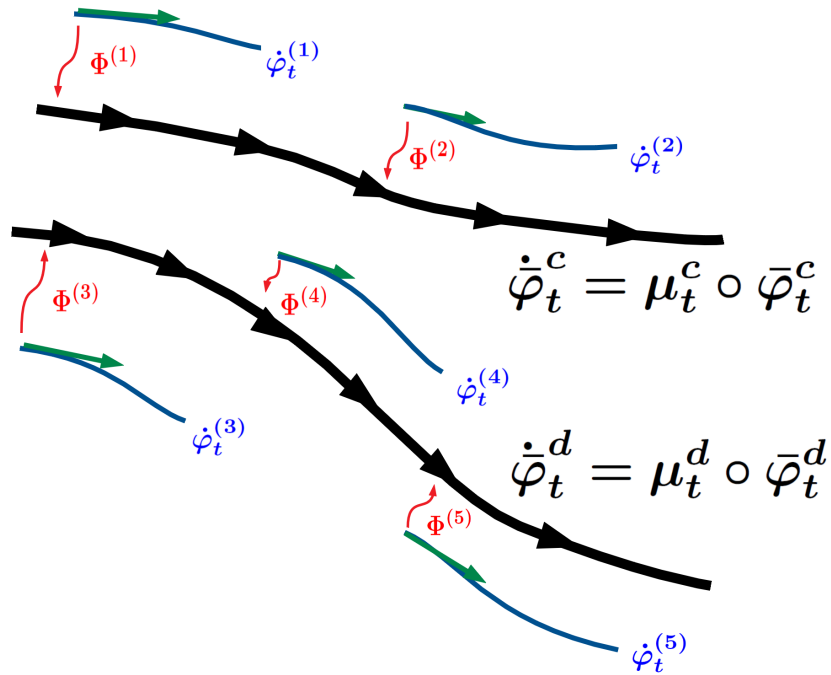


Figure 3.2: Estimating mean drifts associated to the two subpopulations of surfaces corresponding to labeled subjects forming the control (μ^c) and disease (μ^d) subgroups where subjects 1 and 2 belong to the control group and subjects 3-5 belong to the dementia group.

For all experiments shown we assume the time series are synchronized allowing us average the initial momentum of all subjects transported into population template coordinates. The average momentum \bar{p}_0 encodes the population drift μ_t for which we generate Hamiltonian equations for momentum evolution associated to the principles of least action.

To derive the mean drift in subject coordinates we coadjointly transport \bar{p}_0 back to the coordinates of each subject defined by the diffeomorphism $\Phi^{(i)}$ mapping the subject i to population coordinates. The coadjoint transport of any initial momentum seeded on discrete control points along $\Phi^{(i)}$ multiply used above is defined by the following (shown here

for transport of \bar{p}_0 into the coordinate space of subject i along $\Phi^{(i),-1}$:

$$\bar{p}_0^{(i)} = D[\Phi^{(i)}]^{-1}(\Phi^{(i)})^T \bar{p}_0([\Phi^{(i)}]) . \quad (3.19)$$

The coadjoint transport is derived from the classic EPDiff equation (Euler-Poincare equation) [156] and is written for continuous functions of p (i.e. for images):

$$\bar{p}_0^{(i)} = D[\Phi^{(i)}]^{-1}(\Phi^{(i)})^T \bar{p}_0(\Phi^{(i)}) |D\Phi^{(i)}| . \quad (3.20)$$

See Appendix C for proof of Eqn (3.20) from EPDiff. We arrive at (3.19) by taking the discrete representation in the case of surfaces and points. We note that other transport equations exist, such as parallel transport described for moving structures along geodesics [157], which may exhibit better properties than coadjoint transport. However, our focus here is not on the novelty of transport so we use coadjoint transport for its simplicity.

$\Phi^{(i)}$ can be determined in several ways – in our examples, we choose to compute $\Phi^{(i)}$ by mapping the first observation of each subject (for instance the first MRI in a longitudinal series of scans, hereafter termed the "baseline") to the template surface at the corresponding time point in the mean flow. Thus each subject's individual trajectory parameterized by $p_{0,sub}^{(i)}$ lies in the reference frame of the baseline but is seeded at control points corresponding to vertices of the template surface triangulation, ensuring $p_{0,sub}^{(i)}$ exists at corresponding points for all subjects.

Algorithm 1 Estimating Infinitesimal Mean Drift Representing Population Shape

Given: time-series surface $S_t^{(i)}$, $t \in \{t_1, \dots, t_m\}$ and mappings $\Phi^{(i)}$ to population template, $i = 1, \dots, N$:

Geodesic shoot $p_{0,sub}^{(i)}$ through time-series, $i = 1, \dots, N$.

Transport $p_{0,sub}^{(i)}$, $i = 1, \dots, N$ into population template using Eqn. (3.19) and average:

$$\bar{p}_0 = \frac{1}{N} \sum_{i=1}^N D\Phi^{(i)}([\Phi^{(i)}]^{-1})^T p_{0,sub}^{(i)}([\Phi^{(i)}]^{-1}) .$$

Generate population infinitesimal mean μ solving conservation laws from \bar{p}_0 .

Coadjoint transport template-space initial momentum into subject i coordinate space:

$$\bar{p}_{0,sub}^{(i)} = D[\Phi^{(i)}]^{-1}(\Phi^{(i)})^T \bar{p}_0(\Phi^{(i)}) .$$

Generate mean flow in subject-specific coordinates for each subject $i = 1, \dots, N$ from initial conditions $\bar{p}_0^{(i)}$:

$$\frac{d}{dt} \bar{p}_t^{(i)} = -d(\mu_t^{(i)})^T \bar{p}_t^{(i)}, \text{ i.c. } p_0^{(i)} \tag{3.21a}$$

$$\mu_t^{(i)} = \int K(\cdot, \varphi_t^{(i)}(x)) \bar{p}_t^{(i)}(x) dx . \tag{3.21b}$$

3.2 Results

3.2.1 Simulations based on Geodesic Shooting

We first apply our proposed model to simulated triangulated surface data. Illustrated in Figure 3.3, a disc-like surface and a cube-like surface are observed deforming over time by their own subject specific trajectories parameterized by $p_{0,sub}^{(i)}$. Each $p_{0,sub}^{(i)}$ is transported into the template coordinate space where the template is represented by a sphere. Here, the

momenta are averaged, producing \bar{p}_0 (purple vectors), the momentum parameterizing the mean drift. For simplicity, we show simulated data that are synchronized in time by their baseline observations with surface triangulations that have corresponding vertices.

Figure 3.4 shows examples of subject-specific deviations from the simulated drift of Figure 3.3. In this example, a pyramid-like subject changes longitudinally by expanding in the horizontal plane along an axis between two corners of the pyramid. The drift \bar{p}_0 can be transported into the space of this subject, producing $\bar{p}_{0,sub}^{(i)}$ (shown in purple vectors on the pyramid). The method described in (3.17) is used to compute the personalized control, shown in the bottom row. Naturally, because the pyramid expands from corner to corner with no change in any other direction while the drift expands in all directions, the resulting personalized control shows sharp expansion from corner to corner and shrinkage in all other directions. Shrinkage of a surface can be measured by several metrics. We choose to examine the log determinant of the jacobian of the deformation of the transported template surface in directions tangent to the surface, hereafter referred to as the "surface atrophy measure".

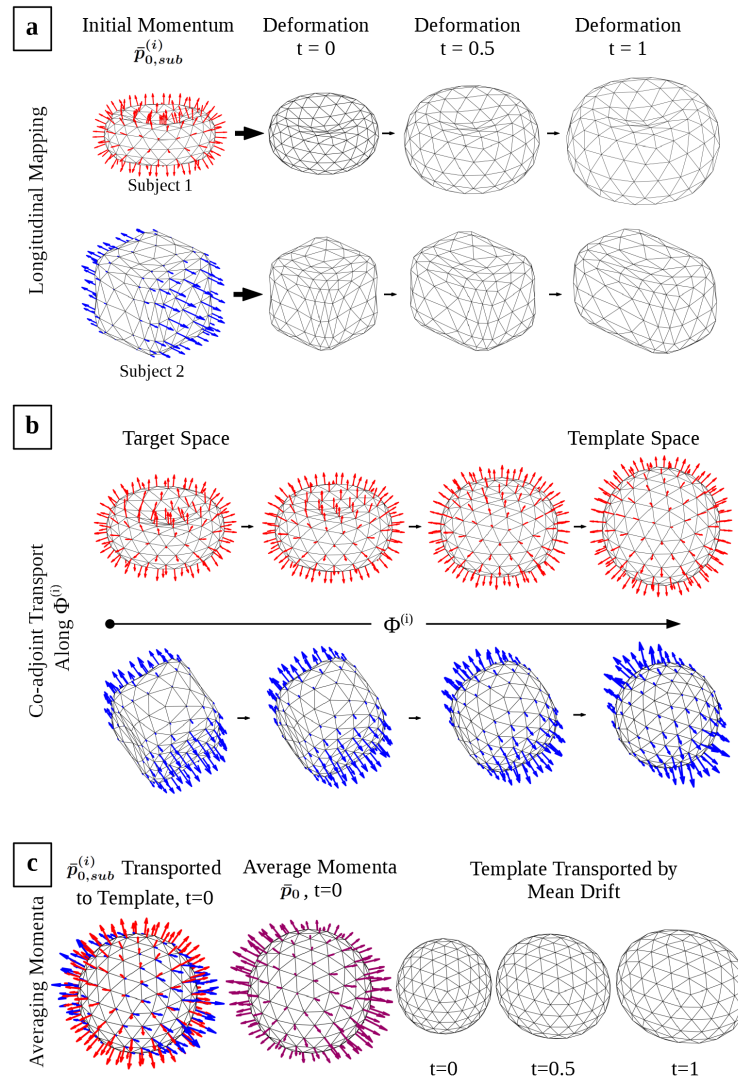


Figure 3.3: Longitudinal LDDMM shooting on simulated data computes the independent subject trajectories parameterized by initial momentum $p_{0,sub}^{(i)}$ shown as red and blue vectors in the left column of panel (a). The subject surface at time 0 is transported by $p_{0,sub}^{(i)}$, following the rightwards arrows for two subjects in panel (a) where subject 1 uniformly expands and subject 2 expands along a single axis. Panel (b) shows the initial momenta $p_{0,sub}^{(i)}$ transported into the template coordinate space by coadjoint transport along $\Phi^{(i)}$ for both subjects, where the template is chosen as a sphere. The transported momenta are averaged in template space in panel (c) to produce \bar{p}_0 in purple and the template surface is shown being transported by the mean drift resulting from \bar{p}_0 .

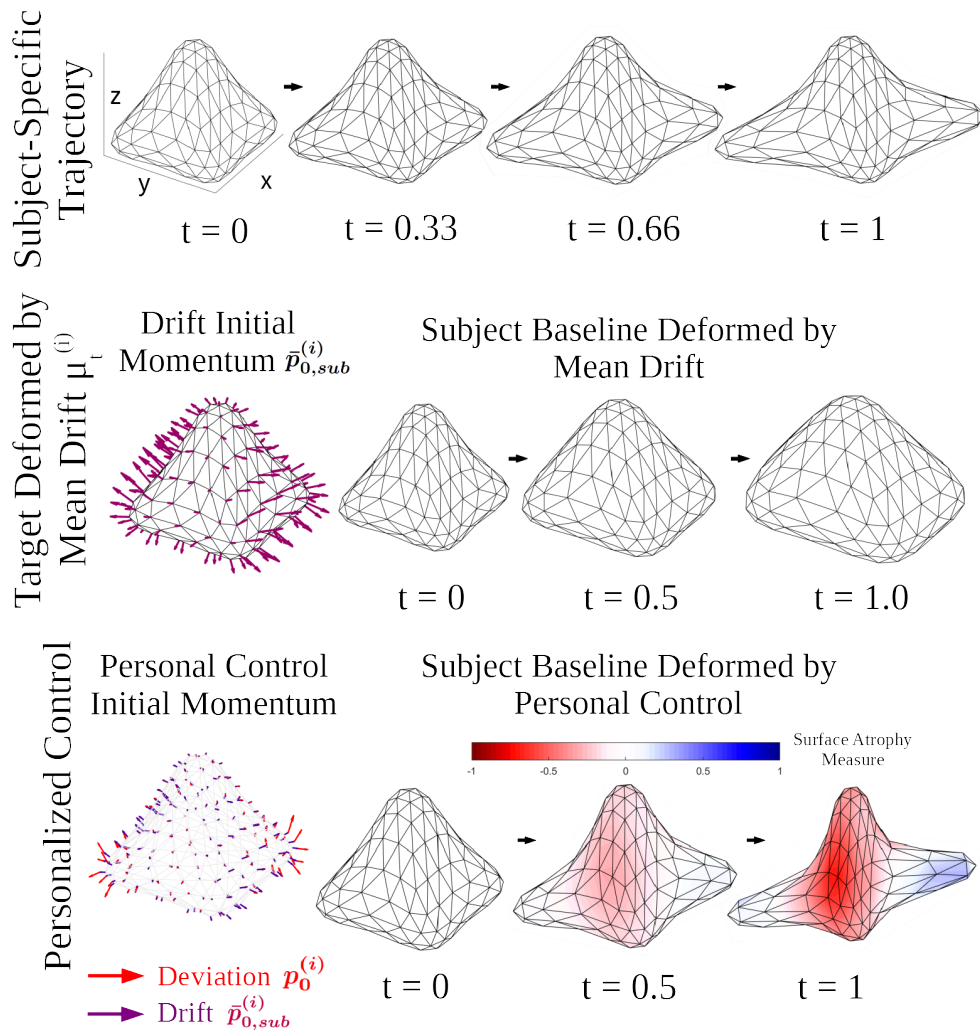


Figure 3.4: Personalized controls are shown for a simulated surface from the mean drift of Figure 3.3. The top row shows an individual subject’s longitudinal trajectory, in which a pyramid-like surface expands in one direction across two corners. The middle row shows the initial momentum parameterizing the mean drift $\mu_t^{(i)}$ in purple arrows (transported into the subject coordinate space) of Figure 3.3 and the baseline ($t = 0$) subject surface deformed by the flow resulting from the transported drift. The bottom left panel shows $p_0^{(i)}$ computed for this subject, the initial momentum parameterizing $w_t^{(i)}$, computed by (3.17). The panels to the right show the subject baseline surface deformed by the flow resulting from $w_t^{(i)}$ overlaid with the surface atrophy measure associated with the personalized control where red indicates shrinkage tangent to the surface.

3.2.2 Alzheimer’s Disease Neuroimaging Initiative

We apply our model to neuroimaging data from the Alzheimer’s Disease Neuroimaging Initiative dataset, a longitudinal imaging study of neurodegeneration in a patient population at risk for Alzheimer’s. The dataset contains 3T MRI scans for 57 patients (22 controls and 35 who developed dementia) over the course of two years with intervals at baseline, 6 months, 12 months, and 24 months and the patient cohorts have been examined by multiple prior studies. We extend our model to study the drift of two populations as illustrated in Figure 3.2.

For simplicity of demonstration we choose to chronologically synchronize all subjects to their baseline scan date, however we note that under our proposed framework any arbitrary synchronization can be used with no requirement for perfect temporally overlapped data. We then demonstrate the computation of the deviation of dementia patient group members from the mean drift of the normal population.

3.2.3 Surface Representation of Subcortical Structures in ADNI

We choose to examine longitudinal shape changes in the entorhinal and transentorhinal cortex (hereafter referred to as the entorhinal cortex) of the brain, a region which has previously been linked to Alzheimer’s Disease.

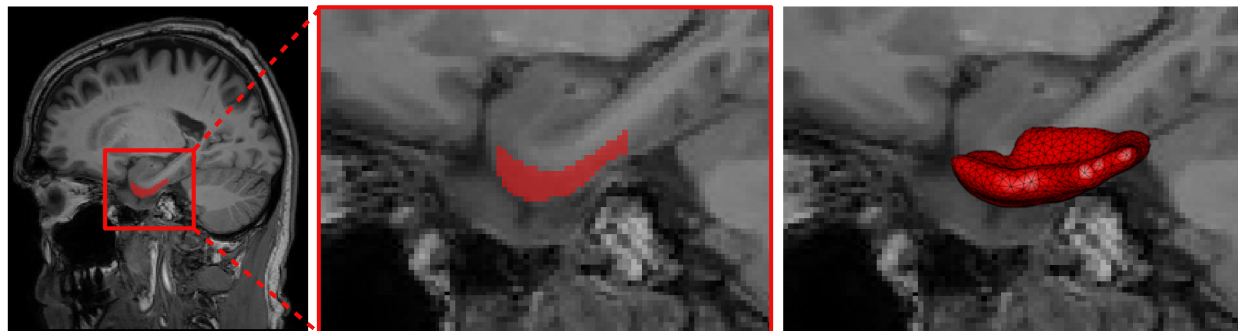


Figure 3.5: Surface generation process. (left) Sagittal view of 3T brain MRI in a section passing through the entorhinal cortex. (middle) Manual voxel-wise segmentations of the entorhinal and transentorhinal cortex are performed by anatomical experts. (right) Smooth triangulated surfaces are seeded on the segmentations.

Figure 3.5 illustrates the process of seeding triangulated surfaces onto the combination of these regions in MR. Manual voxel-wise binary segmentations of the entorhinal cortex were performed by anatomists and these segmentations were used to build smooth triangulated surfaces for each subject at every time point.

3.2.4 Computing the Drift of ADNI Populations

Bayesian template estimation [123] was performed on the baseline surfaces for the 57 subjects in order to build a template coordinate space at the baseline timepoint ($t=0$). The template surface T was then mapped to each subject baseline surface using diffeomorphic surface matching using a data attachment term based on currents [33], producing the transform $\Phi^{(i)}$ for $i \in 1, 2, \dots, 57$. Then, at each baseline timepoint for each subject, we have $\Phi^{(i)} \cdot T$ which is then mapped longitudinally through each subject's subsequent surfaces in a single trajectory

optimized to minimize the sum of currents between the deformed template and the subject's triangulated surface at each time point, producing $p_{0,sub}^{(i)}$ for $i \in 1, 2, \dots, 57$.

The initial momenta $p_{0,sub}^{(i)}$ parameterizing each independent subject specific trajectory are then transported into the template space using coadjoint transport and averaged to produce the population drift. We produce two population drifts: 1) the 22 control subjects who did not develop dementia and 2) the 35 subjects who did develop dementia.

In order to visualize the mean flow of each population, we transport the template surface along each computed drift. Snapshots of the deformed template sampled at selected time points along the continuous drift trajectory are shown in Figure 3.6 with each surface face colored by the log determinant of jacobian of the drift deformation tangent to the surface (where red indicates shrinkage).

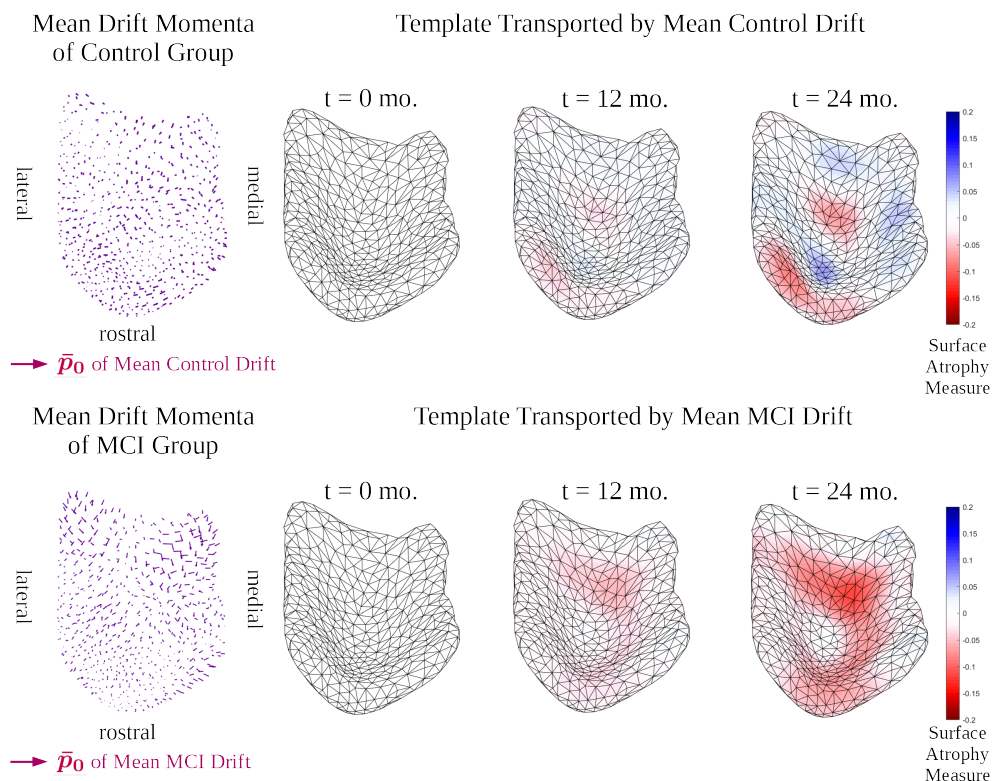


Figure 3.6: Population mean drift of ADNI patient cohort separated by control group and dementia group. The left column displays initial momentum vectors at each vertex of the template surface parameterizing the mean drift of each population. The right columns show the template surface deformed by the resulting flow of each population drift, sampled at baseline, one year, and two years. The surface atrophy measure is plotted on the flowing surfaces where red represents shrinkage tangent to the surface and blue represents expansion.

As expected, the mean drift of the control population fluctuates around identity. On the other hand, the mean drift of the dementia population shows obvious atrophy as evidenced by the red region in the bottom row of Figure 3.6. Measurements on our transported templates showed 1.6% volume loss in the control population and 8.3% volume loss in the dementia population. These values are in line with previous studies of entorhinal cortex

atrophy in Alzheimer’s Disease [107] and notably, the atrophy pattern measured by the drift qualitatively matches that observed in those studies.

3.2.5 Computing the Personalized Controls of ADNI Subjects

Having computed the drift of populations in the dataset, we can now apply our new biased geodesic shooting algorithm to compute the deviation or personalized control of individuals from the mean drift. For understanding biomarkers of Alzheimer’s Disease and dementia, we are interested in examining the deviation of entorhinal cortex atrophy of patients in the dementia group from the mean drift of the control group. This would inform us about the additional deformation imposed on each subject’s entorhinal cortex on top of the shape change associated with normal aging.

We apply the model of (3.4) in order to compute the personalized control of each individual. First, we transport the drift into the coordinate space of the subject. Since the drift is specified by the initial momentum \bar{p}_0 in our case, we once again coadjointly transport \bar{p}_0 into each subject coordinate space to obtain $\bar{p}_{0,sub}^{(i)}$. From there we can apply Eqn (3.17) to compute $w_t^{(i)}$ for each subject. Figure 3.7 shows two sample deviations from the drift from the dementia patient population overlaid with the surface atrophy measurement at selected time intervals.

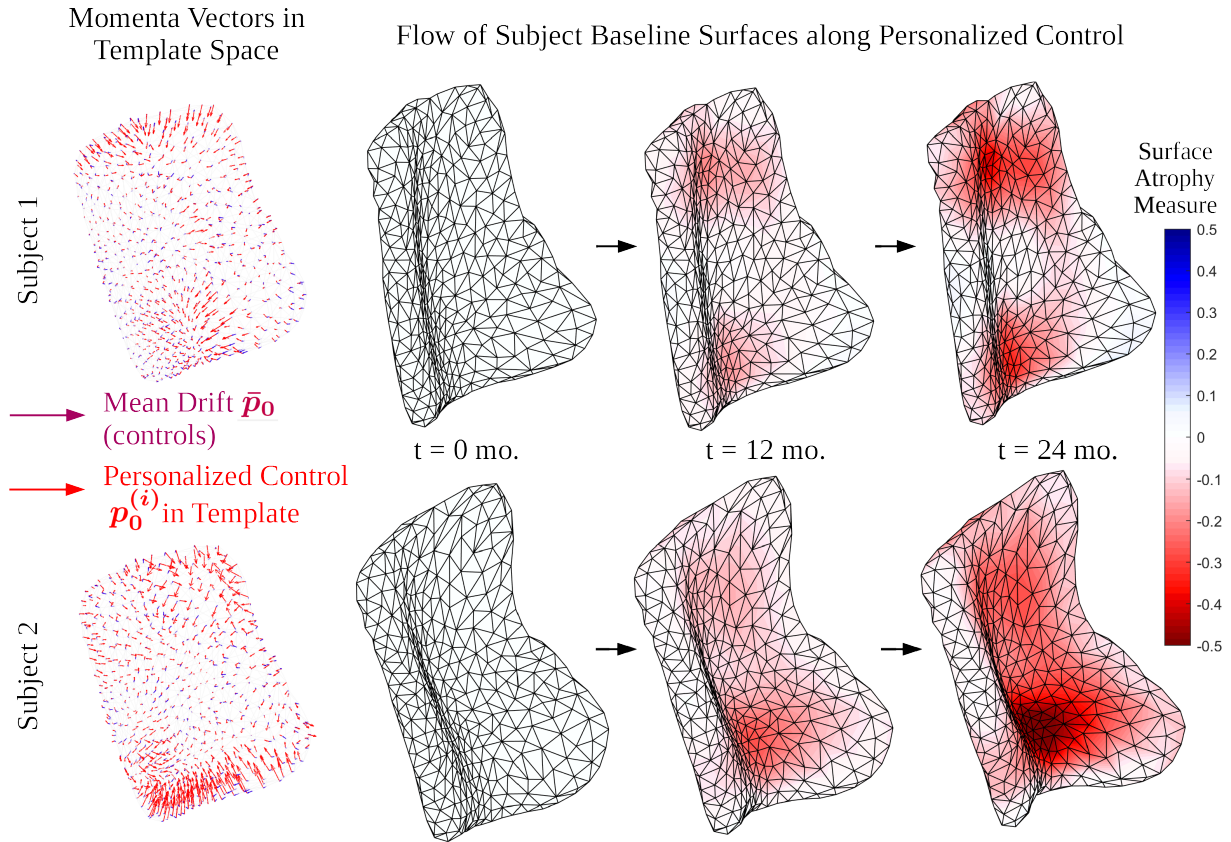


Figure 3.7: Personalized controls for two selected subjects from the dementia patient group. The left column shows the mean control population drift initial momentum \bar{p}_0 (in purple vectors, scaled linearly for visibility) along with the additional deviation computed to match the subject-specific observations $p_0^{(i)}$ transported to template space (in red vectors, scaled by the same linear factor). The right column shows the baseline surface of each subject deformed by the flow resulting from the personalized control only. The surface atrophy measure is plotted on the flowing surfaces where red represents shrinkage tangent to the surface and blue represents expansion.

In order to summarize the individual deviations for the entire patient population, we compute the individual deviations for all 37 subjects in the dementia patient group, as described above. The initial momenta parameterizing the flows associated to their personalized con-

trols are then coadjointly transported back into the template space and averaged using the same method of Algorithm 1 (Chapter 3). The resulting flow describes the average deviation in the shape of the entorhinal cortex of dementia patients from the mean drift characterizing the normal population. Figure 3.8 shows this mean deviation sampled at several time points. As expected, we generally observe a trend towards shrinkage of the entorhinal cortex in dementia patients away from the normal population drift. Our model shows precisely where this deviation occurs in specific patients as well as on the average.

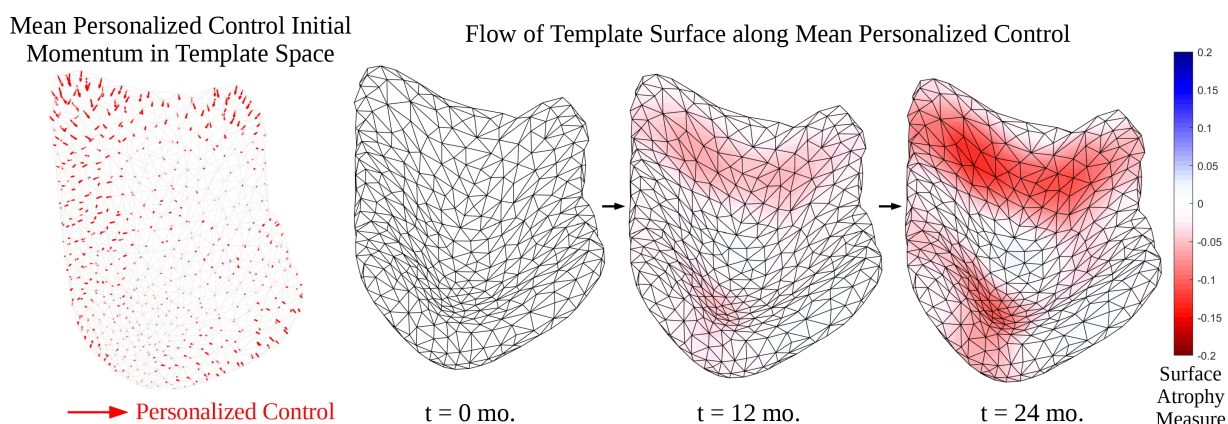


Figure 3.8: Mean personalized control parameterized by initial momentum vectors are shown in the left column. The template flowed along the trajectory defined by the mean personalized control is shown to the right, overlaid with the surface atrophy measure where red represents shrinkage.

3.3 Discussion

Here, we have introduced a new method for computing biased geodesics that describe deviations of subject-specific longitudinal trajectories, or "personalized controls", from a given

drift. We have described the dynamical systems framework that governs our model as well as an algorithm to solve for the personalized controls. Our biased geodesic shooting algorithm is inspired by physical modeling of the motion of particles, particularly related to the movement of particles along Hamiltonian flows. Where classic geodesic shooting can be viewed as describing the movement of a particle through space unperturbed by outside forces, we needed to model the movement of a particle influenced by a background drift. A simple analogy is to consider throwing a baseball across a field at a target on a windless versus a windy day.

Although other groups have examined linear subtractions of flows from one another to quantify differences between geodesic trajectories, our motivation was to estimate the deviation directly and in a more theoretically rigorous fashion. Our derivation of the biased geodesic shooting algorithm is motivated by this intention. Indeed, the deviant flows computed by our algorithm would not be the same as flows produced by linear subtraction of two flows to be compared, nor would they be the same as flows produced by initializing classic geodesic shooting by our drift term. We believe that our formulation is the natural one, primarily because the drift should not be penalized by regularization and should instead be treated as having no metric cost (like identity). For instance, consider an example where the drift is a trajectory with a high metric cost (less smoothness) and the target individual's longitudinal trajectory is identity. Classic geodesic shooting would exactly match the target trajectory with a regularization cost of zero. This could produce trajectories that are not

properly regularized, biasing all other estimations towards identity. Our method is unbiased with respect to the drift, and all transformations are properly regularized with respect to smooth deformations away from the drift. From a generative perspective, we would expect random observations in a longitudinal population to be centered around the drift and not around identity.

We solve the control problem of mapping a template onto members of a population using surface matching of triangulated meshes onto targets. One of the strengths of the method's design is that it can be generalized to include volumes or landmarks, as well as to simultaneously optimize the mean flow along with each individual's personalized flow. Although we pre-compute the mean drift in this work, the natural extension is to optimize the drift jointly with the personalized controls. Such an extension would be motivated by the ideas behind the template estimation algorithm – that is, that the mean drift of a population should be the one that minimizes the personalized controls of its own population. This would be an expansion of the template estimation algorithm where instead of estimating the template at a single timepoint, the template coordinate space would be represented as a time-varying flow. Our biased geodesic shooting algorithm could enable this computation.

Chapter 4

Conclusion

In this work, we developed algorithms for two related classes of problems: spatial image analysis and longitudinal image analysis. Our work was grounded in the computational anatomy random orbit model. Our use of the random orbit model allowed us to generatively model the observations of serially sectioned imagery with random distortions, as well as longitudinal imagery from a population.

We first discussed our extension to the random orbit model to accommodate imagery that is serially acquired in space. We present a variational framework for dense diffeomorphic atlas-mapping serially sectioned image volumes. The observed sections are modelled as Gaussian random fields conditioned on a sequence of unknown section by section rigid motions and unknown diffeomorphic transformation of a three-dimensional atlas. To regularize over the high-dimensionality of our parameter space (which is a product space of the rigid motion

dimensions and the diffeomorphism dimensions), the 2D stacks are modelled as arising from a first order Sobolev space smoothness prior. We show that the joint maximum a-posteriori, penalized-likelihood estimator of our high dimensional parameter space emerges as a joint optimization interleaving rigid motion estimation for volume reconstruction and large deformation diffeomorphic metric mapping to atlas coordinates. We show that joint optimization in this parameter space solves the classical curvature non-identifiability of the volume reconstruction problem. The algorithms are demonstrated on a collection of whole-brain histological image stacks from the Mouse Brain Architecture Project and the Brain/MINDS marmoset imaging study. The advantage of embedding our algorithms in the random orbit model is the immediate accessibility of diffeomorphic measurements between any subject that has been mapped into common coordinates. We demonstrate the power of this method by providing the most localized quantitative analysis of tissue deformation caused by the histological processing procedure to date.

This work has been developed into a comprehensive pipeline currently being used by members of the NIH Brain Initiative's Cell Consensus Network working group. Our pipeline has been used to reconstruct and map thousands of brains, and initial connectivity matrices have been developed based on our work in mouse and marmoset models. We believe that future work in this area will focus on the problem of interpreting the high-resolution and dense connectivity information present in our reconstructions for the purpose of understanding the basic function of the brain as well as understanding how pathologies disrupt these con-

netions. Additionally, the issue of computational time is highly relevant to our work, where there is a need to reconstruct and register thousands of tera-voxel image volumes. Towards this end, we have developed comprehensive software packages to perform GPU-accelerated diffeomorphic registration and reconstruction operations in Python, and we expect future work will contribute to even more efficient processing.

The second half of this work extended the random orbit model to computing differences between geodesic trajectories in a longitudinally imaged population. The study of morphometry in longitudinal populations has been an active area of study for decades. Prior work focused on statistical methods such as linear mixed-effects modeling, whereas our model was the first to directly embed the estimation of individual deviations from a mean into the diffeomorphism model. Our model is inspired by models of Brownian motion with drift, in which the motion of particles through space is modeled as being from two sources. We extend the concept of Hamiltonian flows that define geodesics to what we term "biased geodesics", or trajectories that result from particles moving through space acted on by an outside drift as well as their own momentum. We solve the control problem of mapping a template onto members of a population using surface matching of triangulated meshes onto targets. This method can be generalized to include volumes or landmarks, as well as to simultaneously optimize the mean flow along with each individual's personalized flow. We emphasize that there is no penalty on the drift generated from the population as we assume the drift is of dimension consistent with that of the population from which it was estimated. Our algorithm

treats the mean drift as having no metric cost like identity, and as a result, deviations from that drift are more naturally penalized. For this reason, we use LDDMM shooting onto the population to control the initial dimensions of the mean drift as the order of the database is limited.

In our experiments on entorhinal cortical surfaces from the ADNI dataset, we show that we are able to compute a realistic mean drift of two diagnostic groups within the patient cohort under our model, and that we are able to compute the deviations of dementia group individuals from the normal population drift as well as compute the mean deviation in a common coordinate space. Our work here is intended as a methodological demonstration and the clear limitation is that our results may not necessarily be clinically relevant due to our simplifications, such as the choice of time synchronization. We expect that future work will refine these choices in order to draw clinical conclusions about Alzheimer's, for instance by selecting a more intelligent synchronization that aligns subjects based on the true onset and progression of the disease. Additionally, we propose that the model can easily be generalized in a scheme similar to Bayesian template estimation in order to jointly optimize the mean drift itself, potentially further improving the accuracy of the model.

Understanding the structure of the neural circuitry and how it governs the function of the brain and is disrupted by pathological neurodegeneration is a monumental task with high clinical relevance. Our work in medical imaging and shape analysis is just one part of the tremendous effort that goes into making discoveries in this field. We believe that the

algorithms we developed are among the state-of-the-art for studying the brain constrained by the smoothness and continuity of human anatomy. The algorithms here have been presented in a generative fashion which we believe most closely models real life observations, and we are hopeful that such methods will contribute to the understanding of the human brain.

Appendix A

Reproducing Kernel Hilbert Space and Green's Kernel.

The Green's kernel is translation invariant and takes the form

$$K(x, y, z) = k(x, y, z)Id_3 ,$$

with Id_3 the 3×3 identity matrix, for the Green's function continuously differentiable:

$$k(x, y, z) = 4 \left(3 + 3\sqrt{x^2 + y^2 + z^2} + 3(x^2 + y^2 + z^2) \right) e^{-\sqrt{x^2 + y^2 + z^2}} .$$

This Green's function satisfies $(-\nabla^2 + 1)^4 k(x, y, z) = \delta(x, y, z)$, where $(-\nabla^2 + 1)^4$ is referred to as A . The reproducing kernel Hilbert space (RKHS) with this Green's kernel corresponds

to vector fields satisfying

$$\|v\|_V^2 = \sum_{i=1}^3 \int_{\mathbb{R}^3} ((-\nabla^2 + 1)v_i(x, y, z))^2 dx dy dz < \infty .$$

Appendix B

Geodesics solving Euler-Lagrange Equations.

The explicit equations for geodesics associated to the RKHS norm $\|v\|_V$ and the geodesics satisfy the Euler-Lagrange equations [6, 125] given by the triple of equations.

$$\begin{cases} \dot{\varphi}_t = v_t \circ \varphi_t \\ \dot{p}_t = -(dv_t)^T \circ \varphi_t p_t \\ v_t = \int_{\mathbb{R}^3} K(x, \varphi_t(y)) p_t(y) dy, \quad Av_0 = p_0. \end{cases} \quad (\text{B.1})$$

To prove the Hamiltonian momentum evolution, the second equation $\dot{p} = -(dv)^T \circ \varphi p$ of (B.1) for Av a classical function we use the inner product notation $\langle \cdot, \cdot \rangle$ to calculate the

Lagrangian:

$$L(\varphi, \dot{\varphi}) = \frac{1}{2} \langle A\dot{\varphi} \circ \varphi^{-1}, \dot{\varphi} \circ \varphi^{-1} \rangle = \frac{1}{2} \int_{\mathbb{R}^3} A(\dot{\varphi} \circ \varphi^{-1}(x)) \cdot \dot{\varphi} \circ \varphi^{-1}(x) dx ,$$

with the variation giving the Euler-Lagrange equations:

$$\frac{d}{dt} \underbrace{\partial_{\dot{\varphi}} L(\varphi, \dot{\varphi})}_{\text{Ham. mom. p}} - \partial_{\varphi} L(\varphi, \dot{\varphi}) = 0.$$

To get the Hamiltonian momentum $p = \partial_{\dot{\varphi}} L(\varphi, \dot{\varphi})$, we take variation with respect to Lagrangian velocity $\dot{\varphi} \rightarrow \dot{\varphi}^\varepsilon = \dot{\varphi} + \varepsilon \delta \dot{\varphi}$ and $\varphi \rightarrow \varphi + \varepsilon \delta \varphi$ giving

$$\begin{aligned} \frac{d}{d\varepsilon} L(\varphi^\varepsilon, \dot{\varphi}^\varepsilon)|_{\varepsilon=0} &= \frac{d}{d\varepsilon} \frac{1}{2} \langle A(\dot{\varphi}^\varepsilon \circ \varphi^{-1}), \dot{\varphi}^\varepsilon \circ \varphi^{-1} \rangle |_{\varepsilon=0} \\ &= \frac{d}{d\varepsilon} \frac{1}{2} \left(\langle Av, \dot{\varphi}^\varepsilon \circ \varphi^{-1} \rangle + \langle A(\dot{\varphi}^\varepsilon \circ \varphi^{-1}), v \rangle \right) |_{\varepsilon=0} \end{aligned}$$

Combining gives the Hamiltonian momentum :

$$\langle Av, \frac{d}{d\varepsilon} (\dot{\varphi} + \varepsilon \delta \dot{\varphi}) \circ \varphi^{-1} \rangle = \langle \underbrace{Av \circ \varphi |d\varphi|}_{\partial_{\dot{\varphi}} L \text{ Ham. mom.}}, \delta \dot{\varphi} \rangle .$$

The variation $\varphi \rightarrow \varphi^\varepsilon = \varphi + \varepsilon \delta \varphi$ requires the inverse:

$$(\varphi^{-1} + \varepsilon \delta \varphi^{-1}) \circ (\varphi + \varepsilon \delta \varphi) \simeq \text{id} + \varepsilon (d\varphi^{-1})|_{\varphi} \delta \varphi + \varepsilon \delta \varphi|_{\varphi}^{-1}$$

which gives first order perturbation

$$\delta\varphi^{-1} = -(d\varphi^{-1})\delta\varphi|_{\varphi^{-1}} = -(d\varphi)_{\varphi^{-1}}^{-1}\delta\varphi|_{\varphi^{-1}} . \quad (\text{B.2})$$

Taking a similar variation of the Lagrangian as above but with respect to the Lagrangian velocity gives

$$\begin{aligned} \langle Av, \frac{d}{d\varepsilon}(\dot{\varphi} \circ (\varphi^{-1} - \varepsilon(d\varphi)_{\varphi^{-1}}^{-1}\delta\varphi|_{\varphi^{-1}})) \rangle &= -\langle Av, (dv)(d\varphi)|_{\varphi^{-1}}(d\varphi)_{\varphi^{-1}}^{-1}\delta\varphi|_{\varphi^{-1}} \rangle \\ &= -\underbrace{\langle (dv)_{\varphi}^T Av \circ \varphi|d\varphi|, \delta\varphi \rangle}_{\partial_{\varphi}L} \end{aligned} \quad (\text{B.3})$$

The third equation of (B.1) follows from $p = Av \circ \varphi|d\varphi|$. Integrating with the Green's kernel gives the expression $v_t(\cdot) = \int K(\cdot, \varphi_t(y))p_t(y)dy$.

Appendix C

Coadjoint Transport

We show the coadjoint transport property for initial momentum p_0 and diffeomorphism Φ_t , partially derived from [153, 158]:

$$p_t = D\Phi_t(\Phi_t^{-1})^T p_0(\Phi_t^{-1}) |D\Phi_t^{-1}| \quad (\text{C.1})$$

This can also be written:

$$p_t(x) = [D\Phi_t^{-1}]^T p_0(\Phi_t^{-1}) |D\Phi_t^{-1}| \quad (\text{C.2})$$

Compose:

$$p_t(\Phi_t) = [D\Phi_t^{-1}(\Phi_t)]^T p_0 |D\Phi_t^{-1}(\Phi_t)| \quad (\text{C.3})$$

$$p_t(\Phi_t) = [D\Phi_t]^{-T} p_0 |D\Phi_t^{-1}| \quad (\text{C.4})$$

$$|D\Phi_t| p_t(\Phi_t) = [D\Phi_t]^{-T} p_0 \quad (\text{C.5})$$

Take derivative of the right side with respect to time:

$$\frac{d}{dt}[D\Phi_t]^{-1} = -[D\Phi_t]^{-1} \frac{d}{dt}[D\Phi_t][D\Phi_t]^{-1} \quad (\text{C.6})$$

$$= -[D\Phi_t]^{-1} D[v_t(\Phi_t)][D\Phi_t]^{-1} \quad (\text{C.7})$$

$$= -[D\Phi_t]^{-1} Dv_t(\Phi_t) D\Phi_t [D\Phi_t]^{-1} \quad (\text{C.8})$$

$$= -[D\Phi_t]^{-1} Dv_t(\Phi_t) \quad (\text{C.9})$$

This gives from (C.5):

$$|D\Phi_t| p_t(\Phi_t) = -Dv_t(\Phi_t)^T [D\Phi_t]^{-T} p_0 \quad (\text{C.10})$$

Take derivative of the left side with respect to time:

$$\frac{d}{dt}[|D\Phi_t| p_t(\Phi_t)] = |D\Phi_t| \operatorname{div}[v_t](\Phi_t) p_t(\Phi_t) + |D\Phi_t| \frac{d}{dt} p_t(\Phi_t) + |D\Phi_t| Dp_t(\Phi_t) v_t(\Phi_t) \quad (\text{C.11})$$

Equate the two sides:

$$|D\Phi_t|\operatorname{div}[v_t](\Phi_t)p_t(\Phi_t) + |D\Phi_t|\frac{d}{dt}p_t(\Phi_t) + |D\Phi_t|Dp_t(\Phi_t)v_t(\Phi_t) = -Dv_t(\Phi_t)^T[D\Phi_t]^{-T}p_0 \quad (\text{C.12})$$

Multiply by Jacobian:

$$\operatorname{div}[v_t](\Phi_t)p_t(\Phi_t) + \frac{d}{dt}p_t(\Phi_t) + Dp_t(\Phi_t)v_t(\Phi_t) = -Dv_t(\Phi_t)^T[D\Phi_t]^{-T}p_0|[D\Phi_t]^{-1}| \quad (\text{C.13})$$

Compose with Φ_t^{-1} :

$$\operatorname{div}[v_t]p_t + \frac{d}{dt}p_t + Dp_tv_t = -Dv_t^T[D\Phi_t(\Phi_t^{-1})]^{-T}p_0(\Phi_t^{-1})|[D\Phi_t(\Phi_t^{-1})]^{-1}| \quad (\text{C.14})$$

The Jacobian of the RHS is $|D\Phi_t^{-1}|$. Recover p_t on the right to get:

$$\operatorname{div}[v_t]p_t + \frac{d}{dt}p_t + Dv_tp_t = -Dv_t^T p_t \quad (\text{C.15})$$

Rearrange to recover the EPDiff equation:

$$\frac{d}{dt}p_t = -Dp_tv_t - \operatorname{div}[v_t]p_t - Dv_t^T p_t \quad (\text{C.16})$$

Bibliography

- [1] M Faisal Beg et al. “Computing Large Deformation Metric Mappings via Geodesic Flows of Diffeomorphisms”. In: *International Journal of Computer Vision* 61.2 (2005), pp. 139–157. ISSN: 09205691. DOI: 10.1023/B:VISI.0000043755.93987.aa. URL: <http://www.springerlink.com/openurl.asp?id=doi:10.1023/B:VISI.0000043755.93987.aa>.
- [2] Ulf Grenander and Michael I Miller. “Computational anatomy: An emerging discipline”. In: *Quarterly of Applied Mathematics* 56.4 (1998), pp. 617–694. ISSN: 0033569X. DOI: 10.1090/qam/1668732. URL: <http://portal.acm.org/citation.cfm?id=309082.309089>.
- [3] P Dupuis, U Grenander, and MI Miller. “Variation Problems on Flows of Diffeomorphisms for Image Matching”. In: *Quarterly of Applied Mathematics* LVI.4 (3 1998), pp. 587–600.

- [4] MI Miller and L Younes. “Group Actions, Homeomorphisms, and Matching: A General Framework”. In: *International Journal of Computer Vision* 41.4 (1-2 2001), pp. 61–84. DOI: 10.1023/A:1011161132514.
- [5] A Toga and PM Thompson. “Maps of the Brain”. In: *Anat Rec.* 265.2 (2001), pp. 37–53.
- [6] Michael I Miller, Alain Trouvé, and Laurent Younes. “On the metrics and euler-lagrange equations of computational anatomy.” In: *Annual Review of Biomedical Engineering* 4.1 (2002), pp. 375–405. DOI: 10.1146/annurev.bioeng.4.092101.125733. URL: <http://www.ncbi.nlm.nih.gov/pubmed/12117763>.
- [7] Paul M Thompson and Arthur W Toga. “A framework for computational anatomy”. In: *Computing and Visualization in Science* 5.1 (2002), pp. 13–34. ISSN: 14329360. DOI: 10.1007/s00791-002-0084-6. URL: <http://www.springerlink.com/openurl.asp?genre=article&id=doi:10.1007/s00791-002-0084-6>.
- [8] MI Miller. “Computational anatomy: shape, growth, and atrophy comparison via diffeomorphisms”. In: *Neuroimage* 29.Suppl 1:S (2004), pp. 19–33.
- [9] Mirza Faisal Beg et al. “Computational cardiac anatomy using MRI”. In: *Magnetic Resonance in Medicine: An Official Journal of the International Society for Magnetic Resonance in Medicine* 52.5 (2004), pp. 1167–1174.

- [10] Sarang Joshi et al. “Unbiased diffeomorphic atlas construction for computational anatomy”. In: *NeuroImage* 23 (2004), S151–S160.
- [11] J Ashburner and K J Friston. “Computational anatomy”. In: *Statistical Parametric Mapping The Analysis of Functional Brain Images*. Ed. by K J Friston et al. Academic Press, 2007, pp. 49–100.
- [12] M Grenander and MI Miller. *Pattern Theory: From Representation to Inference*. ISBN 978-0199297061. Oxford Press, 2007.
- [13] Stanley Durrleman et al. “Inferring brain variability from diffeomorphic deformations of currents: an integrative approach.” In: *Medical Image Analysis* 12.5 (2008), pp. 626–637. URL: <http://www.pubmedcentral.nih.gov/articlerender.fcgi?artid=2572735&tool=pmcentrez&rendertype=abstract>.
- [14] J Ashburner. “Computational Anatomy with the SPM Software”. In: *Magnetic Resonance Imaging* 27 (8 2009), pp. 1163–1174.
- [15] Laurent Younes, Felipe Arrate, and Michael I Miller. “Evolutions equations in computational anatomy”. In: *NeuroImage* 45.1 (2009), S40–S50.
- [16] L Younes. *Shapes and Diffeomorphisms*. Vol. 171. XVI. Series: Applied Mathematical Sciences, 2010, 438 pages.
- [17] X Pennec. “From Riemannian Geometry to Computational Anatomy”. In: *Elements* (2011).

- [18] Rick A Adams et al. “The computational anatomy of psychosis”. In: *Frontiers in psychiatry* 4 (2013), p. 47.
- [19] R Bajcsy, R Lieberman, and M Reivich. “A computerized system for the elastic matching of deformed radiographic images to idealized atlas images.” In: *J Comput Assist Tomogr* 7 (4 1983), pp. 618–625.
- [20] R Bajcsy and S Kovačič. “Multiresolution elastic matching”. In: *Computer Vision, Graphics, and Image Processing* 46 (1 1989), pp. 1–21.
- [21] Y Amit, U Grenander, and M Piccioni. “Structural Image Restoration through Deformable Templates”. In: *Journal of the American Statistical Association* 86.414 (1991), pp. 376–381.
- [22] James C Gee, Martin Reivich, and Ruzena Bajcsy. “Elastically Deforming a Three-Dimensional Atlas to Match Anatomical Brain Images”. In: *University of Pennsylvania Institute for Research in Cognitive Science Technical Report No. IRCS-93-37* (1993).
- [23] M I Miller et al. “Mathematical textbook of deformable neuroanatomies”. In: *Proceedings of the National Academy of Sciences* 90.24 (1993), pp. 11944–11948. ISSN: 0027-8424. DOI: 10.1073/pnas.90.24.11944. eprint: <http://www.pnas.org/content/90/24/11944.full.pdf>.

- [24] *Mapping of hyperelastic deformable templates using the finite element method*. Vol. 2573. 1995, pp. 2573–2573–14. DOI: 10.1117/12.216419.
- [25] Gary Christensen, Michael I. Miller, and Richard D. Rabbit. “Deformable templates using large deformation kinematics”. In: *IEEE Transactions of Medical Imaging* 5 (10 1995), pp. 1435–1447. DOI: 10.1109/83.536892. URL: <http://en.scientificcommons.org/43056763>.
- [26] Gary E. Christensen, Sarang C. Joshi, and Michael I. Miller. “Volumetric Transformation of Brain Anatomy”. In: *IEEE TRANSACTIONS ON MEDICAL IMAGING* 16.6 (1997), pp. 864–877.
- [27] F. L. Bookstein. “Principal Warps: Thin-Plate Splines and the Decomposition of Deformations”. In: *IEEE Trans. Pattern Anal. Mach. Intell.* 11.6 (June 1989), pp. 567–585. ISSN: 0162-8828. DOI: 10.1109/34.24792. URL: <http://dx.doi.org/10.1109/34.24792>.
- [28] Fred L Bookstein. “Thin-plate splines and the atlas problem for biomedical images”. In: *Biennial International Conference on Information Processing in Medical Imaging*. Springer. 1991, pp. 326–342.
- [29] F.L. Bookstein. “Biometrics, Biomathematics and the Morphometric Synthesis”. In: *Bulletin of Mathematical Biology* 58.2 (1996), pp. 313–365.

- [30] SC Joshi and MI Miller. “Landmark matching via large deformation diffeomorphisms”. In: *IEEE Trans Image Process* 9.8 (2000), pp. 1357–70. ISSN: doi: 10.1109/83.855431.
- [31] Vincent Camion and Laurent Younes. “Geodesic interpolating splines”. In: *Energy Minimization Methods in Computer Vision and Pattern Recognition*. Springer Berlin/Heidelberg. 2001, pp. 513–527.
- [32] Joan Glaunes, Alain Trouvé, and Laurent Younes. “Diffeomorphic matching of distributions: A new approach for unlabelled point-sets and sub-manifolds matching”. In: *Computer Vision and Pattern Recognition, 2004. CVPR 2004. Proceedings of the 2004 IEEE Computer Society Conference on*. Vol. 2. Ieee. 2004, pp. II–712.
- [33] Marc Vaillant and Joan Glaunès. “Surface matching via currents”. In: *Proceedings of Information Processing in Medical Imaging (IPMI 2005), number 3565 in Lecture Notes in Computer Science*. 2005, pp. 381–392.
- [34] Joan Glaunès et al. “Large Deformation Diffeomorphic Metric Curve Matching”. In: *International Journal of Computer Vision* 80.3 (2008), pp. 317–336.
- [35] Brian Avants and James C Gee. “Geodesic estimation for large deformation anatomical shape averaging and interpolation”. In: *Neuroimage* 23 (2004), S139–S150.
- [36] Mirza Faisal Beg and Ali Khan. “Symmetric data attachment terms for large deformation image registration”. In: *IEEE Transactions on Medical Imaging* 26.9 (2007), pp. 1179–1189.

- [37] Tom Vercauteren et al. “Symmetric log-domain diffeomorphic registration: A demonstration-based approach”. In: *International Conference on Medical Image Computing and Computer-Assisted Intervention*. Springer. 2008, pp. 754–761.
- [38] Brian B Avants et al. “Symmetric diffeomorphic image registration with cross-correlation: evaluating automated labeling of elderly and neurodegenerative brain”. In: *Medical Image Analysis* 12.1 (2008), pp. 26–41.
- [39] C Ceritoglu et al. “Multi-contrast large deformation diffeomorphic metric mapping for diffusion tensor imaging”. In: *Neuroimage* 47.2 (2009), pp. 618–27. ISSN: doi: 10.1016/j.neuroimage.2009.04.057. Epub 2009 May 3. DOI: 10.1016/j.neuroimage.2009.04.057.
- [40] Can Ceritoglu et al. “Large deformation diffeomorphic metric mapping registration of reconstructed 3D histological section images and in vivo MR images”. In: *Frontiers in Human Neuroscience* 4 (2010), p. 43.
- [41] Laurent Risser et al. “Simultaneous Multi-scale Registration Using Large Deformation Diffeomorphic Metric Mapping.” In: *IEEE Transactions on Medical Imaging* 30.10 (2011), pp. 1746–59. ISSN: 15580062. DOI: 10.1109/TMI.2011.2146787. URL: <http://www.ncbi.nlm.nih.gov/pubmed/21521665>.

- [42] Stefan Sommer et al. “A multi-scale kernel bundle for LDDMM: towards sparse deformation description across space and scales.” In: *Information processing in medical imaging proceedings of the conference 22.17* (2011), pp. 624–635.
- [43] DJ Tward et al. “Patient Specific Dosimetry Phantoms Using Multichannel LDDMM of the Whole Body”. In: *International Journal of Biomedical Imaging* 2011 (). ISSN: Article ID 481064, 9 pages, 2011. doi:10.1155/2011/481064a.
- [44] Jia Du, L Younes, and A Qiu. “Whole brain diffeomorphic metric mapping via integration of sulcan and gyral curves, cortical surfaces, and images”. In: *Neuroimage* 56.1 (2011), pp. 162–173.
- [45] F Vadakkumpadan et al. “Image-Based Estimation of Ventricular Fiber Orientations for Personalized Modeling of Cardiac Electrophysiology”. In: *IEEE Transactions on Medical Imaging* 31.5 (2012), pp. 1051 –1060.
- [46] X Tang, S Mori, and MI Miller. “Segmentation via multi-atlas LDDMM”. In: *MICCAI 2012 Workshop on Multi-Atlas Labeling* (2012), pp. 123–133.
- [47] Jia Du, Alvina Goh, and Anqi Qiu. “Diffeomorphic metric mapping of high angular resolution diffusion imaging based on riemannian structure of orientation distribution functions”. In: *IEEE Transactions on Medical Imaging* 31.5 (2012), pp. 1021–1033.

- [48] Jia Du et al. “Diffeomorphic metric mapping and probabilistic atlas generation of hybrid diffusion imaging based on BFOR signal basis”. In: *Medical Image Analysis* 18.7 (2014), pp. 1002–1014.
- [49] Laurent Risser et al. “Piecewise-diffeomorphic image registration: Application to the motion estimation between 3D CT lung images with sliding conditions”. In: *Medical Image Analysis* 17.2 (2013), pp. 182–193.
- [50] DJ Tward et al. “Robust Diffeomorphic Mapping via Geodesically Controlled Active Shapes”. In: *International Journal of Biomedical Imaging* Article ID 205494 (2013), 19 pages.
- [51] Ali R Khan, Lei Wang, and Mirza Faisal Beg. “Multistucture large deformation diffeomorphic brain registration”. In: *IEEE Transactions on Biomedical Engineering* 60.2 (2013), pp. 544–553.
- [52] U Grenander. *General Pattern Theory*. ISBN 978-0198536710. Oxford Science Publications, 1994.
- [53] Michael I Miller, Alain Trouvé, and Laurent Younes. “Diffeomorphometry and geodesic positioning systems for human anatomy”. In: *Technology* 1:36 (2014).
- [54] O. Sporns, G. Tononi, and R. Kotter. “The human connectome: A structural description of the human brain.” In: *PLoS Comp Biol* 1 (2005), pp. 245–251. DOI: 10.1371/journal.pcbi.0010042.

- [55] O. Sporns. “The human connectome: a complex network”. In: *Annals of the New York Academy of Sciences* 1224.1 (2011), pp. 109–125. DOI: 10.1111/j.1749-6632.2010.05888.x.
- [56] Alex Fornito, Andrew Zalesky, and Michael Breakspear. “The connectomics of brain disorders”. In: *Nature reviews. Neuroscience* 16 (Feb. 2015), pp. 159–72. DOI: 10.1038/nrn3901.
- [57] Suzana Herculano-Houzel. “The Human Brain in Numbers: A Linearly Scaled-up Primate Brain”. In: *Front Hum Neurosci* 3.31 (2009). DOI: 10.3389/neuro.09.031.2009.
- [58] P. Hagmann et al. “Mapping the structural core of human cerebral cortex”. In: *PLoS Biology* 6.7 (2008). DOI: 10.1371/journal.pbio.0060159.
- [59] M. Rubinov and O. Sporns. “Complex network measures of brain connectivity: uses and interpretations”. In: *Neuroimage* 52.3 (2010), pp. 1059–1069. DOI: 10.1016/j.neuroimage.2009.10.003.
- [60] H. Taniguchi et al. “A resource of cre driver lines for genetic targeting of gabaergic neurons in cerebral cortex”. In: *Neuron* 71.6 (2011), 995–1013. DOI: 10.1016/j.neuron.2011.07.026.
- [61] Seung Oh et al. “A mesoscale connectome of the mouse brain”. In: *Nature* 508 (Apr. 2014). DOI: 10.1038/nature13186.

- [62] Gabriella Ugolini. “Advances in viral transneuronal tracing”. In: *Journal of Neuroscience Methods* 194 (Jan. 2009), pp. 2–20. DOI: 10.1016/j.jneumeth.2009.12.001.
- [63] P. Hagmann et al. “Mapping human whole-brain structural networks with diffusion MRI”. In: *PLoS One* 2.7 (2007). DOI: 10.1371/journal.pone.0000597.
- [64] P. Osten and T. W. Margrie. “Mapping brain circuitry with a light microscope”. In: *Nature Methods* 10.6 (2013), pp. 515–523. DOI: 10.1038/nmeth.2477.
- [65] H. Okano and P. P. Mitra. “Brain-mapping projects using the common marmoset”. In: *Neuroscience research* 93 (2015), pp. 3–7. DOI: 10.1016/j.neures.2014.08.014.
- [66] E. A. Papp et al. “Brain-wide mapping of axonal connections: workflow for automated detection and spatial analysis of labeling in microscopic sections”. In: *Frontiers in neuroinformatics* 10 (2016). DOI: 10.3389/fninf.2016.00011.
- [67] G. Malandain et al. “Fusion of autoradiographs with an MR volume using 2-D and 3-D linear transformations.” In: *Neuroimage* 23 (2004). DOI: 10.1016/j.neuroimage.2004.04.038.
- [68] S Ourselin et al. “Reconstructing a 3D structure from serial histological sections. Image Vision Comput.” In: *Image Vision Comput* 19.1 (2001). DOI: 10.1016/S0262-8856(00)00052-4.
- [69] J Streicher, WJ Weninger, and GB Muller. “External marker-based automatic congruencing: a new method of 3D reconstruction from serial sections.” In: *Anat Rec*

- 248.4 (1997), pp. 583–602. DOI: 10.1002/(SICI)1097-0185(199708)248:4<583::AID-AR10>3.0.CO;2-L.
- [70] J Dauguet et al. “Three-dimensional reconstruction of stained histological slices and 3D non-linear registration with in vivo MRI for whole baboon brain.” In: *J Neurosci Methods* 164.1 (2007), pp. 191–204. DOI: 10.1016/j.jneumeth.2007.04.017.
- [71] D. H. Adler et al. “Histology-derived volumetric annotation of the human hippocampal subfields in postmortem MRI.” In: *Neuroimage* 84 (2014), pp. 505–23. DOI: 10.1016/j.neuroimage.2013.08.067.
- [72] Dam A Mouritzen. “Shrinkage of the brain during histological procedures with fixation in formaldehyde solutions of different concentrations”. In: *J Hirnforsch* 20 (2 1979), pp. 115–9.
- [73] Leibnitz L. “Studies on the optimization of weight and volume changes in brains during fixation, dehydration and brightening as well as on fresh brain volume estimates based on the weight of treated brains”. In: *J Hirnforsch* 13 (4 1971), pp. 320–9.
- [74] Ralf Quester and Roland Schroder. “The shrinkage of the human brain stem during formalin fixation and and embedding in paraffin”. In: *J Neurosci Methods* 75 (1 1997), pp. 81–89.

- [75] Hans F Wehrl et al. “Assessment of murine brain tissue shrinkage caused by different histological fixatives using magnetic resonance and computed tomography imaging”. In: *Histol Histopathol* 30 (5 2015), pp. 601–15. DOI: 10.14670/HH-30.601.
- [76] Georg Schulz et al. “Three-dimensional strain fields in human brain resulting from formalin fixation”. In: *J Neurosci Methods* 202 (1 2011), pp. 16–27. DOI: 10.1016/j.jneumeth.2011.08.031.
- [77] C. N. Carlo and C. F. Stevens. “Analysis of differential shrinkage in frozen brain sections and its implications for the use of guard zones in stereology”. In: *J Comp Neurol* 519 (14 2011), pp. 12803–10. DOI: 10.1002/cne.22652.
- [78] H. N. Sabbah et al. “Left ventricular shape changes during the course of evolving heart failure”. In: *Am J Physiol* 263 (1992), pp. 226–270. DOI: 10.1152/ajpheart.1992.263.1.H266.
- [79] Matthew Wheeler et al. “A New Era in Clinical Genetic Testing for Hypertrophic Cardiomyopathy”. In: *Journal of cardiovascular translational research* 2 (Dec. 2009), pp. 381–91. DOI: 10.1007/s12265-009-9139-0.
- [80] F. Saremi, J.D. Grizzard, and R.J. Kim. “Optimizing Cardiac MR Imaging: Practical Remedies for Artifacts”. In: *Radiographics* 28.4 (2008), pp. 1161–1187.
- [81] M. Alexa, D. Cohen-Or, and D. Levin. “As-rigid-as-possible shape interpolation”. In: *Proc. ACM SIGGRAPH* (2000), pp. 157–164.

- [82] Stanley Durrleman et al. “Toward a Comprehensive Framework for the Spatiotemporal Statistical Analysis of Longitudinal Shape Data”. In: *Int J Comp Vis* 103.1 (2013), pp. 22–59.
- [83] P Thomas Fletcher. “Geodesic regression and the theory of least squares on Riemannian manifolds”. In: *Int J Comput Vis* 105.2 (2013), pp. 171–185.
- [84] D. J. Tward et al. “Tools for registering 11T ex-vivo MRI of the human medial temporal lobe to a standard atlas coordinate system”. In: *Poster session presented at the Society for Neuroscience* (2018).
- [85] J-B. Schiratti et al. “Learning spatiotemporal trajectories from manifold-valued longitudinal data”. In: *Advances in Neural Information Processing Systems* (2015), pp. 2404–2412.
- [86] Y. Gao et al. “Image registration and segmentation in longitudinal MRI using temporal appearance modeling”. In: *Proc. IEEE ISBI* (2016), pp. 629–632.
- [87] M.M. Chakravarty et al. “The creation of a brain atlas for image guided neurosurgery using serial histological data”. In: *Neuroimage* 30.2 (2006), pp. 359–376.
- [88] J. Ehrhardt et al. “An optical flow based method for improved reconstruction of 4D CT data sets acquired during free breathing”. In: *Med Phys* 34.2 (2007), pp. 711–21.

- [89] Oleg Lobachev, Birte S Steiniger, and Michael Guthe. “Compensating Anisotropy in Histological Serial Sections with Optical Flow-Based Interpolation”. In: May 2017. DOI: 10.1145/3154353.3154366.
- [90] Alejandro Frangi et al. “Automatic Construction of Multiple-object Three-dimensional Statistical Shape Models: Application to Cardiac Modelling.” In: *Medical Imaging, IEEE Transactions on* 21 (Oct. 2002), pp. 1151–1166. DOI: 10.1109/TMI.2002.804426.
- [91] Vicky Y. Wang et al. “Modelling passive diastolic mechanics with quantitative MRI of cardiac structure and function”. In: *Medical Image Analysis* 13.5 (2009). Includes Special Section on the 12th International Conference on Medical Imaging and Computer Assisted Intervention, pp. 773–784. ISSN: 1361-8415. DOI: <https://doi.org/10.1016/j.media.2009.07.006>. URL: <http://www.sciencedirect.com/science/article/pii/S1361841509000619>.
- [92] Siamak Ardekani et al. “Shape Analysis of Hypertrophic and Hypertensive Heart Disease using MRI-based 3D Surface Models of Left Ventricular Geometry”. In: *Medical Image Analysis* 29 (Dec. 2015). DOI: 10.1016/j.media.2015.11.004.
- [93] O. Oktay et al. “Anatomically Constrained Neural Networks (ACNNs): Application to Cardiac Image Enhancement and Segmentation”. In: *IEEE Transactions on Medical Imaging* 37.2 (2018), pp. 384–395.

- [94] Alzheimer's Association. "2019 Alzheimer's disease facts and figures". In: *Alzheimer's & Dementia* 15.3 (2019), pp. 321–387. DOI: 10.1016/j.jalz.2019.01.010. eprint: <https://alz-journals.onlinelibrary.wiley.com/doi/pdf/10.1016/j.jalz.2019.01.010>. URL: <https://alz-journals.onlinelibrary.wiley.com/doi/abs/10.1016/j.jalz.2019.01.010>.
- [95] J.G. Csernansky et al. "Preclinical detection of Alzheimer's disease: Hippocampal shape and volume predict dementia onset in the elderly". In: *NeuroImage* 25 (May 2005), pp. 783–92.
- [96] John G. Csernansky et al. "Hippocampal morphometry in dementia of the Alzheimer type by computer algorithm". In: *Soc Neurosci Abst* 24 (1998), p. 264.
- [97] L. Wang et al. "Changes in hippocampal volume and shape across time distinguish dementia of the Alzheimer type from healthy aging". In: *Neuroimage* 20 (2003), pp. 667–82.
- [98] Lei Wang et al. "Hippocampal Shape Abnormalities in Early AD: A Replication Study". In: *Alzheimer's Association International Conference on Prevention of Dementia: Early Diagnosis and Intervention*. Washington, D.C., 2005.
- [99] Lei Wang et al. "Abnormalities of hippocampal surface structure in very mild dementia of the Alzheimer type". In: *NeuroImage* 30 (Apr. 2006), pp. 52–60. DOI: 10.1016/j.neuroimage.2005.09.017.

- [100] Anqi Qiu et al. “Region of Interest Based Analysis of Cortical Thickness Variation of Left Planum Temporale in Schizophrenia and Psychotic Bipolar Disorder”. In: *Human Brain Mapping* 29 (2008), pp. 973–985.
- [101] John Csernansky et al. “Abnormalities of Thalamic Volume and Shape in Schizophrenia”. In: *The American journal of psychiatry* 161 (June 2004), pp. 896–902. DOI: 10.1176/appi.ajp.161.5.896.
- [102] Anqi Qiu et al. “Regional Subcortical Shape Abnormalities in Mild Cognitive Impairment and Alzheimer’s Disease”. In: *NeuroImage* 45 (2009), pp. 656–661.
- [103] Marco Lorenzi et al. “Mapping the Effects of AB1-42 Levels on the Longitudinal Changes in Healthy Aging: Hierarchical Modeling Based on Stationary Velocity Fields”. In: *Medical Image Computing and Computer-Assisted Intervention – MICCAI 2011*. Vol. 6892. Berlin, Heidelberg: Springer, 2011.
- [104] Alexandre Bône et al. “Deformetrica 4: an open-source software for statisticalshape analysis”. In: *ShapeMI @ MICCAI 2018, Lecture Notes in Computer Science*. Vol. 11167. 2018.
- [105] Alexandre Bône, Olivier Colliot, and Stanley Durrleman. *Learning the spatiotemporal variability in longitudinal shape data sets*. HAL Preprint: fhal-02091549v4f. 2019.

- [106] Anqi Qiu et al. “Parallel transport in diffeomorphisms distinguishes the time-dependent pattern of hippocampal surface deformation due to healthy aging and the dementia of the Alzheimer’s type”. In: *Neuroimage* 40.1 (2008), pp. 68–76.
- [107] Daniel J Tward et al. “Entorhinal and transentorhinal atrophy in mild cognitive impairment using longitudinal diffeomorphometry”. In: *Alzheimers Dement* 9 (2017), pp. 41–50.
- [108] Xiaoying Tang et al. “The diffeomorphometry of regional shape change rates and its relevance to cognitive deterioration in mild cognitive impairment and Alzheimer’s disease: Diffeomorphometry of Regional Shape Change Rates.” In: *Human Brain Mapping* 36.6 (2015), pp. 2093–2117.
- [109] Michael Miller et al. “The diffeomorphometry of temporal lobe structures in preclinical Alzheimer’s disease”. In: *NeuroImage: Clinical* 3 (Dec. 2013), pp. 352–360. DOI: 10.1016/j.nicl.2013.09.001.
- [110] L Younes et al. “Regionally selective atrophy of subcortical structures in prodromal HD as revealed by statistical shape analysis”. In: *Human Brain Mapping* (2012).
- [111] Anqi Qiu and Michael I. Miller. “Multi-structure network shape analysis via normal surface momentum maps”. In: *NeuroImage* 42.4 (2008), pp. 1430–1438. ISSN: 1053-8119. DOI: <http://doi.org/10.1016/j.neuroimage.2008.04.257>. URL: <http://www.sciencedirect.com/science/article/pii/S1053811908005946>.

- [112] A Qiu et al. “Basal Ganglia Volume and Shape in Children with Attention Deficit Hyperactivity Disorder”. In: *American Journal Psychiatry* 166.1 (2009), pp. 74–82.
- [113] Marco Lorenzi et al. “Disentangling Normal Aging from Alzheimer’s Disease in Structural MR Images.” In: *Neurobiology of aging* 36 (2015).
- [114] D. Tward et al. “Parametric Surface Diffeomorphometry for Low Dimensional Embeddings of Dense Segmentations and Imagery”. In: *IEEE Transactions on Pattern Analysis and Machine Intelligence* PP.99 (2016), pp. 1–1. ISSN: 0162-8828. DOI: 10.1109/TPAMI.2016.2578317.
- [115] Raphaël Sivera et al. “A model of brain morphological changes related to aging and Alzheimer’s disease from cross-sectional assessments”. In: *NeuroImage* 198 (May 2019).
- [116] Brian C. Lee et al. “On variational solutions for whole brain serial-section histology using the computational anatomy random orbit model”. In: *PLOS Computational Biology* 14 (Feb. 2018). DOI: 10.1371/journal.pcbi.1006610.
- [117] Brian C. Lee et al. “Diffeomorphic Upsampling of Serially Acquired Sparse 2D Cross-Sections in Cardiac MRI”. In: vol. 2019. July 2019, pp. 4491–4495. DOI: 10.1109/EMBC.2019.8856317.
- [118] Brian C. Lee et al. “Multimodal Cross-registration and Quantification of Metric Distortions in Marmoset Whole Brain Histology using Diffeomorphic Mappings [pub-

- lished online ahead of print, 2020 May 14]”. In: *J Comp Neurol* (May 2020). DOI: 10.1002/cne.24946.
- [119] J.K. Mai and G. Paxinos. *The Human Nervous System*. Academic Press, 2011. ISBN: 9780080921303.
- [120] S. Mori et al. *MRI Atlas of Human White Matter*. Elsevier, 2005. ISBN: ISBN-13: 978-0123820815.
- [121] Nelson Chuang et al. “An MRI-based atlas and database of the developing mouse brain”. In: *Neuroimage* 54.1 (2011), pp. 80–89. DOI: 10.1016/j.neuroimage.2010.07.043.
- [122] S. Mori et al. “Atlas-Based Neuroinformatics via MRI: Harnessing Information from Past Clinical Cases and Quantitative Image Analysis for Patient Care”. In: *Annual Review of Biomedical Engineering* 15 (2013), pp. 71–92. DOI: 10.1146/annurev-bioeng-071812-152335.
- [123] Jun Ma et al. “Bayesian template estimation in computational anatomy.” In: *NeuroImage* 42.1 (2008), pp. 252–261. URL: <http://www.pubmedcentral.nih.gov/articlerender.fcgi?artid=2602958&tool=pmcentrez&rendertype=abstract>.
- [124] E. S. Lein et al. “Genome-wide atlas of gene expression in the adult mouse brain”. In: *Nature* 445 (2007), pp. 168–176. DOI: 10.1038/nature05453.

- [125] Michael I Miller, Alain Trouvé, and Laurent Younes. “Geodesic Shooting for Computational Anatomy.” In: *Journal of Mathematical Imaging and Vision* 24.2 (2006), pp. 209–228. ISSN: 15737683. DOI: 10.1007/s10851-005-3624-0. URL: <http://www.pubmedcentral.nih.gov/articlerender.fcgi?artid=2897162&tool=pmcentrez&rendertype=abstract>.
- [126] Michael I Miller, Alain Trouvé, and Laurent Younes. “Hamiltonian Systems and Optimal Control in Computational Anatomy: 100 Years Since D’Arcy Thompson.” In: *Annual Review of Biomed Engineering* 17 (2015), pp. 447–509. DOI: 10.1146/annurev-bioeng-071114-040601.
- [127] A.D. Lanterman, U. Grenander, and M.I. Miller. “Bayesian Segmentation via Asymptotic Partition Functions”. In: *IEEE Trans. on Pattern Analysis and Machine Intelligence* 22.4 (2000), pp. 337–347. DOI: 10.1109/34.845376.
- [128] Kwame S. Kutten et al. “A Diffeomorphic Approach to Multimodal Registration with Mutual Information: Applications to CLARITY Mouse Brain Images”. In: (Dec. 2016).
- [129] Alexander Woodward et al. “The Brain/MINDS 3D digital marmoset brain atlas”. In: *Nature Sci Data* 20.180009 (5 2018). DOI: 10.1038/sdata.2018.9.

- [130] Vadim Pinksly et al. “High-Throughput Method of Whole-Brain Sectioning, Using the Tape-Transfer Technique”. In: *PLoS One* 10.7 (2015). DOI: 10.1371/journal.pone.0102363.
- [131] Meng Kuan Lin et al. “A High-throughput Neurohistological Pipeline for Brain-Wide Mesoscale Connectivity Mapping of the Common Marmoset”. In: *eLife* (2019).
- [132] B. Lee et al. “On variational solutions for whole brain serial-section histology using the computational anatomy random orbit model”. In: *PLOS Computational Biology* (2018).
- [133] G. Malandain et al. “Fusion of autoradiographs with an MR volume using 2-D and 3-D linear transformations.” In: *Neuroimage* 23 (2004). DOI: 10.1016/j.neuroimage.2004.04.038.
- [134] T. Sorensen. “A method of establishing groups of equal amplitude in plant sociology based on similarity of species and its application to analyses of the vegetation on Danish commons”. In: *Kongelige Danske Videnskabernes Selskab* 5 (1948), pp. 1–34.
- [135] Lee R. Dice. “Measures of the Amount of Ecologic Association Between Species”. In: *Ecology* 26.3 (1945), pp. 297–302.
- [136] Yan Cao et al. “Large deformation diffeomorphic metric mapping of vector fields”. In: *IEEE Transactions on Medical Imaging* 24.9 (2005), pp. 1216–1230. ISSN: 0278-0062. DOI: 10.1109/TMI.2005.853923.

- [137] J Ashburner. “A fast diffeomorphic image registration algorithms”. In: *Neuroimage* 38.1 (2007), pp. 95–113.
- [138] Brian C. Lee et al. “Infinitesimal Drift Diffeomorphometry Models for Population Shape Analysis”. In: *IEEE/CVF Conference on Computer Vision and Pattern Recognition. 5th International Workshop on Differential Geometry in Computer Vision and Machine Learning*. 2020.
- [139] Samuel Karlin and Howard Taylor. In: *Second Edition: A First Course in Stochastic Processes*. Academic Press, 2012, pp. 1–557.
- [140] Darryl D. Holm. “Variational principles for stochastic fluid dynamics”. In: *Proceedings of the Royal Society A: Mathematical, Physical and Engineering Sciences* 471.2176 (2015), p. 20140963. ISSN: 1471-2946. DOI: 10.1098/rspa.2014.0963. URL: <http://dx.doi.org/10.1098/rspa.2014.0963>.
- [141] E.T. Jaynes. “On the rationale of maximum-entropy methods”. In: *Proc. of the IEEE* 70 (September 1982), pp. 939–952.
- [142] R.W. Johnson, J.E. Shore, and J.P. Burg. “Multisignal minimum-cross-entropy spectrum analysis with weighted initial estimates”. In: *IEEE Transactions on Acoustics, Speech and Signal Processing* ASSP-32, No.3 (June 1984), pp. 531–539.

- [143] Jan M. Van Campenhout and T. M. Cover. “Maximum entropy and conditional probability”. In: *IEEE Transactions on Information Theory* IT-27, No. 4 (July 1981), pp. 483–489.
- [144] Lalit Bahl, Frederick Jelinek, and Robert Mercer. “A Maximum Likelihood Approach to Continuous Speech Recognition”. In: *Pattern Analysis and Machine Intelligence, IEEE Transactions on PAMI-5* (Apr. 1983), pp. 179–190. DOI: 10.1109/TPAMI.1983.4767370.
- [145] Stuart Geman and Donald Geman. “Stochastic Relaxation, Gibbs Distributions, and the Bayesian Restoration of Images”. In: *IEEE Trans. Pattern Anal. Machine Int.* 6 (1984), pp. 721–741.
- [146] M.I. Miller and D.L. Snyder. “The Role of Likelihood and Entropy in Incomplete-Data Problems: Applications to Estimating Point-Process Intensities and Toeplitz Constrained Covariances”. In: *Proceedings of the IEEE* 75, No.7 (July 1987), pp. 892–907.
- [147] Ronald R. Coifman and Mladen .V. Wickerhauser. “Entropy based algorithms for best basis selections”. In: *IEEE Trans. on Information Theory* 38 (1992), pp. 713–718.

- [148] Song Zhu, Yingnian Wu, and David Mumford. “Minimax Entropy Principle and Its Application to Texture Modeling”. In: *Neural Computation* 9 (Sept. 2000). DOI: 10.1162/neco.1997.9.8.1627.
- [149] B. Gidas. “Global Optimization Via the Langevin Equation”. In: *Proceedings of the 24th Conference on Decision and Control*. Ft. Lauderdale, Fl., 1985, pp. 774–778.
- [150] Stuart Geman and Chii Ruey Hwang. “Diffusions for Global Optimization”. In: *SIAM J. Control and Optimization* 24 (1987), pp. 1031–1043.
- [151] Ulf Grenander and Michael I. Miller. “Representations of Knowledge in Complex Systems”. In: *J. Roy. Stat. Soc. B* 56.3 (1994), pp. 549–603.
- [152] Michael Miller et al. “Computational anatomy and diffeomorphometry: A dynamical systems model of neuroanatomy in the soft condensed matter continuum.” In: *Wiley Interdiscip Rev Syst Biol Med* 10.6 (2018).
- [153] Michael I. Miller, Alain Trouvé, and Laurent Younes. “Geodesic Shooting for Computational Anatomy”. In: *J. Mathematical Imaging and Vision* 24 (2006), pp. 209–228.
- [154] Ronald Petersen et al. “Alzheimer’s Disease Neuroimaging Initiative (ADNI): Clinical characterization”. In: *Neurology* 74 (Jan. 2010), pp. 201–9. DOI: 10.1212/WNL.0b013e3181cb3e25.

- [155] Marilyn Albert et al. “Cognitive Changes Preceding Clinical Symptom Onset of Mild Cognitive Impairment and Relationship to ApoE Genotype”. In: *Current Alzheimer Research* 11 (Sept. 2014), pp. 773–84. DOI: 10.2174/156720501108140910121920.
- [156] I.J. Arnold. “Sur la géométrie différentielle des groupes de Lie de dimension infinie et ses applications à l’hydrodynamique des fluides parfaits”. In: *Ann. Inst. Fourier (in French)* 16.1 (1966), pp. 319–361. DOI: doi:10.5802/aif.233.
- [157] Laurent Younes et al. “Transport of Relational Structures in Groups of Diffeomorphisms”. In: *Journal of Mathematical Imaging and Vision* (2008).
- [158] Daniel J. Tward. “Singular geodesic coordinates for representing diffeomorphic maps in computational anatomy, with application to the morphometry of early Alzheimer’s disease in the medial temporal lobe”. PhD thesis. Johns Hopkins University, 2017.

Curriculum Vitae

Brian Lee was born in New Jersey in 1990. He graduated as an undergraduate from the University of Pennsylvania in 2012 with a Bachelor of Science in Engineering as part of the Bioengineering Department, where he worked with Professor Lou Soslowsky on orthopedic ultrasound imaging. He went on to receive his Masters degree in Bioengineering at the University of Pennsylvania in 2013, where he worked with Professor Andrew Maidment on tomosynthesis image quality. He joined the Biomedical Engineering PhD program at Johns Hopkins University in the fall of 2013 where he joined Professor Michael Miller's lab at the Center for Imaging Science. As a PhD student, his research interests were in developing novel diffeomorphic image registration algorithms in order to facilitate understanding of the brain and its pathologies.